



A University of Sussex DPhil thesis

Available online via Sussex Research Online:

<http://sro.sussex.ac.uk/>

This thesis is protected by copyright which belongs to the author.

This thesis cannot be reproduced or quoted extensively from without first obtaining permission in writing from the Author

The content must not be changed in any way or sold commercially in any format or medium without the formal permission of the Author

When referring to this work, full bibliographic details including the author, title, awarding institution and date of the thesis must be given

Please visit Sussex Research Online for more information and further details



Exploring Star Formation in Galaxy Populations using the Far-Infrared - Radio Correlation

Richard F. White

Submitted for the degree of Doctor of Philosophy

University of Sussex

May 2014

Declaration

I hereby declare that this thesis has not been and will not be submitted in whole or in part to another University for the award of any other degree.

Signature:

Richard White

UNIVERSITY OF SUSSEX

RICHARD F. WHITE, DOCTOR OF PHILOSOPHY

EXPLORING STAR FORMATION IN GALAXY POPULATIONS
USING THE FAR-INFRARED - RADIO CORRELATIONSUMMARY

In this thesis I take a close look at the far-infrared radio - correlation, a puzzlingly persistent and tight relationship identified between the far-infrared and radio luminosities of star forming galaxies. Two disparate processes are attributed to this phenomenon. In the first, starlight from massive stars is reprocessed by dust to be re-emitted in the infrared and secondly, radio emission in the form of synchrotron radiation originating in shocks driven by these same high mass stars as they end their lives as supernovae. Cosmic ray electrons are accelerated by these shocks, their paths subsequently spiralling in their host galaxies magnetic fields, produce a continuum of synchrotron radiation. I investigate this far-infrared radio correlation for a large sample of IRAS galaxies and compare my results to previous studies. I look at the effect of peak galaxy dust temperature on the correlation, dividing my sample into ‘warm’ and ‘cool’ bins and find a lower flux ratio in the warm sample. The correlation at low radio frequencies is tested, probing the constancy of the dominant synchrotron radiation where absorption or other effects are expected to lead to a divergence from the linear continuum spectrum. Finally I look at a smaller sample of galaxies in the ELAIS-N1 field using HerMES and GMRT data to investigate the correlation to higher redshifts. The interest and rationale for investigating this correlation is its evident link to star formation. Any deviation for example will imply an evolution in one or both of these processes which are closely linked to star formation. With the advent of new dedicated low frequency array radio telescopes such as LOFAR it is increasingly necessary to trust the correlation at these longer wavelengths if observational data is to be used as a reliable predictive tool in the study of star formation.

Acknowledgements

As a part time student I have seen many other students complete their PhDs at the University of Sussex Astronomy Centre. Too numerous to mention their names here, but all have been very supportive and willing to help with any problems making this extended period of research a pleasure. I would like to thank my supervisor Seb Oliver for his unfailing directions and explanations that have helped to formulate this PhD thesis. I would also like to thank the University of Sussex School of Mathematical and Physical Sciences for funding this research via the fee waiver scheme whilst I have continued to work in the Physics Department in the role of Chief Technician and Electronics Engineer.

Official acknowledgements:

- This research has made extensive use of the *Imperial IRAS-FSC Redshift Catalogue* (IIFSCz) [Wang & Rowan-Robinson \(2009\)](#).
- This research has made use of the NASA/IPAC Extragalactic Database (NED) which is operated by the Jet Propulsion Laboratory, California Institute of Technology, under contract with the National Aeronautics and Space Administration.
- This research is based in part on observations with the Infrared Astronomical Satellite (*IRAS*), a joint project of the US, UK and the Netherlands, [Neugebauer et al. \(1984\)](#).
- This research is based in part on observations with the GMRT, [Swarup, Ananthkrishnan, Kapahi, Rao, Subrahmanya & Kulkarni \(1991\)](#)
- This research is based in part on observations with the NRAO VLA. The National Radio Astronomy Observatory is a facility of the National Science Foundation operated under cooperative agreement by Associated Universities, Inc.
- This research has made use of the VizieR catalogue access tool, CDS, Strasbourg, France”. The original description of the VizieR service was published in A&AS by

Ochsenbein, Bauer & Marcout (2000).

- This research has made use of data from HerMES project (<http://hermes.sussex.ac.uk/>). HerMES is a Herschel Key Programme utilising Guaranteed Time from the SPIRE instrument team, ESAC scientists and a mission scientist. The HerMES data was accessed through the Herschel Database in Marseille (HeDaM - <http://hedam.lam.fr>) operated by CeSAM and hosted by the Laboratoire d'Astrophysique de Marseille.
- This research has made use of VLSSr data, [Lane et al. \(2012\)](#) "VLSS Redux: Software Improvements applied to the Very Large Array Low-frequency Sky Survey".
- This research has made use of NASA's Astrophysics Data System

Contents

List of Tables	ix
List of Figures	xii
1 Introduction	1
1.1 Astronomical context	2
1.2 Infrared emission	2
1.3 Radio Emission	4
1.3.1 Non-Thermal radio	4
1.3.2 Thermal radio	4
1.4 Observation at radio and infrared wavelengths	5
1.4.1 Infrared surveys	6
1.4.2 Radio surveys	7
1.5 The discovery of the far-infrared radio correlation	9
1.6 Theories of how the correlation works	11
1.7 Evolution in the FIRC	14
1.8 Application of the FIRC	16
1.9 Outline of the thesis	17
2 The Far-Infrared - Radio Correlation at 1.4GHz	19
2.1 Introduction	19
2.2 Data selection	21
2.2.1 The IIFSCz catalogue	21
2.2.2 The radio data	22
2.2.3 Data Sample Boundary	22
2.3 Quantification of the Far-Infrared-Radio Correlation	23
2.3.1 K-corrections	26
2.3.2 Removal of AGN	28

2.3.3	Volume Limited Samples	29
2.3.4	Survival analysis	30
2.4	Results	30
2.4.1	q_{FIR}	33
2.4.2	q_{L60}	39
2.4.3	q_{TIR}	44
2.5	Discussion	50
3	The FIRC as a function of temperature	51
3.1	The q of warm and cold galaxies	51
3.1.1	Dust Temperatures	52
3.2	Results	57
3.3	Discussion	65
4	The Far-Infrared Radio Correlation at low radio frequencies	67
4.1	Introduction	67
4.2	The FIRC at 74 MHz	69
4.2.1	Low frequency turnover	70
4.2.2	Data	71
4.2.3	Spectral Index	72
4.3	Results	74
4.4	Discussion	78
5	FIRC with HerMES and GMRT	79
5.1	Introduction	79
5.2	Hermes fields	79
5.3	GMRT-the telescope	81
5.4	Radio data	81
5.5	Far-infrared data	84
5.6	Method and results	85
5.7	Discussion	91
6	Conclusions	92
6.1	Future work	96
	Bibliography	97

List of Tables

1.1	<i>Herschel</i> instrumentation specifications	8
1.2	Theoretical models explaining the FIR-radio correlation	15
2.1	Fir-radio correlation of specific fields	20
2.2	q_{FIR} redshift slices	36
2.3	q_{FIR} luminosity slices	37
2.4	q_{FIR} divided into redshift / luminosity bins	38
2.5	q_{L60} redshift slices	41
2.6	q_{L60} luminosity slices, restframe	43
2.7	q_{LTIR} redshift slices	47
2.8	q_{LTIR} luminosity slices	48
2.9	Variation in q_{L60} with galaxy types	49
3.1	q_{LTIR} of cold and warm samples in luminosity and redshift blocks and slices	64
4.1	Radio surveys at Low frequency	70
4.2	Sources with a low spectral index at 74 MHz	73
5.1	Radio frequency coverage of the ELAIS-N1 field	83
5.2	q_{LTIR} redshift slices. 325 MHz sample	88
5.3	q_{LTIR} redshift slices. 610 MHz sample	90
6.1	q_{TIR} 1.4 GHz to 74 MHz	95

List of Figures

1.1	The Cosmic Optical and Infrared Background	3
1.2	The Hubble Tuning Fork	3
1.3	Super Novae Remnant W44 imaged by <i>Herschel</i> and <i>XMM</i>	5
1.4	<i>HerMES</i> fields.	8
1.5	The FIR/radio correlation at $60\mu m$ and 1.49 GHz	10
2.1	Sample area defined by the <i>VLA</i> First survey	21
2.2	The radio spectrum of M82	25
2.3	Restframe M82 Infrared SED	25
2.4	M82 vs Arp220 k -correction	28
2.5	Typical probability distribution plot	31
2.6	q_{FIR} calculated using Helou formula	32
2.7	Far-infrared/radio correlation of a sample $> 11,00$ galaxies	33
2.8	q_{FIR} plotted against redshift	35
2.9	Mean q_{FIR} versus redshift	36
2.10	Mean q_{FIR} versus $\log L_{60}$	37
2.11	q_{L60} plotted against redshift	39
2.12	Histogram of the q_{L60} total sample	41
2.13	q_{L60} plotted against L_{60}	42
2.14	Mean q_{L60} versus redshift	42
2.15	Mean q_{L60} versus $\log L_{60}$	43
2.16	L_{TIR} vs redshift with $60 \mu m$ cut + number of objects per redshift slice	44
2.17	L_{TIR} vs redshift with $60 \mu m$ cut + number of objects per luminosity slice	45
2.18	Mean q_{TIR} versus redshift	47
2.19	Mean q_{TIR} versus $\log L_{60}$	48

3.1	The radio luminosity at 1.4 GHz vs. the total FIR luminosity of the warm and cold components	52
3.2	Herschel’s far-infrared view of the Andromeda galaxy, M31 imaged at 250 μm	53
3.3	The radio luminosity at 1.4 GHz vs. the total FIR luminosity for a sample of 369 warm objects selected with a temperature above 24 K	57
3.4	The radio luminosity at 1.4 GHz vs. the total FIR luminosity for a sample of 356 cool objects selected with a temperature below 24 K	58
3.5	The radio luminosity at 1,4 GHz vs. the total FIR luminosity for a sample of 725 objects. Warm objects above 24 K, cool objects below 24 K	59
3.6	q_{TIR} vs Redshift	60
3.7	q_{TIR} of cool and warm objects	60
3.8	Linear fit to the warm and cold sample	61
3.9	Histogram of cold (< 24 K) sample	61
3.10	Histogram of warm (> 24 K) sample	62
3.11	Luminosity vs. temperature of the warm and cool samples	62
4.1	Wavelength coverage and baselines of past, present and future Low frequency arrays compared	68
4.2	FIRCOR at 151 MHz. Plot of FIR flux against radio flux density at 151 MHz	69
4.3	Dispersion in Spectral index 1 GHz to 74 MHz	74
4.4	$q_{74\text{MHz}}$ and $q_{1.4\text{GHz}}$ compared	75
4.5	$q_{74\text{MHz}}$ and $q_{1.4\text{GHz}}$ using <i>AKARI</i> FIR fluxes	76
4.6	$q_{1.4\text{GHz}}$ vs. $q_{74\text{MHz}}$ calculated from IRAS 12, 25, 60 and 100 μm plus <i>AKARI</i> 140 μm flux densities	77
5.1	The ‘Great Observatory Origins Deep Survey (GOODS) Field North observed by the Herschel Spectral and Photometric Imaging Receiver (SPIRE)	80
5.2	The ‘Wedding cake survey’	80
5.3	GMRT at Pune	81
5.4	GMRT location 80 km north of Pune and 10 km east of Narayangaon, illustrating the configuration of the 30 antennae	82
5.5	Map of the ELAIS-N1field	83
5.6	q_{L70} of the 325 MHz selected sample compared to q_{L70} at 1.4 GHz	86
5.7	q_{L70} of the 610 MHz selected sample compared to q_{L70} at 1.4 GHz	87

5.8	q_{LTIR} of the 325 MHz selected sample	88
5.9	q_{LTIR} of the 610 MHz selected sample	89
5.10	q_{LTIR} subset of the 610 MHz selected sample	90
6.1	LOFAR sensitivities for a 6-station Superterp, a 24-station core array, a 40-station Dutch array, and a 48-station full array	94

Glossary of Terms and Acronyms

α	Spectral index of a power law radio spectrum
AGN	Active Galactic Nucleus
AKARI	Japanese infrared space observatory
β	Spectral index of dust emissivity
CR _e	Cosmic ray electrons
CSS	Compact Peaked Spectrum sources
ESA	European Space Agency
FIR	Far-infrared
FIRC	Far-infrared/Radio Correlation
FIRST	Faint Images of the Radio Sky at Twenty-Centimeters
FMR	False Matching Rate
FSC	<i>IRAS</i> Faint Source Catalogue
FWHM	Full Width Half Maximum
GMRT	Giant Metrewave Radio Telescope
GPS	Gigahertz Peaked Spectrum radio sources
HerMES	Herschel Multi-tiered Extragalactic Survey
HIFI	Heterodyne Instrument for the Far Infrared
HLIRGS	Hyper luminous infrared galaxies
IRAS	Infrared Astronomical Satellite
IIFSCz	Imperial IRAS-FSC Redshift Catalogue
ISO	Infrared Space Observatory
JCMT	James Clerk Maxwell Telescope
KAO	Kuiper Airborne Observatory
KM	Kaplan Meier survival analysis
L_{TIR}	Integrated total IR luminosity (8 - 1000 μ m) (L_{\odot})
LOFAR	LOW-Frequency ARray, radio interferometer

LWA	Long Wavelength array
NVSS	The NRAO VLA Sky Survey
PACS	Photodetector Array Camera and Spectrometer
PAH	Polycyclic Aromatic Hydrocarbon
q	Logarithmic IR/radio ratio
q_{FIR}	Logarithmic total flux (42.5 - 122.5 μm)/radio ratio
qL_{TIR}	Logarithmic total integrated luminosity(8 - 1000 μm)/radio ratio
QSO	Quasi-stellar object
SDSS	The Sloan Digital Sky Survey
SED	Spectral energy distribution
SB	Starburst galaxies
SFR	Star formation rate
SNe	Supernovae
SKA	Square Kilometre Array
SLOAN	The Sloan Digital Sky Survey
SPIRE	Spectral and Photometric Imaging REceiver
T_{dust}	Dust temperature (K)
TPT	Clark Lake Teepee-Tee radio telescope
ULIRG	Ultra Luminous Infrared Galaxy
UV	Ultraviolet
VLA	The Very Large Array
VLSS	The VLA Low-Frequency Sky Survey
WIM	Warm ionised medium
z	Redshift

Cosmology

In this thesis I adopt a cosmology with $\Omega_M = 0.3$, $\Omega_\Lambda = 0.7$, $H_0 = 70\text{kms}^{-1}\text{Mpc}^{-1}$

'Somewhere, something incredible is waiting to be known'

Carl Sagan

Chapter 1

Introduction

A recognised gap in our understanding of the processes of star formation is the persistent linearity of a correlation identified between the far-infrared and radio emissions of star-forming galaxies ([van de Kruit, 1971, 1973](#); [Helou et al., 1985](#); [de Jong et al., 1984](#)), this is the ‘Far-Infrared - Radio Correlation’ (FIRC). To date this correlation is poorly understood and a wider understanding of the phenomenon and its limits is needed to give astronomers greater confidence in its use as a tracer of star-formation rates. A number of questions are raised about the correlation: does the correlation evolve with redshift or luminosity, and does it hold to low radio frequencies? Magnetic field strengths, quenching of synchrotron emission by the CMB, evolution of the spectral energy distributions (SEDs) ([Seymour et al., 2009](#)), or cluster environments enhancing radio emission ([Miller & Owen, 2001](#)) are all potential disruptions to this remarkably linear correlation. In recent years there have been a number of explorations of the Far-Infrared - Radio Correlation but a consensus on its behaviour at higher redshifts is yet to emerge. ([Jarvis et al., 2010](#); [Sargent et al., 2010b](#); [Iverson et al., 2010](#); [Bourne et al., 2011](#)).

This thesis will examine the low redshift FIRC out to $z < 0.5$ with a large representative sample of galaxies which I test for evolution in redshift, luminosity and dust temperature. The correlation is poorly understood at low radio frequencies where a flattening of the radio spectrum has been observed compared with the power law flux densities observed at frequencies in the 1 GHz to 10 GHz range ([Hummel, 1991](#)). I evaluate the correlation in this domain with a low frequency radio continuum survey. The FIRC will also be tested in the ELAIS-N1 field to higher redshifts than explored in the main sample.

1.1 Astronomical context

It is less than one hundred years since [Hubble \(1925\)](#) confirmed the existence of galaxies independent of our own ‘Milky Way’ Galaxy. The notion that nebulous smudges observed through telescopes could be independent distant stellar systems in their own right was first predicted by [Kant \(1755\)](#). Optical observation of these distant galaxies alone cannot tell the whole story since it is now known that around half the light from these galaxies is emitted in the infrared wavelengths, see [Figure 1.1 \(Dole et al., 2006\)](#). Observations at these long wavelengths are seeing starlight reprocessed by dust. At even longer wavelengths it is possible to observe radio emissions from many types of galaxy.

One of the main drivers of present extragalactic astronomy is the understanding of galaxy formation. A hierarchical structure formation model for galaxies is now accepted but would benefit from a greater insight into the star formation histories of galaxies to tell the whole story. Hubble gave us the ‘tuning fork’ diagram illustrated in [Figure 1.2](#), which is purely a classification list with no respect to evolution so tells us nothing about the formation process. At present we are still unable to classify galaxies types in any true formation order, hence there is a great need to understand the history of galaxies. By observing galaxies at increasing redshifts we are able look back in time resolving snapshots of galaxy formation history but even this does not tell the whole story.

One way forward is by observing at infrared and radio wavelengths. We can now start to build a picture of the star formation histories, probing the interiors of galaxies where star formation would otherwise be hidden from view. With a firmer understanding of the FIRC it will be possible to define a radio luminosity/star-formation relationship that can differentiate between normal star-forming galaxies and radio loud Active Galactic Nuclei (AGN) ([Bell, 2003](#)).

1.2 Infrared emission

Infrared emission radiating from galaxies is the result of ultra-violet (UV) radiation from massive stars, reprocessed by interstellar dust grains. This dust or ‘soot’ consists of very small grains of silicates or graphite ranging in size from a few tenths to a few tens of nanometers in radius. It is believed that these small grains will emit a near thermal modified black body when subjected to intense UV radiation and that the emission profile will become broader and longer wavelength in more quiescent UV environs ([Desert et al., 1990](#)). A third component in this interstellar medium is the presence of Polycyclic Aro-

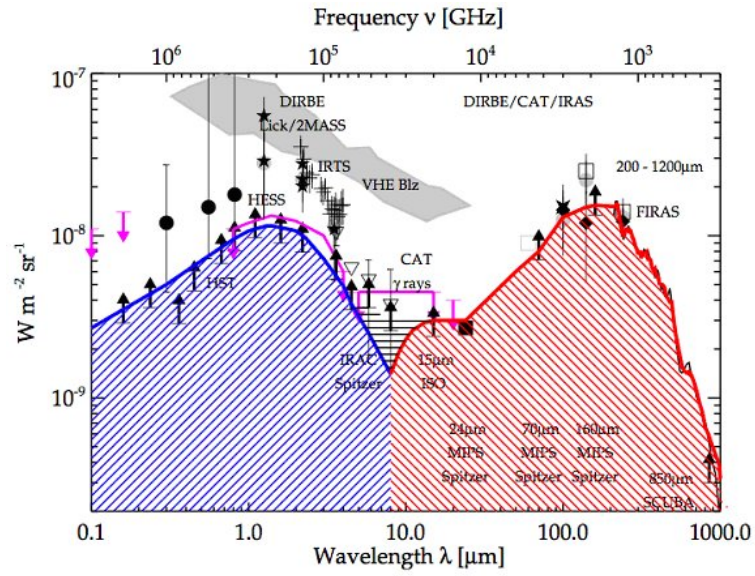


Figure 1.1: The Cosmic Optical Background (blue) and The Cosmic Infrared Background (red), illustrating the spectral energy distribution of the total light received between 0.1 and 1000 μm . From: [Dole et al. \(2006\)](#), Figure 13.

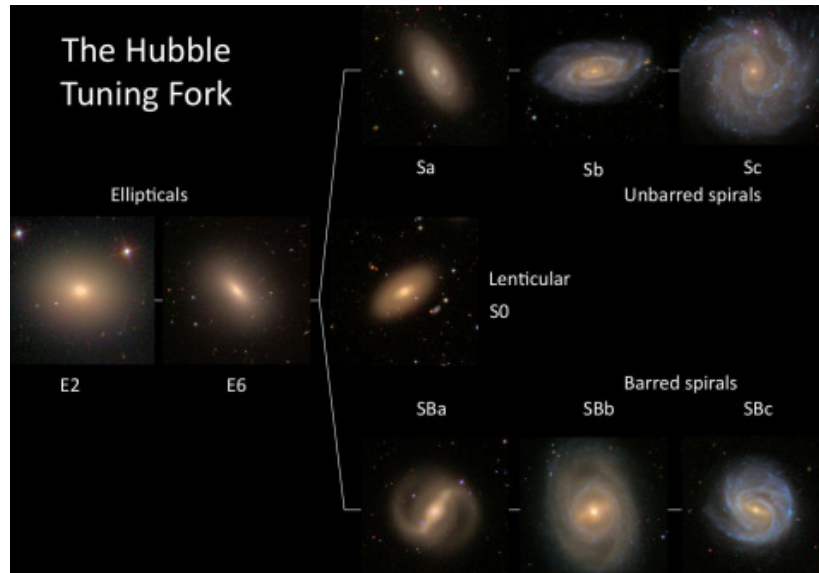


Figure 1.2: The Hubble Tuning Fork interpreted with images from the Sloan Digital Sky Survey. Credit: Karen Masters [ICG Portsmouth]

matic Hydrocarbons (PAHs) which emit in the near infrared accounting for $\approx 30\%$ of the energy emitted (Beelen, 2004).

1.3 Radio Emission

1.3.1 Non-Thermal radio

Cosmic rays, which are particles, electrons and protons, are thought to be accelerated to relativistic speeds in the shocks produced when massive ($> 8M_{\odot}$) stars explode as Type-II supernova at the end of their lives, producing broadband synchrotron radio emission as they spiral in their host galaxies' magnetic fields. Until now it has only been proposed that the cosmic rays are produced by supernova since the direct detection of cosmic ray sources is not possible as they are deflected by magnetic fields and the line of sight path is destroyed. Now the first direct evidence of cosmic ray origin has been recorded using gamma rays. Gamma rays can be produced by these high energy protons and unlike the cosmic rays they travel in straight lines, hence it becomes possible to trace back to the origin of the cosmic rays. Using NASA's orbiting *Fermi Large Area Telescope* two particular origins of cosmic rays have now been traced back to galactic supernovae remnants (SNR), designated IC443 in the constellation of Gemini and W44 near the galactic plane. An image of SN remnant W44 is portrayed in Figure 1.3. These two examples add weight to the theory that SNRs are the source of cosmic rays in external galaxies (Funk et al., 2013). But there are still doubts expressed about an understanding of the origins of cosmic rays within galaxies, that may in turn have an impact on our understanding of the source of synchrotron emission in those same galaxies (Butt, 2009).

It is calculated that only 10% of the total synchrotron can be directly attributed to supernovae remnants, the remaining 90% of diffuse radiation is coming from cosmic ray electrons permeating the galactic discs and haloes (Lisenfeld & Völk, 2000).

1.3.2 Thermal radio

Part of the radio continuum emission from galaxies is by the bremsstrahlung (free-free) mechanism. The source of this thermal radio radiation is emission from ionised gas in HII regions heated by hot young stars (Yun & Carilli, 2002). At frequencies above 30 GHz, the thermal component can be equal or greater than the non-thermal flux. Looking towards lower frequencies we see that the thermal radiation stays relatively constant while the

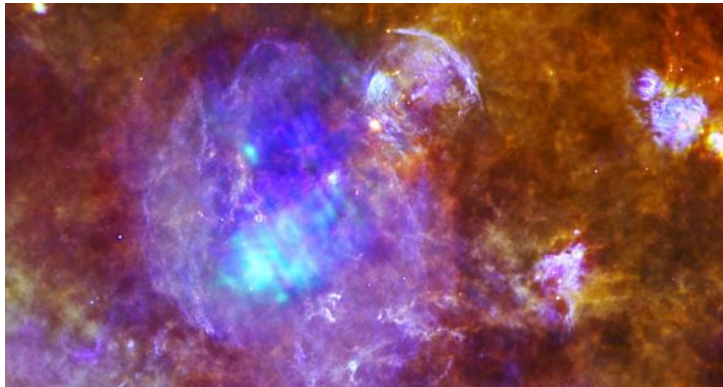


Figure 1.3: Super Nova Remnant W44 imaged by *Herschel* and *XMM* illustrating the shockwave. Credit: ESA/Herschel/HOBYS/XMMNewton

non-thermal increases with a spectral index of between 0.5 and 1.0 (Duric et al., 1988),¹. The total continuum radio emission is the sum of these two components.

1.4 Observation at radio and infrared wavelengths

Water vapour in the Earth’s atmosphere effectively absorbs infrared radiation in the wavelength range of 10 μm to 1000 μm . Ground based pioneering observations had taken place in the 1960s from a telescope at Mount Wilson in the 2.2 μm atmospheric window, finding some 20,000 individual infrared sources (Neugebauer & Leighton, 1968). During the 1970s balloons and rockets were used to get above the limits imposed by the atmosphere which only allows observations in a few narrow windows in those infrared wavebands. Observations were also made using various forms of high altitude aircraft (Longair, 2006). One of the most notable of these was the the Kuiper Airborne Observatory (KAO), operating from a modified Lockheed C-141 Starlifter from the years 1974 to 1995. Flying at high altitude (up to 48,000 feet) the KAO telescope equipped with a 36 inch mirror was capable of making observations in the 1 to 500 μm infrared spectrum (Gillespie, 1981). The opportunity to explore the whole of the infrared regime came with the launch of a series of infrared space observatories commencing in 1983 with launch of the *Infrared Astronomical Satellite (IRAS)*. This and subsequent missions have produced a wealth of data in the infrared wavelengths.

¹The spectral index α is a measure of the slope of the radio spectrum defined as $S\nu \propto \nu^{-\alpha}$

1.4.1 Infrared surveys

The first true infrared survey was undertaken following the launch of the *IRAS* in January 1983. The prime objective was an all-sky survey in four wavebands centered on 12, 25, 60 and 100 μm respectively. *IRAS* housed a relatively small telescope with a 0.6 m diameter mirror incorporating Ritchey-Chretien optics and cryogenically cooled to 2K by the evaporation of superfluid liquid Helium. The depletion of this coolant was the reason that *IRAS* ceased operations in November 1983 (Beichman et al., 1988). The main catalogue used in this thesis is the *IRAS* Faint Source Catalogue (FSC), containing data for 173,044 sources having flux densities greater than 0.2 Jy at 12, 25, and 60 μm and greater than 1.0 Jy at 100 μm (Moshir et al., 1992).

The IRAS mission found that many galaxies are strong emitters in the far-infrared, where the more intense examples are referred to as starburst galaxies (Longair, 1998). A starburst galaxy is one undergoing a brief period ($10^7 - 10^8$ year) of exceptionally high rate star formation compared with that found in the majority of galaxies and is driven by a close encounter with a nearby galaxy. This gravitational interaction fuels star formation, supplying abundant quantities of interstellar molecular hydrogen (Heckman, 2006). Luminous Infrared Galaxies (LIRG) are a class of starburst galaxies with a bolometric luminosity above $10^{11} L_{\odot}$. The most luminous class of starburst is the Ultra Luminous Infrared Galaxy (ULIRG), this is an extreme starburst with a bolometric luminosity above $10^{12} L_{\odot}$, arising from a merger with another galaxy resulting in a disturbed morphology, for example Arp 220. Many examples of these ultra luminous IR galaxies were identified in redshift surveys of IRAS galaxies (Soifer et al., 1986; Sanders et al., 1988).

The European Space Agency (ESA) *Infrared Space Observatory (ISO)* was launched by Ariane in November 1995. This infrared observatory having similar size optics to that of *IRAS* was also cooled by superfluid liquid Helium which lasted to April 1998. Whilst operational *ISO* covered wavelengths from 2.5 to 240 μm with its instruments: a camera (ISOCAM), an imaging photo-polarimeter (ISOPHOT) and a long wavelength spectrometer (LWS) (Kessler et al., 1996). *ISO* had improved sensitivity and spatial resolution over *IRAS* together with a good spectroscopic capability. This specification enabled advances in the understanding of star formation and active galaxies. Observations in the mid-infrared resolved the dust shrouded nuclei of nearby galaxies, whilst far-infrared imaging of starburst galaxies, ULIRGS and quasars revealed the presence of very cold dust components (Cesarsky & Salama, 2006).

This thesis also uses data from the *AKARI* infrared astronomy satellite, developed

by the Japan Aerospace Exploration Agency, and launched in February 2006. Operating with a mirror of 0.67 m diameter, slightly larger than carried by *IRAS* or *ISO*, *AKARI* undertook an all-sky survey over a period of 16 months from May 2006 to August 2007 in the mid-infrared and more pertinent to this thesis, in the far-infrared at 65, 90, 140 and 160 μm (Matsuhara et al., 2008; Bertout, 2010).

Herschel, the most ambitious infrared space telescope to date was launched in May 2009. This ESA space observatory carried a 3.5 m diameter mirror passively cooled using the same technology as *ISO*. As with other Infrared space observatories its operational lifetime was limited by the capacity and efficiency of the cryostat holding the superfluid helium coolant for the instrumentation. The spectral coverage of the instruments carried on *Herschel* was extended further into the far-infrared and submillimeter compared to previous missions and unlike previous missions was boosted to the 2nd Lagrangian point (L2)² where it operated from a large amplitude quasi-halo orbit (Pilbratt et al., 2010). The instrument payload comprised of three instruments: the Heterodyne Instrument for the Far Infrared (HIFI) (de Graauw et al., 2010), the Photodetector Array Camera and Spectrometer (PACS) (Poglitsch et al., 2010) and the Spectral and Photometric Imaging REceiver (SPIRE) (Griffin et al., 2010), see table 1.1. *Herschel* ceased operation on the 29th April 2013 when the helium coolant was exhausted, some months beyond the predicted date.

In this thesis I also use data from SPIRE, the 3-band imaging photometer at wavelengths of 250, 350 and 500 μm . This extends the data previously available from *IRAS* to the region beyond the peak of the far-infrared. The *Herschel* Multi-tiered Extragalactic Survey (HerMES) uses the *Herschel*-SPIRE and PACS instruments to map a set of nested fields whose locations are illustrated in Fig. 1.4. Each field is observed in six tiers from wide and shallow to deep and narrow, the chosen fields were selected from some of the most intensively observed at all wavelengths (Oliver et al., 2012). Further details are given in Chapter 5.

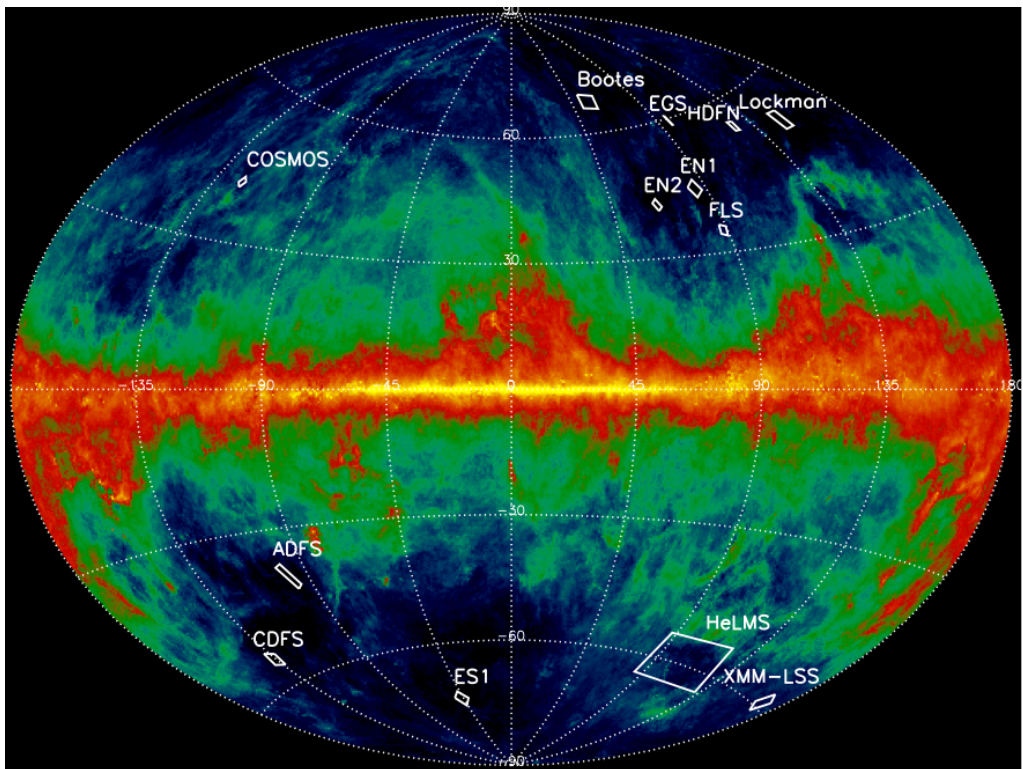
1.4.2 Radio surveys

The prime source of radio data for this thesis is the National Radio Astronomy Observatory VLA Sky Survey (NVSS). The NVSS covers the sky north of declination -40 degrees at a frequency of 1.4 GHz. Undertaken between September 1993 and October 1996 the survey

²A Lagrangian point is a location in space where gravitational forces and the orbital motion are balanced. L2 is 1.5 million km behind Earth opposite the Sun.

Table 1.1: Major *Herschel* instrumentation specifications from [Pilbratt et al. \(2010\)](#)

HIFI	Heterodyne spectrometer
Wavelength coverage	157-212 & 240-625 μm
Field-of-view (FOV)	single pixel on sky
PACS	2-band imaging photometer
Wavelength coverage	60-85 or 85-130, 130-210 μm
Field-of-view (FOV)	$0.5F\lambda$ sampled 1.75'-3.5'
SPIRE	3-band imaging photometer
Wavelength bands ($\lambda/\Delta\lambda \sim 3$)	250, 350, 500 μm
Field-of-view (FOV)	$2F\lambda$ sampled 4'x8'
SPIRE	imaging fourier transf. spectrometer
Wavelength coverage	194-324 & 316-671 μm
Field-of-view (FOV)	$2F\lambda$ sampled circular 2.6'

Figure 1.4: *The HerMES* fields illustrated here are located in regions with low dust contamination. Credit: ([Oliver et al., 2012](#))

produced a catalogue comprising 1773484 rows of discrete sources stronger than $S \approx 2.5$ mJy (Condon et al., 1998).

I also use data from the VLA FIRST Survey (Becker et al., 1995). Like the NVSS this was also undertaken at 1.4 GHz but has an angular resolution of 5 arcsec, compared to the NVSS 45 arcsec FWHM. Observations were made from 1993 to 2011 resulting in a catalogue of 946,464 sources.

To the present time there have been few low frequency surveys. One early deep survey of radio sources, the Mullard Radio Astronomy Observatory, Cambridge 8c survey at 38 MHz covers an area of about 1 steradian north of +60 degrees and contains reliable fluxes for about 5000 sources. The angular resolution of the 8c survey is 4.5×4.5 arcmin, and the limiting flux density is about 1 Jy (Rees, 1990). The most notable low frequency results come from the Very Large Array Low-frequency Sky Survey at 74MHz (VLSS). The VLSS continuum survey covers the whole northern sky above declination -10 degrees and down to -30 degrees in parts with an angular resolution of 80 arcseconds (FWHM) and a typical point source detection limit of 0.7 Jy beam^{-1} (Cohen et al., 2006). The Giant Metrewave Radio Telescope (GMRT) which is an interferometric array of dishes located near Pune, India, has made observations down to 150 MHz (see Chapter 5 for details). In general the low frequencies below 150 MHz remain poorly explored to the present time and we await new radio telescopes such as LOFAR the LOw Frequency ARray for radio astronomy to undertake large area surveys to greater depths. The LOFAR interferometric array of radio telescopes is comprised of many stations across Europe with a core centred on the Netherlands. It will be dedicated to observations at radio-frequencies below 240 MHz, in two bands down to 10 MHz with a break from 88 to 110 MHz which is dominated by terrestrial broadcasts (Falcke, 2006).

1.5 The discovery of the far-infrared radio correlation

The first indication of a general correlation between the infrared and the radio emission for star forming galaxies came in the 1970s from limited ground based observations. van de Kruit (1971) noted a correlation between the 1415 MHz radio emission from a sample of eight galaxies classified as Seyferts, and their $10 \mu\text{m}$ infrared emission. Later Rickard & Harvey (1984) make observations at 40, 50, 100 and $160 \mu\text{m}$ from the NASA Kuiper Airborne Observatory (KAO) (Cameron, 1976) and find a strong correlation with the non-thermal radio continuum emission. This association is interpreted to have a common source in young massive stars. Figure 1.5 (Condon, 1992) illustrates the FIRC for

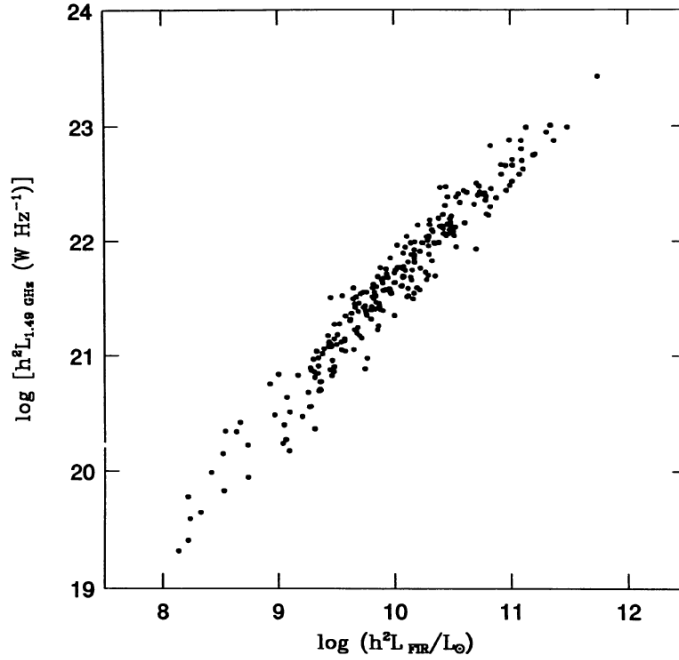


Figure 1.5: The FIR/radio correlation for sources selected at $60\mu m$ with FIR luminosity in solar units plotted against radio luminosity at 1.49 GHz. This plot excludes Seyfert nuclei. Figure (8) taken from [Condon \(1992\)](#).

strong sources in the *IRAS* Revised Bright Galaxy Sample ([Soifer et al., 1989](#)) with radio luminosity at 1.49 GHz plotted against FIR luminosity for sources selected at $60\mu m$.

Following the launch of the *IRAS* in 1983, the correlation was confirmed by [de Jong et al. \(1985\)](#) and [Helou et al. \(1985\)](#). In the intervening years to the present time the FIRC has been firmly established ([Condon, 1992](#); [Yun et al., 2001](#)) and more recently at higher redshifts where research has concentrated on specific deep fields ([Bourne et al., 2011](#); [Ivison et al., 2010](#); [Sargent et al., 2010b](#); [Seymour et al., 2009](#)). A more general FIRC study by [Morić et al. \(2010\)](#), to a redshift of 0.4, is based on *IRAS* data and the *Unified Radio Catalogue* ([Kimball & Ivezić, 2008](#)). [Jarvis et al. \(2010\)](#) have made a study of the FIRC at $0.05 < z < 0.5$. They use observations made in the Herschel-ATLAS Science Demonstration Field observed at wavelengths from $100\mu m$ to $500\mu m$ and match them to the Sloan Digital Sky Survey (SDSS) with corresponding radio data from NVSS and FIRST.

1.6 Theories of how the correlation works

The FIRC is observed primarily in star-forming galaxies therefore it has been natural to link the correlation to star-formation. The consensus at present is that two mechanisms are involved. The first of these is directly linked to the luminosity of O and B spectral class stars (Cox et al., 1986) and the second is dependant on massive stars reaching the end of their lives in a relatively short timescale of $\sim 10^8$ years (Xu, 1990).

The source of the FIR emission is dust in the interstellar medium (ISM) heated by radiation from young massive stars. Dust here refers to particles $< 1 \mu\text{m}$ in diameter similar to soot or smoke and composed of silicates or graphite (Oort & van de Hulst, 1946; Martin, 1978).

The dominant radio emission from galaxies is synchrotron radiation, this is produced by relativistic electrons accelerated in a magnetic field. Burke & Graham-Smith (2002) show that the frequency of a relativistic electron is given by

$$2\pi\nu_e = \frac{e\beta}{\gamma m_e c} \quad (1.1)$$

where

$$\beta \equiv \nu/c \quad (1.2)$$

and

$$\gamma \equiv (1 - \beta^2)^{-1/2} \quad (1.3)$$

γ is the Lorentz factor and accounts for relativistic change in mass for a moving object

The power spectrum of a single electron is given by

$$P(\nu)d\nu = \sqrt{3} \frac{e^3 B \sin \alpha}{mc^2} F(x) d\nu \quad (1.4)$$

where $x = \nu/\nu_c$

Condon (1992) shows that the spectrum of synchrotron radiation is the sum of the contribution from a large number of individual electrons with a wide range of energies. The spectrum then has an energy density given by

$$S_\nu \propto \nu^{\frac{p-1}{2}} \quad (1.5)$$

The index of the energy spectrum p observed in comic rays is 2.4 (Strong & Moskalenko, 1997). The synchrotron spectrum takes the form of a power law which declines with increasing frequency and with $p \simeq 2.4$ is approximately

$$S_\nu \propto \nu^{-0.7} \quad (1.6)$$

The exponential term in Eqn. 1.6 is the spectral index α as defined in the Chapter 2 section on radio k -correction.

The radiation spectra for a range of electron energies is expected to be of the form $N(E)dE = kE^{-p}dE$ where $N(E)dE$ is the number of electrons in the energy interval E to $E+dE$ (Longair, 1994).

The synchrotron emissivity is a function of the magnetic field strength and the number density of relativistic electrons, where the luminosity at a frequency ν is given by

$$I(\nu) = \text{const} LN_0 B^{(p+1)/2} \nu^{-(p-1)/2} \quad (1.7)$$

where N_0 is the density of relativistic electrons, B is the magnetic field strength and L is the emission depth (Davies & Wilkinson, 1998).

The spectral index of luminous radio galaxies is observed to steepen at the high frequency end of the radio spectrum in a process known as spectral ageing. This effect is thought to be the result of high-energy electrons becoming depleted as they efficiently produce synchrotron radiation in comparison to those electrons with relatively lower energy (Chandra et al., 2004). Spectral ageing is seen to occur in the lobes of radio galaxies where the spectral index is observed to become increasingly steep from the the centre of the host galaxy towards the outer lobes. This change in spectral index in the lobes of radio galaxies is used to estimate their ages (Siah & Wiita, 1990).

One of the early theories proposed to account for the remarkably tight FIRC is the calorimeter theory of Völk (1989). In the calorimeter theory it is posited that galaxies act as calorimeters trapping all the relativistic electrons responsible for the synchrotron radiation whilst also being optically thick for stellar UV photons to be efficiently converted and re-radiated in the far-infrared by interstellar dust grains. Völk assumes that both of these mechanisms responsible for the radio synchrotron and far-infrared emissions are proportional to the supernova rate. The implication of this theory is that the FIRC is the result of chance balance of the UV radiation to the synchrotron emission. Evidence against the calorimeter theory is seen in the radio spectral indices. Theory predicts radio spectral indices $\alpha \approx 1 - 1.2$ but the observed α are in the range $0.7 - 0.8$ believed to be a result of synchrotron and inverse Compton cooling (Condon, 1992).

In contrast to the calorimeter theory Helou & Bicay (1993) propose a model centred on a ‘conspiracy’ whereby an assumption is made that the diffusion, decay and strength of cosmic ray electrons responsible for synchrotron emission matches the emission of dust-

heating photons i.e radio-emitting cosmic-ray electrons are required to be created in constant proportion to the UV emission as a normal function of star-formation activity.

[Niklas & Beck \(1997\)](#) only expect a maximum $\approx 50\%$ of galaxies to conform to the calorimeter theory. They propose a mechanism which can continue to support the FIRC in non-calorimeter galaxies. One factor considered is the average volume density of the gas and its relationship to the strength of the magnetic field. Secondly, thermal radio emissivity is taken as a measure of the star formation rate (SFR) whilst assuming that the FIR luminosity is related to the SFR.

Utilising observations of M31 [Hoernes et al. \(1998\)](#) split the observed FIR emission into warm and cool components, and similarly split the radio into thermal and non-thermal components. The FIRC is expected for the warm FIR and the thermal radio since these are common to massive ionising stars, whereas the cool FIR and the non-thermal radio do not have a dependence on a common energy source. The cool dust is heated by the interstellar radiation field and the non-thermal radiation has supernovae as a precursor. An alternative proposal to explain the FIRC for this latter case is proposed, whereby the magnetic field is coupled to the gas which is mixed with the cool dust.

[Bell \(2003\)](#) revisits the conspiracy theory and points out that both indicators of star-formation, the radio emission and IR from low luminosity galaxies underestimate the actual star-formation rate. Thus [Bell](#) finds that there is still the need to invoke the ‘conspiracy theory’ to account for the linear relation.

[Lacki et al. \(2010\)](#) give the following explanation for the FIRC:

‘The FIRC is caused by a combination of the efficient cooling of CR electrons (calorimetry) in starbursts and a conspiracy of several factors. For lower surface density galaxies, the decreasing radio emission caused by CR escape is balanced by the decreasing FIR emission caused by the low effective UV dust opacity. In starbursts, bremsstrahlung, ionisation, and inverse Compton cooling decrease the radio emission, but they are countered by secondary electrons/positrons and the dependence of synchrotron frequency on energy, both of which increase the radio emission’.

Table 1.2 outlines some of the theories put forward to explain the correlation. There are many questions posed by this collection of theories. The calorimeter theory requires cosmic ray electrons to lose most of their energy in the form of synchrotron radiation, whilst also being optically thick such that most of the UV light is converted to FIR. The problem here is that not all galaxies are optically thick so the calorimeter theory is in

doubt. Even if the theory holds for some galaxies there is a conflict with observations. The radio spectral index α of star-forming galaxies ($\sim 0.7 - 0.8$) suggests according to [Lacki et al. \(2010\)](#) that electrons escape before all their energy is converted to synchrotron radiation, if conversion were efficient α would be expected to be closer to $\sim 1.0 - 1.2$.

Non-calorimeter theories have to invoke a large dynamic range in physical properties to account for the FIRC although [Thompson et al. \(2006\)](#) do suggest that the calorimeter theory can hold if the radio spectra is cooled by ionisation and bremsstrahlung.

At this time none of the preceding theories provide a comprehensive explanation of the FIRC.

1.7 Evolution in the FIRC

It is not known at the present time whether the FIRC evolves with redshift, although this is a probability with several major factors that are expected to come into effect with increasing look-back time:

1. Changes in the SEDs of high redshift galaxies in terms of dust or metallicity ([Bourne et al., 2011](#)).
2. Quenching from the CMB whereby inverse Compton scattering suppresses synchrotron radiation by limiting the life time of relativistic electrons. This synchrotron quenching is predicted to occur beyond $z=2$ ([Blain et al., 2002](#)).
3. The effect of hot intra-cluster gas in dense environments: Winds in the intra-cluster medium have the potential to raise the synchrotron power by driving shocks into the inter-stellar medium ([Murphy et al., 2009](#)).

The question of evolution in the FIRC has been central to many research papers. In the last few years various differing results have been presented, here I summarise some of the principle results.

- [Garrett \(2002\)](#) Shows that the FIRC holds to a redshift of $z \approx 1.3$.
- [Ibar et al. \(2008\)](#) Show that the FIRC holds to a redshift of $z \approx 3.5$
- Using *Spitzer MIPS* 70 μm data [Seymour et al. \(2009\)](#) find a gradual decrease in q_{70} for star forming galaxies with increasing redshift.

Table 1.2: Theoretical models attempting to explain the FIR-radio correlation

Author	Model Assumptions
Völk (1989)	Calorimeter model: Massive stars powering both radio and FIR emissions.
Helou & Bicay (1993)	Model considers the diffusion, decay and strength of CR electrons responsible for synchrotron emission. An assumption is made that dust-heating photons and radio-emitting cosmic-ray electrons are created in constant proportion.
Niklas & Beck (1997)	Dependence on the magnetic field strength and the star formation rate.
Hoernes, Berkhuijsen & Xu (1998)	The nonthermal-radio/cool-dust correlation arises because of a coupling of the magnetic field to the gas which is mixed with the cool dust.
Bell (2003)	The linear relation is ‘a conspiracy’ since both the IR and radio underestimate the star formation rate at low luminosities.
Lacki, Thompson & Quataert (2010)	Calorimetry, Conspiracy, and Implications: Model indicates that FIR and radio emissions keep a constant ratio, by differing mechanisms for low surface density galaxies compared to starburst galaxies.

- Also using *Spitzer MIPS* 24 and 70 μm and VLA 1.4 GHz data [Sargent et al. \(2010a\)](#) find that the FIRC remains unchanged out to $z\sim 1.4$.
- In a second paper using *Spitzer MIPS* 24 and 70 μm and VLA 1.4 GHz data [Sargent et al. \(2010b\)](#) observe that Ultra Luminous Galaxies (ULIRGS) and infrared bright galaxies show no change in their average FIRC values out to a redshift of $z\sim 2$ when they apply a bias correction.
- Using *Herschel-ATLAS* and VLA FIRST [Jarvis et al. \(2010\)](#) find no evidence for evolution in the FIRC over the redshift range $0 < z < 0.5$.
- [Morić et al. \(2010\)](#) find that Seyfert galaxies have FIRC ratios lower than the canonical values due to possible active galactic nuclei (AGN), but that galaxies containing AGN in their sample do fit the FIRC having ratios indistinguishable from star forming galaxies.
- [Iverson et al. \(2010\)](#) find that there is no evidence that q_{IR} changes with any significance between $0 < z < 2$
- [Bourne et al. \(2011\)](#) observe that the FIRC does not significantly change over the redshift range of $0 < z < 2$ when using k -corrected 24 or 160 μm fluxes. But they do observe a decline in the FIRC with 70 μm fluxes beyond $z\sim 1$.
- [Mao et al. \(2011\)](#) report no evidence for evolution in the FIRC at 70 μm for star-forming galaxies out to $z > 2$

It can be seen from the above summary that it is generally accepted that there is no evidence for evolution in the FIRC with redshift with the exception of that reported by [Seymour et al. \(2009\)](#).

1.8 Application of the FIRC

The far-infrared - radio correlation (FIRC) is now regarded as a ‘main sequence’ for star forming galaxies revealing many important galaxy properties. The universality of this correlation has been accepted as a tracer of star formation in starburst galaxies with the potential to indicate galaxy types, ranging from normal star forming to active galactic nuclei. It is possible to identify AGN by looking for galaxies with high radio (excess) ([Donley et al., 2005](#)). [Oyabu et al. \(2005\)](#), show that the correlation can pinpoint co-ordinates for optical identifications of far-infrared sources by utilising followup radio observations to

obtain precise co-ordinates. Originally found to apply to nearby star forming galaxies, the FIRC is becoming accepted for fundamental applications such as the determination of redshift. [Mao et al. \(2011\)](#) suggest that it is possible to use the FIRC to estimate the distance of galaxies when no optical counterpart is available and [Carilli & Yun \(1999\)](#) have estimated the redshift of submillimeter galaxies using the radio to submillimeter spectral index ($\alpha_{1.4}^{350}$). In their study of star formation history [Haarsma et al. \(2000\)](#) detect star-forming galaxies at high redshift, then use the FIRC to directly predict the star-formation history from these radio observations assuming that the FIRC holds to these redshifts.

At the present there is little evidence of any breakdown in the FIRC. With reliance on the correlation becoming routine there is a need to know if there are limits to its reliability. The correlation is expected to break down at some point, therefore an understanding of any limitations is becoming increasingly necessary. This is especially true at high redshifts where it will impact on the up and coming LOFAR and Square Kilometre Array (SKA) radio surveys.

1.9 Outline of the thesis

This thesis considers the possible evolution in the Far-Infrared - Radio Correlation (FIRC) of mainly low redshift ($z < 0.5$) galaxies, in terms of either redshift or luminosity using a large sample of objects. The possibility of the FIRC being related to galaxy temperature is also investigated. In this thesis I extend the Far-infrared radio ratio beyond radio observations made at 1.4 GHz down to lower radio frequencies, using data from the VLA and GMRT. The main thrust of this thesis is to learn more about a correlation that is perplexingly consistent by studying the q parameter in great detail, examining departures from the canonical q . The correlation has become one of the underlying foundations of modern astronomy, therefore it is important to know if the relationship breaks down at high luminosities or varies with redshift or radio frequency. The FIRC is expected to breakdown at some at some point possibly since it is highly unlikely that the conditions responsible for this remarkably linear correlation can stay in perfect balance at all redshifts in all relevant galaxy types.

This thesis is organised as follows. In this chapter I review the history and current theories of galaxy formation and the mechanisms of the FIRC as presently understood and explain why it is expected to breakdown at some point. Chapter 2 is a close examination of the FIR radio correlation at 1.4 GHz, using a large sample of galaxies. Chapter 3 looks at FIRC as a function of temperature for warm and cold samples. Chapter 4 examines the

FIR radio correlation of low radio frequency selected samples as a precursor to analysis with LOFAR data. Chapter 5 examines the FIR radio correlation in the ELAIS-N1 field at 610 and 325 MHz using HerMES, GMRT and SPITZER data. Chapter 6 Conclusions and summary of this thesis and prospects for future work.

Chapter 2

The Far-Infrared - Radio Correlation at 1.4GHz

2.1 Introduction

In this chapter I examine the Far-Infrared-Radio Correlation (FIRC) at low redshift with a large, ($\sim 11,000$) object catalogue complete with spectroscopic or photometric redshifts. This is larger than previous catalogues used by others to test the FIRC and samples a significant proportion of the low redshift population ($z < 0.5$). Within this sample our understanding of the FIRC will be statistically more significant and will have increased precision when estimating the properties of star-forming galaxies.

The FIRC is quantified by the q parameter, originally defined by [Helou et al. \(1985\)](#) as the log ratio of the total far-infrared to radio emission at 1.4 GHz. The Log far-infrared - radio flux ratio is examined using the Helou formula equation 2.4 ([Helou et al., 1985](#)), where FIR is defined as the radiation between 42.5 and 122.5 μm derived from the 60 and 100 μm *IRAS* bands and the radio flux density is measured at 1.4 GHz. I next calculate q_{L60} which quantifies the FIRC as the logarithmic ratio between the rest-frame luminosity (L_{IR} at 60 μm) and the rest-frame radio luminosity ($L_{1.4\text{GHz}}$), see Equation 2.14. Finally q is evaluated following the definition in [Sanders & Mirabel \(1996\)](#) where L_{TIR} is the integrated infrared luminosity from 8-1000 μm , Appropriate cuts are applied to minimise selection effects. Kaplan-Meier statistics are employed to account for upper limits in the radio sample in the quest to confirm or refute evolution in q in terms of redshift or luminosity. For all three methods q is evaluated with respect to both redshift and luminosity. The q parameter is described in greater detail in section 2.3.

Early investigations into the far-infrared radio correlation were made using relatively

Table 2.1: Fir-radio correlation of specific fields

Authors	Year	Field	Sample size
Garn and Alexander	2008	xFLS	2298
Seymour et al	2009	XMM Newton/Chandra	488
Sargent et al	2010	COSMOS	4500
Iverson et al	2010	GOODS-North	652
Bourne et al	2010	ECDFS	3529
Jarvis et al	2010	Herschel-ATLAS SDF	2334
Huynh et al	2010	HDFS	495
Mao et al	2011	ECDFS	617

SDF fields : GOODS-N, Lockman-N, Lockman-SWIRE, FLS ([Levenson et al., 2010](#))

small samples as reported in [Helou et al. \(1985\)](#) with 28 galaxies, [Devereux & Eales \(1989\)](#) with 237 and Condon, Anderson and Helou (1991) with 313. In [Yun, Reddy & Condon \(2001\)](#), q is calculated for a sample of 1809 galaxies with both *IRAS* infrared and 1.4 GHz radio fluxes. This sample has a redshift coverage out to $z \approx 0.15$ and the mean q -value for the whole sample was found to be 2.34 ± 0.01 . One of the major results from early work was the demonstration of a very tight correlation between the far infrared and radio luminosities that held over many decades. These early studies of Virgo galaxies by [Helou et al.](#) and large nearby galaxies by [Condon et al.](#), did not exhibit signs of evolution, although it is expected that the FIRC will break down at some critical high redshift. One possible mechanism is the cooling of relativistic electrons by Compton scattering off Cosmic Microwave Background photons, thus eventually dominating over radio emission via synchrotron radiation ([Ghisellini et al., 2013](#); [Schleicher & Beck, 2013](#)).

Table 2.1 lists recent examinations of the FIRC by various authors, these are restricted in area to mainly less than one square degree and limited to specific deep fields. In this chapter I have taken a large sample of *IRAS* galaxies to investigate the possibility of evolution in terms of either redshift, luminosity or both. q values are divided into luminosity and redshift bins across the full sample.

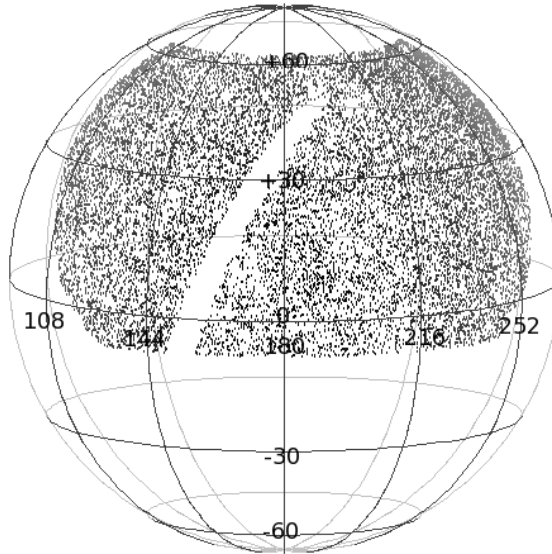


Figure 2.1: The contiguous sample area defined by a major part of the *VLA* First survey. The extremities of the RA boundary run from 105.2 to 266.6 degrees, and the declination from +64.6 down to -8.0 degrees. See section 2.2.3 for description of void.

2.2 Data selection

2.2.1 The IIFSCz catalogue

The primary sample is sourced from the *Imperial IRAS-FSC Redshift Catalogue (IIFSCz)* by Wang & Rowan-Robinson (2009). The *IIFSCz* catalogue is comprised of a sample of 60,303 IRAS galaxies selected from the *IRAS Faint Source Catalogue (FSC)*, each source has four photometric points at 12, 24, 60 and 100 μm . Approximately two thirds of galaxies in this catalogue have associated 1.4 GHz radio fluxes. This large catalogue has associated redshifts for around 75% of the galaxies, 55% of these are spectroscopic, the remaining 20% are photometric, being derived by training set methods or Spectral Energy Distribution (SED) fitting from optical and near-infrared broad band photometry. The catalogue columns include the *IRAS* source name and flux density, integrated 1.4 GHz flux density, spectroscopic and photometric redshift, the adopted redshift, optical galaxy template type, luminosity fractions from cirrus, M82, AGN and Arp220 infrared templates, predicted fluxes from 12 to 1380 μm . This catalogue was assembled for use in the validation of large infrared surveys such as *Herschel* and provides an excellent source for re-examination of the far-infrared radio correlation with a large database.

2.2.2 The radio data

In the *IIFSCz* catalogue, radio data is drawn solely from the VLA *NVSS* survey with only 40% of those galaxies having an associated 1.4 GHz flux density. The *NVSS* is a radio continuum survey covering the sky north of -40 declination at 1.4 GHz. with a relatively large beam size of 45 arcsec Full Width Half Maximum (FWHM), suited to observing objects at low redshift (Condon et al., 1998). In contrast the VLA *FIRST* has a beam size of 5.4 arcsec FWHM (Becker et al., 1995). By inspection of the *NVSS* and *FIRST* catalogues I have determined that the flux densities overlap at $z \simeq 0.2$. Where *NVSS* data is absent from the *IIFSCz* catalogue I supplement *NVSS* radio fluxes with 1.4 GHz fluxes from the *FIRST* survey, adopting the selection method outlined in Jarvis et al. (2010), whereby objects at $z < 0.2$ are primarily selected as *NVSS* sources, and objects above $z > 0.2$ are primarily selected from the *FIRST* catalogue. This effectively filled the gaps in radio data for the higher redshift sources where the *IIFSCz* catalogue is deficient.

Matching the *IIFSCz* catalogue to the VLA *FIRST* catalogue was achieved with TOPCAT, the Tool for Operations on Catalogues and Tables (Taylor, 2005). The matching radius was set to 5 arcsec to match the *FIRST* beam size of 5 arcsec. The match results output by TOPCAT are expected to have a low probability of being false since the galaxies in the *IIFSCz* catalogue are cross-matched with a number of databases, most notably the NASA/IPAC Extragalactic Database(NED) and point sources at the detection limit of the *FIRST* catalog have positions accurate to better than 1 arcsec (White et al., 1997). I therefore expect a very low false matching rate (FMR). Future work could test for false matches by introducing offsets in co-ordinates.

2.2.3 Data Sample Boundary

The footprint was chosen such that it avoided the galactic plane and was fully covered by both radio and infrared surveys, the *NVSS*, Faint Images of the Sky at Twenty centimetres *FIRST* (White et al., 1997) and the *IRAS* Faint Source Catalogue. The Sloan Digital Sky Survey *SDSS* (Abazajian et al., 2009) is additionally used to verify positions of sources. The sample area is illustrated in Fig. 2.1 and is bounded by $105.2^\circ \leq \text{Dec} \leq 266.6^\circ$ and $+64.6^\circ \leq \text{RA} \leq -8.0^\circ$. Within this area can be seen the void in the *IRAS* data, there are two such strips on opposite sides of the galactic plane in the full survey approximately 5° wide by 60° long which were not observed at the allotted time due to observational difficulties, unfortunately the liquid helium coolant did not last long enough for this area to be revisited (Emerson et al., 1985). By choosing an area bounded by *FIRST*, the

smallest of all the aforementioned surveys that also sits within the defined boundary, I ensure complete coverage in each wavelength both radio and infrared.

The sample for this chapter covering an area sky of $\sim 5,000 \text{ deg}^2$, was primarily taken from the *IIFSCz* catalogue and bounded by the footprint illustrated in Fig. 2.1, comprising a total of 17,044 *IRAS* sources complete with either spectroscopic or photometric redshifts. Not all of these sources were complete with radio flux densities. By following the method outlined in section 2.2.2 I added or replaced *NVSS* sources where $z > 0.2$, and additionally over the whole redshift range *FIRST* sources were inserted in the catalogue where there was no pre-existing *NVSS* source. This increased the number of sources with 1.4 GHz data to $\sim 63\%$, yielding a final number of catalogue sources complete with 1.4 GHz radio data of 10,833.

The *NVSS* catalogue has a completeness limit of $S \approx 2.5 \text{ mJy}$ (Condon et al., 1998). I have accordingly made a conservative estimate for the radio upper limit, setting this at 2.0 mJy. The remaining sources from the *IIFSCz* catalogue in my data sample having no recorded radio flux, were then set to this upper limit boundary of 2.0 mJy. The detection limit of VLA *FIRST* over the majority survey area is 1.0 mJy (White, 2014). This opens the possibility to lower the radio upper limit for the *FIRST* selected sample, although in this present work I have opted to retain the 2.0 mJy for both *NVSS* and *FIRST* galaxies.

2.3 Quantification of the Far-Infrared-Radio Correlation

The dimensionless parameter “ q ”, introduced by Helou et al. (1985), is defined as the logarithmic ratio of the far-infrared to the radio emission. In its simplest form q is quantified in the observed frame as

$$q = \log_{10} \left(\frac{S_{\text{IR}}}{S_{\text{radio}}} \right) \quad (2.1)$$

where the observed infrared flux density is represented by S_{IR} and S_{radio} is the observed radio flux density. q can also be quantified as the logarithmic ratio between a rest-frame infrared flux and rest-frame radio flux. The monochromatic q_{IR} , Equation 2.2, is taken from Appleton et al. (2004) where it quantified q_{IR} for high redshift sources in the xFLS field where S_{IR} is the flux density in the 24 or 70 μm wavebands.

$$q_{\text{IR}} = \log_{10} \left(\frac{S_{\text{IR}}}{S_{1.4 \text{ GHz}}} \right) \quad (2.2)$$

Helou et al. (1985) introduced a pseudo-bolometric method of calculating q where *IRAS* 60 and 100 μm flux densities in Jy are combined to estimate the total FIR flux between 42.5 and 122.5 μm

$$FIR = 1.26 \times 10^{-14} (2.58S_{60\mu\text{m}} + S_{100\mu\text{m}}) \text{W m}^{-2} \quad (2.3)$$

then

$$q_{\text{FIR}} = \log_{10} \left(\frac{FIR}{3.75 \times 10^{12} \text{W m}^{-2}} \right) - \log_{10} \left(\frac{S_{1.4\text{GHz}}}{\text{W m}^{-2} \text{Hz}^{-1}} \right) \quad (2.4)$$

In the Equation 2.4, 3.75×10^{12} Hz is the applied normalising frequency of 80 μm and the radio flux at 1.4 GHz is k -corrected to the rest-frame (section 2.9 for details of k -correction methods). The Helou formula has the limitation that it can underestimate the total far-infrared emission since it does not depend on the actual SEDs of the individual galaxies but approximates the flux density that would be seen by an ideal square passband 80 μm wide centered on 82.5 μm (Fitt et al., 1988).

Uncertainty in the FIR comes from an incomplete understanding of the spectral behaviour at 60 and 100 μm for galaxies at temperatures colder than 30K. Additionally the flux densities of some nearby galaxies may not be fully sampled and thus the FIR underestimated if they exceed the field of view of *IRAS* (Cox et al., 1988). The FIR which is estimated by Equation 2.3 is only true if the far-infrared flux peaks in this defined passband. Emission at shorter or longer wavelengths is not accounted for, thus the FIR flux will not be overestimated with this sampling window (Nagata et al., 2002).

A further variant of q is that of q_{TIR} , where the infrared flux is the calculated total infrared flux between the wavelengths of 8 and 1000 μm , that can be determined from *IRAS* 12, 25, 60 and 100 μm fluxes by applying the formula given in Appendix B of *Cataloged Galaxies and Quasars Observed in the IRAS Survey* (Fullmer & Lonsdale, 1989), thus

$$TIR = 1.8 \times 10^{-14} (13.48S_{12\mu\text{m}} + 5.16S_{25\mu\text{m}} + 2.58S_{60\mu\text{m}} + S_{100\mu\text{m}}) \text{W m}^{-2} \quad (2.5)$$

then as defined in Sanders & Mirabel (1996)

$$q_{\text{TIR}} = \log_{10} \left(\frac{TIR}{3.75 \times 10^{12} \text{W m}^{-2}} \right) - \log_{10} \left(\frac{S_{1.4\text{GHz}}}{\text{W m}^{-2} \text{Hz}^{-1}} \right) \quad (2.6)$$

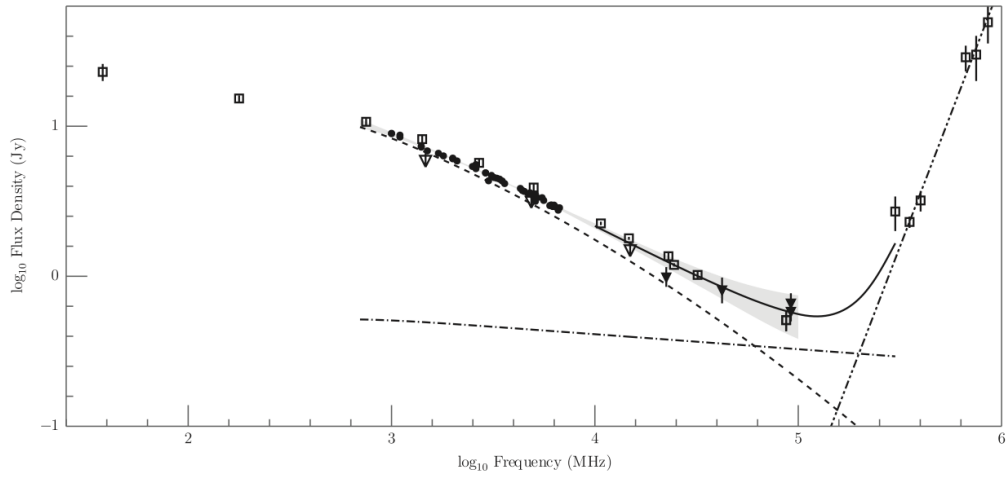


Figure 2.2: The radio spectrum of M82 compiled from measurements made by various telescopes. Taken from Figure 8 in [Williams & Bower \(2010\)](#). The dashed line represents the model non-thermal spectrum while the dot-dashed line extending to below 1 GHz represents the model thermal contributions. The solid line is the sum of the thermal and non-thermal contributions. In this thesis the M82 spectrum is extrapolated to fit the three lowest frequency data points.

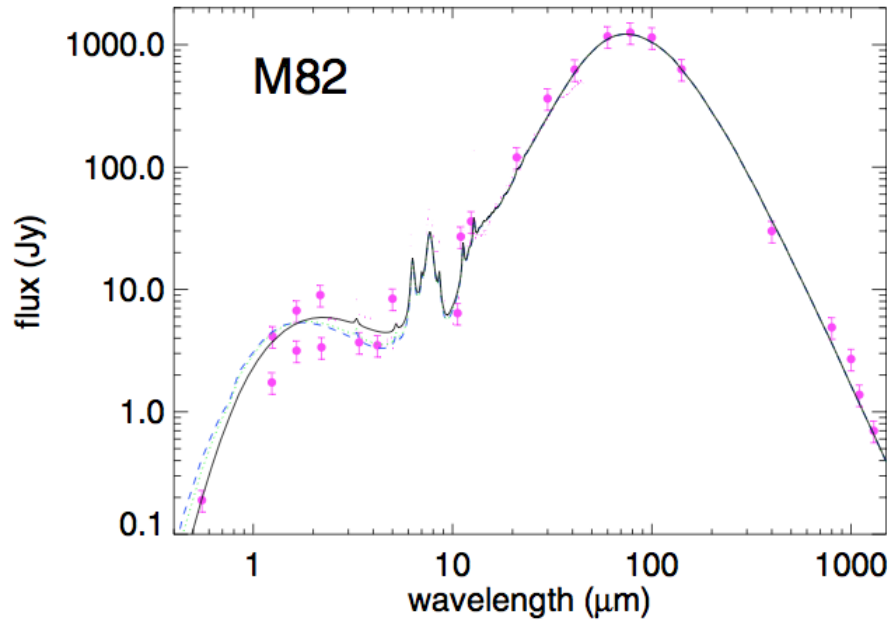


Figure 2.3: Restframe M82 infrared SED from [Siebenmorgen & Krügel \(2007\)](#)

The radio spectrum of M82 is exploited to calculate the radio luminosity of starburst galaxies. M82 has been extensively observed in the 1 - 10 GHz range, see Figure 2.2 from Williams & Bower (2010). This radio spectrum shows observations defining the combined synchrotron and thermal spectra, where the dot dashed line depicts the predicted thermal spectra, and the dashed line is the predicted non-thermal spectra. The dot dot dashed line on the right is the predicted far-infrared spectra. There have been few low frequency large area surveys, the most notable being the 74 MHz VLA *VLSS* survey covering the entire sky north of -30 degrees declination (Cohen et al., 2006), other surveys used to complement the low frequency end of this SED are the Texas Survey at 365 MHz (Douglas et al., 1996), the 6c Survey at 151 MHz Hales et al. (1991) and the 8c Survey at 38 MHz Hales et al. (1994).

Ideally q is calculated with the total infrared luminosity and the total radio luminosity. This is problematic for a large sample of galaxies and requires a good knowledge of the spectral energy distribution in both regimes. There is a problem when only some percentage of galaxies detected by *IRAS* have corresponding radio detections with either VLA *NVSS* or *FIRST*. Here the aim is to determine the best quantification of q for the sample of infrared selected star forming galaxies. When associated radio detections are not available we are subsequently limited in the number of objects available for statistical analysis. To improve the estimation of the true q value, upper limits for the radio flux are introduced for all sources without a detection in the radio. Then subsequent to the determination q by any of the methods outlined survival analysis is used to return a more representative value, this is discussed further in section 2.3.4

2.3.1 K-corrections

Helou et al. (1985) calculated q with observed frame Far-infrared and radio flux densities, see Equations 2.3 and 2.4, this is adequate for monochromatic flux densities at relatively low redshifts. To investigate the evolution of q to higher redshifts it becomes important to correct from the observed frame to the rest-frame. In order to achieve this a k -correction is applied which accounts for the lowering in frequency of the emitted flux densities due to the individual redshift distances of each discrete source. A flux density S detected at the observed frequency ν_0 was emitted at frequency ν_e by the source where

$$\nu_e = (1 + z)\nu_o \quad (2.7)$$

Radio k -correction

The radio emission spectra of star-forming galaxies at frequencies ≤ 100 GHz, are the product of synchrotron and thermal emissions. At frequencies ≤ 10 GHz synchrotron becomes the dominant emission. The radio spectra of these galaxies follows the power law $S\nu \propto \nu^\alpha$ to frequencies ≈ 1 GHz, where α is the radio spectral index given by

$$\alpha = \frac{\ln(S_1/S_2)}{\ln(\nu_1/\nu_2)} \quad (2.8)$$

S_1 and S_2 are flux levels at two distinct frequencies, for example 610 MHz and 1.4 GHz. α is typically taken to be around -0.7 to -0.8 for star-forming galaxies (Condon, 1992). At some undetermined frequency below 100 MHz the spectra is expected to depart from being linear and to turn over from possessing a negative spectral index to having a positive spectral index, this can be attributed an expected absorption of the synchrotron radiation (for details see chapter 4). Throughout this thesis a spectral index of -0.8 is used unless otherwise stated.

The k -correction term is given by

$$k = (1 + z)^{-\alpha} \quad (2.9)$$

and the luminosity of a source at redshift z is then given by

$$L_{\text{radio}} = \frac{4\pi D_L^2}{(1 + z)^{1+\alpha}} S_{\text{radio}} \quad (2.10)$$

where D_L is the luminosity distance and the observed radio luminosity is converted to a rest-frame luminosity by the addition of the k -correction term that ‘corrects’ for observed sources being at different rest-frame wavelengths due to their redshifts with respect to the observer (Hogg et al., 2002)

Infrared k -correction

In the infrared regime a power law is no longer valid for k -correction, it is now necessary to employ one or more spectral energy distribution (SED) templates representing typical starburst galaxies. The most commonly used are those of M82, a closely studied local starburst galaxy or that of Arp220, a galaxy seen to be the product of two galaxies in the act of merging and is classed as an Ultra-luminous Infrared Galaxy (ULIRG). In Figure 2.4

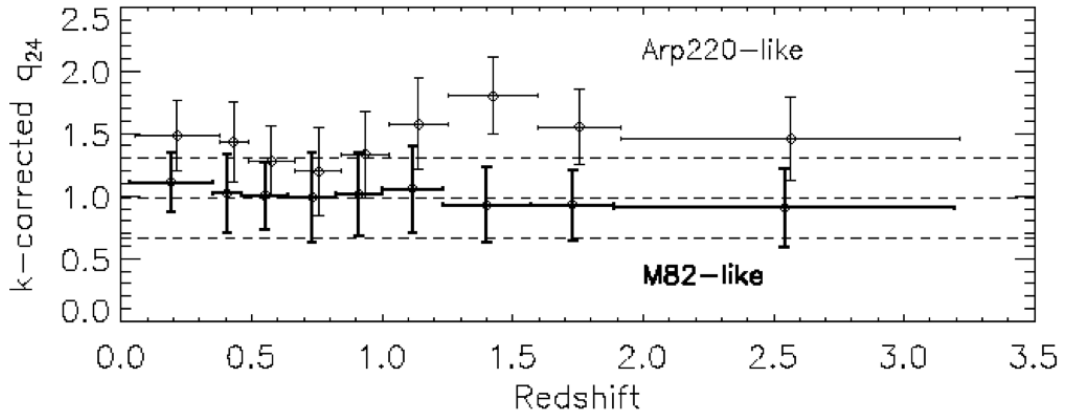


Figure 2.4: k -corrected $24 \mu\text{m}/1.4 \text{ GHz}$ correlation reproduced from Ibar (2008a) illustrates a greater deviation in q values above redshifts of 1.0 when using an Arp220-like template compared to an M82-like template (Note: Arp220 results slightly shifted to improve visualisation.)

reproduced from Ibar (2008a) a comparison is made between an Arp220-like and an M82-like template when used for k -correction. The plot depicts a larger deviation in calculated q values for galaxies at redshifts higher than $z=1$ when using the Arp220 template.

IR SED libraries are available such as those presented by Chary & Elbaz (2001); Dale & Helou (2002); Lagache et al. (2003) and Magdis et al. (2012), although where there are only one or two flux data points available for the fit I have restricted the selection to the Siebenmorgen & Krügel M82 SED illustrated in Figure 2.3. When calculating total infrared luminosities where there are more than two photometric points I use the IDL fitting procedure by Casey (2012). In this routine fitting is achieved by comparing (at least three) available data points to SEDs in a selection of libraries as aforementioned thus achieving a ‘best fit’ for each galaxy with the benefit of selecting the most appropriate SED.

2.3.2 Removal of AGN

I am primarily interested in normal star-forming galaxies and therefore aim to eliminate AGN from the sample unless they appear to have predominantly starburst characteristics in both their infrared and radio emissions. Typical galaxy types in question here are those classified as Seyfert, radio loud and radio quiet quasars. Sopp & Alexander (1991) have shown that radio-quiet quasars and Ultra Luminous Infrared galaxies (ULIRGS) both follow the FIRC, whereas they found that radio-loud quasars look similar to radio

galaxies, with an output predominantly in the radio wavebands. If the dominant process in any of these galaxy is starburst then they will be expected to have a q near to the mean of 2.34 determined for ‘normal’ star-forming galaxies by Yun et al. (2001). The radio flux is expected to be higher in radio loud AGN and they will reveal themselves by their offset from the mean q . For sources found to have a q of less than 1.8, i.e. galaxies that are more than 3 times more radio loud than normal star-forming galaxies (Condon et al., 2002)) a cut is applied, removing these sources with a radio excess eliminates the possibility of contamination from radio loud AGN.

Some ellipticals can be distinguished from star-forming spirals by their lower levels of far-infrared emission (Condon, 1998). A radio selected elliptical galaxy therefore may not be detected as an infrared source at say 60 μm . The radio continuum fluxes exhibited by some ellipticals are higher than found in spiral star-forming galaxies and are thought to be non-thermal in origin being powered by an AGN (Goudfrooij, 1997). This class of ellipticals will not fit the FIRC although as Figure 2.8 shows a large number of ellipticals, classified by their morphology (Wang & Rowan-Robinson, 2009) do fall close to the median of star-forming galaxies. The cut in q applied to remove AGN also removes these radio loud ellipticals, all other ellipticals are retained.

2.3.3 Volume Limited Samples

To ensure that the calculated q is a true representation at any redshift or luminosity within our sample it is necessary to avoid selection effects. At progressively higher redshifts the higher luminosity objects will be dominating the sample, therefore we need a defined strategy to construct volumes in luminosity and redshift that are as complete as possible.

An attempt to overcome this disadvantage is made by applying volume limited samples. Using volume limited samples has the disadvantage of inherently smaller samples. If the volumes are divided into redshift bins the low redshift bins will be more complete than the high redshift bins where the high luminosity objects will dominate. In the case of luminosity bins the q values will also not reflect the mean value of the whole sample. We attempt to overcome these limitations by applying survival analysis techniques to each volume bin then determining the mean q for the whole sample (see section 2.3.4).

While there are limitations in redshift range in the sample it is possible to probe a range of luminosities. Sargent et al. (2010b) have found that q is not evolving with redshift, this can be confirmed at low redshift and will allow a search for evolution in terms of luminosity.

2.3.4 Survival analysis

Survival analysis techniques were originally developed in the medical field to predict patient survival rates when deaths occurred randomly throughout a study period. In that particular case the data was said to be right censored. The Kaplan-Meier estimator as presented by [Feigelson & Nelson \(1985\)](#), is one formalisation of survival analysis techniques which provides a maximum likelihood reconstruction of the distribution function. The Kaplan-Meier (KM) method has been adapted to accommodate left censored data, where some fraction of a sample is not detected, specifically in this instance, the non-detection of radio at 21 cm for sources with FIR detections. The KM method applied in this situation provides an unbiased estimate of the mean by taking into account these radio upper limits.

Variables used in calculation of the KM mean for data set comprised of a mixed ‘good’ and left centred data are

x^L , the uncensored data list, ranked max to min.

n_j the total number of data points including censored points below each x^L value

d_j the total number of identical data points ranked max to min.

where the distribution function

$$\hat{F}(x_{j=1}) = 1 \quad (2.11)$$

then for $j=1$ to n

$$\hat{F}(x_{j+1}) = \hat{F}(x_j) \left(1 - \frac{d_j}{n_j} \right) \quad (2.12)$$

we now estimate the mean

$$\mu = \sum_{j=1}^n x_j^L [\hat{F}(x_j^L) - \hat{F}(x_{j-1}^L)] \quad (2.13)$$

This method is adapted from [Beal \(2010\)](#) following the method of [Feigelson & Nelson \(1985\)](#). My IDL KM code following this method is listed in appendix [A](#).

2.4 Results

In chapter 1 previous studies of the FIRC were examined, these indicated that the correlation holds for a range of galaxy types over several decades of logarithmic luminosity. The results presented here are the q values that I have determined in terms of the \log_{10} ratios:

1. Far-infrared luminosity (FIR) to 1.4 GHz luminosity [$q_{\text{FIR}} 42.5 - 122.5 \mu\text{m}$]

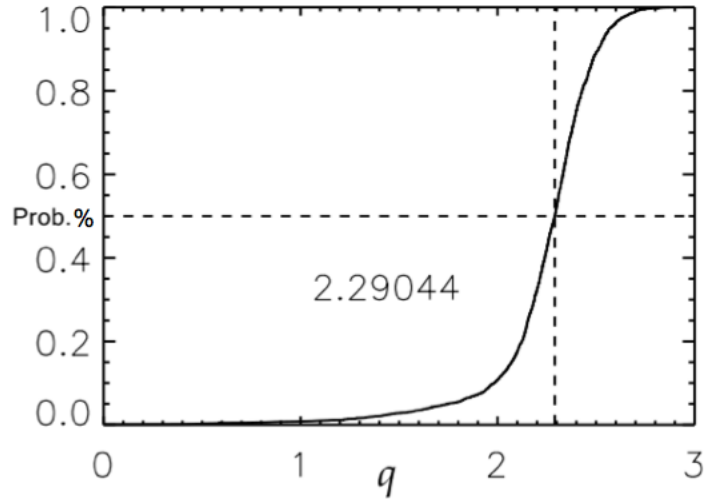


Figure 2.5: Typical probability distribution plot from the Kaplan Meier programme. The median value of q is defined where the horizontal dashed line (50% probability) intersects with the plotted curve.

2. Monochromatic 60 μm luminosity to 1.4 GHz luminosity [q_{60}]
3. Total IR luminosity (TIR) to 1.4 GHz luminosity [q_{TIR} 8 - 1000 μm]

In this chapter a sample of 11,330 galaxies is selected from the *IIFSCz* catalogue covering a contiguous area clear of the galactic plane as illustrated in Figure. 2.1. Of this sample only 7070 sources have a corresponding radio detection at 1.4 GHz, the remainder are assigned an upper limit flux of 2 mJy, this being just below the 5 sigma detection limit of approximately 2.5 mJy/beam.

Throughout this section I apply appropriate cuts where applicable to reduce selection effects which may impact on the determined q values. Star-forming galaxies (SFGs) hosting Active Galactic Nuclei (AGN) included in this sample will have boosted radio fluxes that will manifest as low q sources (Mushotzky, 2004). These possible AGN are eliminated from the calculated q sample by applying a cut at $q_{\text{FIR}} < 1.8$ as first implemented by Condon et al. (2002), see section 2.3.2. Completeness in the sample is an important consideration, 90% completeness limits for the 60 μm flux reported in the literature range from 0.2 Jy (Wang et al., 2008) and 0.26 Jy (Moshir et al., 1992) to 0.36 Jy (Wang & Rowan-Robinson, 2009). I apply a cut to galaxies in the sample with a 60 μm *IRAS* flux below a 0.25 Jy threshold. A cut in redshift beyond 0.5 is also made. The final sample size after applying these cuts is 5506.

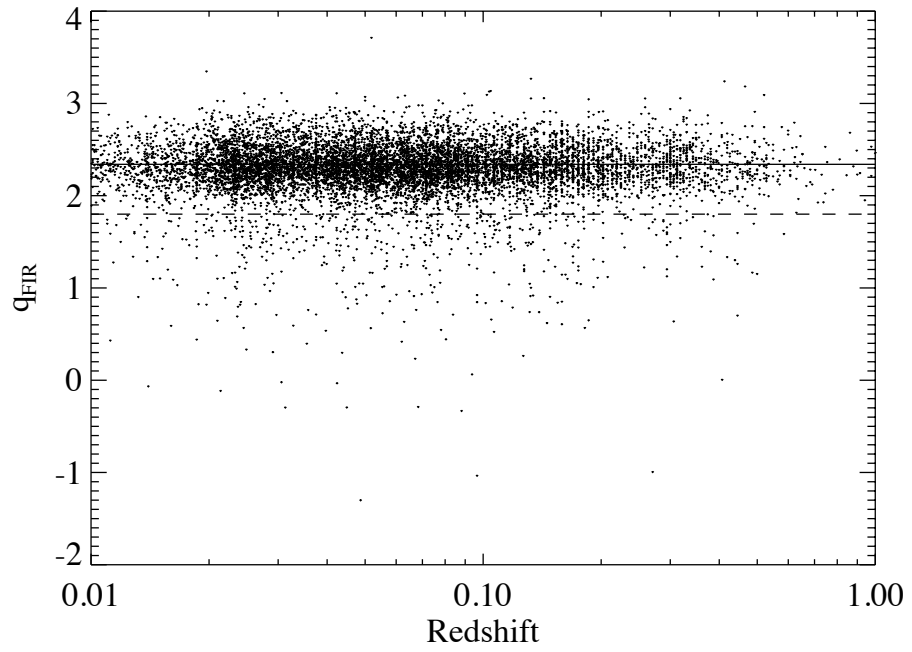


Figure 2.6: q_{FIR} calculated using Helou formula (Equation 2.4) plotted as a function of redshift. The broken line marks the cut used to discard possible AGN at $q_{\text{FIR}} < 1.8$ prior to finding the mean. The solid line indicates the mean value of $q=2.34 \pm 0.002$ with a dispersion σ_q of 0.21 for 10,591 objects out of 11181. k -correction is not used in the construction of this plot.

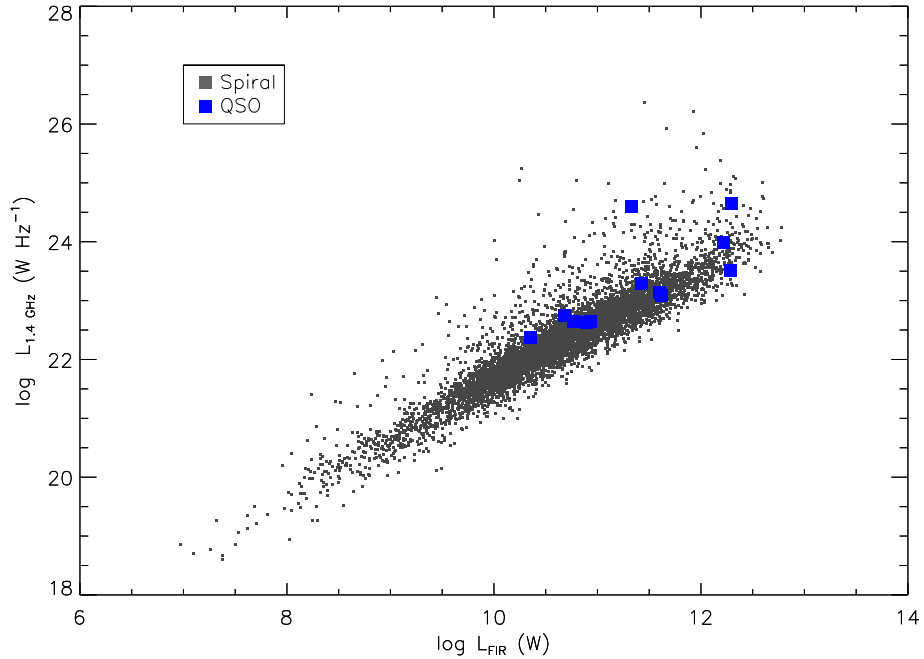


Figure 2.7: Far-infrared/radio correlation of a sample $> 11,000$ galaxies with no cuts applied. A small number of QSOs identified from their morphology are identified, with the majority of these falling on the correlation.

2.4.1 q_{FIR}

I calculate q_{FIR} following the method of Helou et al. (1985) with Equation 2.4 and find a mean of 2.34 ± 0.002 ($\sigma = 0.21$) for the data set of 10,591 objects selected from the primary sample after cuts are applied. Figure 2.6 illustrates q_{FIR} of this sample plotted as a function of redshift. Note that no k -correction was applied to the data when constructing this plot. This q agrees with a median $q_{\text{FIR}} \sim 2.3$ having a scatter of $\sigma_q \leq 0.2$ reported by Condon (1992) when similarly calculating q_{FIR} from *IRAS* flux densities at $60 \mu\text{m}$, $100 \mu\text{m}$ and radio flux at 1.4 GHz for a sample of spiral galaxies in Virgo. This q factor was calculated with observed frame fluxes which were adequate for the relatively low redshift Virgo cluster galaxies as determined by Helou et al. (1985). In the remainder of this section the sample is limited to a redshift of $z = 0.5$. Nevertheless these redshifts necessitate the use of rest-frame equivalents for both infrared and radio fluxes when calculating q . Infrared fluxes are corrected to rest-frame values with the prototype starburst ‘M82’ template. The radio fluxes are k -corrected with the spectral index set at $\alpha = -0.8$.

I compare the linearity in the FIRC as illustrated in Figure 1.5 (Condon, 1992), which plots $L_{1.4\text{GHz}}$ against L_{FIR} . That sample excluding AGN has a q of 2.32 ($\sigma = 0.20$). Figure 2.7 is my plot for the full sample of $L_{1.4\text{GHz}}$ against L_{FIR} , this plot includes all star

forming galaxies, including all radio loud objects, AGN, QSOs and ellipticals that are cut in subsequent calculations of the mean q .

QSO's in the sample shown in Figure 2.7 have been identified from optical galaxy template types in the *IIFSCz* catalog (Wang & Rowan-Robinson, 2009), (for details see Rowan-Robinson et al. (2008)) and will only be cut from further analysis if their q values fall below a predetermined limit. Therefore the sample is not restricted to starburst galaxies but will also have a presence of non-radio loud AGN.

The q_{FIR} of the full $0 < z < 0.5$ sample has a mean (standard deviation) 2.27 ± 0.004 ($\sigma = 0.32$). The sample now with radio loud objects eliminated has a mean q_{FIR} of 2.32 ± 0.003 ($\sigma = 0.21$) as illustrated in Figure 2.8. Any deviation from the correlation is difficult to distinguish from this plot therefore to explore possible evolution of the correlation the sample is split into redshift and luminosity slices. In terms of redshift the sample is cut into slices of width $0.05 z$ and in terms of luminosity slices are set at $0.5 \text{ Log } L_{60} \mu\text{m}$ intervals. The q_{FIR} were calculated for each redshift slice, see Table 2.2 and the associated plot Figures 2.9. There are deviations from the mean around $z \approx 0.4$ this may be due to incompleteness in the sample or errors in the photometric redshift, no definite trend is identified. Table 2.3 and the associated Figure 2.10 show q_{FIR} in terms of luminosity slices. There is a small rise from the mean q_{FIR} at low redshift when plotted against $\text{Log } L_{60}$ but settles to follow the mean to higher luminosities, again this deviation is not regarded as significant with respect to the errors. In table 2.4 I divide the q_{FIR} sample into blocks to illustrate the small changes in q within redshift / luminosity bins. Overall there is no definitive sign of evolution in either the redshift or luminosity slices.

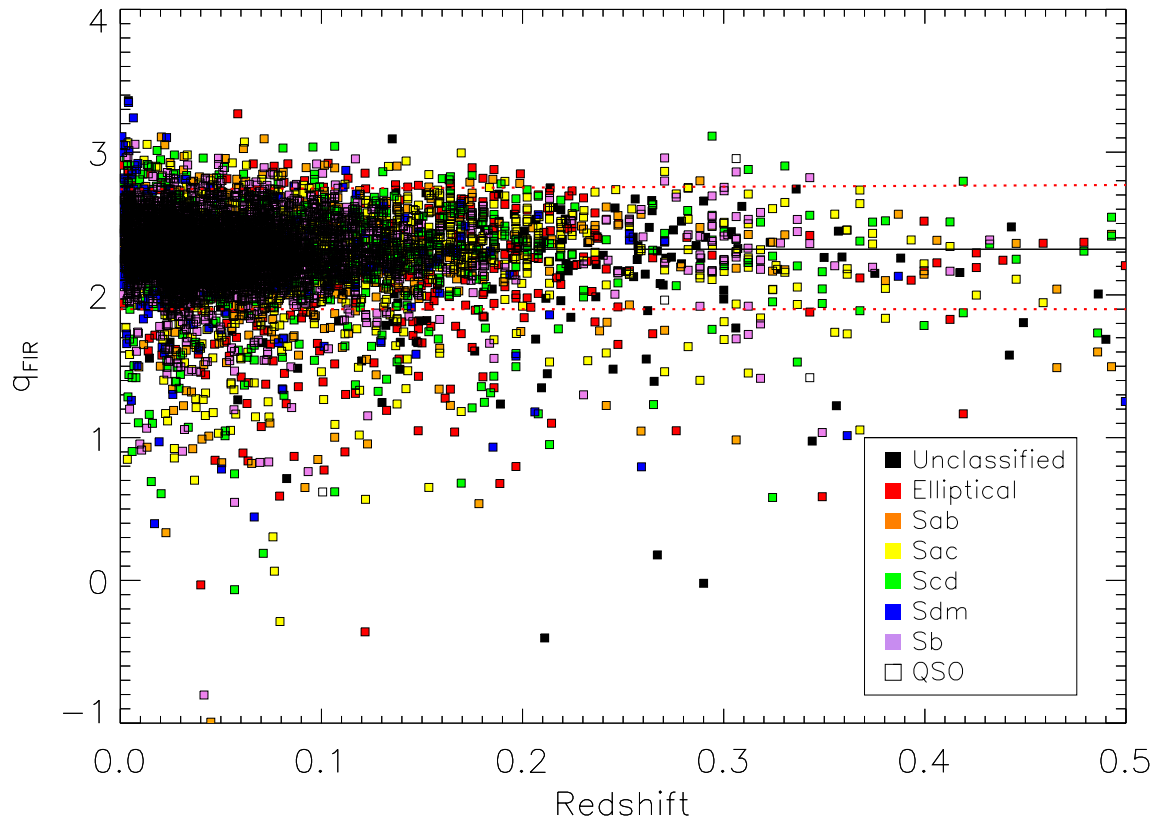


Figure 2.8: q_{FIR} plotted against redshift. The mean q_{FIR} value obtained for the whole sample is 2.27 ± 0.004 (σ 0.32). After possible AGN and radio loud sources are eliminated by cutting below $q_{\text{FIR}} = 1.8$ the final mean q_{IR} (solid line) is 2.32 ± 0.003 (σ 0.21). Dotted (red) lines are the 2σ limits.

Table 2.2: q_{FIR} redshift slices (non KM), see Figure 2.9

N_{Total}	$N_{\text{UpperLimits}}$	z range	q_{FIR}	σ
3885	927	$0.00 < z < 0.05$	2.32 ± 0.01	0.20
1788	346	$0.05 < z < 0.10$	2.31 ± 0.01	0.20
687	179	$0.10 < z < 0.15$	2.31 ± 0.01	0.22
321	89	$0.15 < z < 0.20$	2.35 ± 0.01	0.22
140	54	$0.20 < z < 0.25$	2.36 ± 0.01	0.20
77	29	$0.25 < z < 0.30$	2.38 ± 0.02	0.21
82	44	$0.30 < z < 0.35$	2.33 ± 0.03	0.27
36	23	$0.35 < z < 0.40$	2.22 ± 0.03	0.18
20	11	$0.40 < z < 0.45$	2.27 ± 0.06	0.28
23	16	$0.45 < z < 0.50$	2.36 ± 0.02	0.10

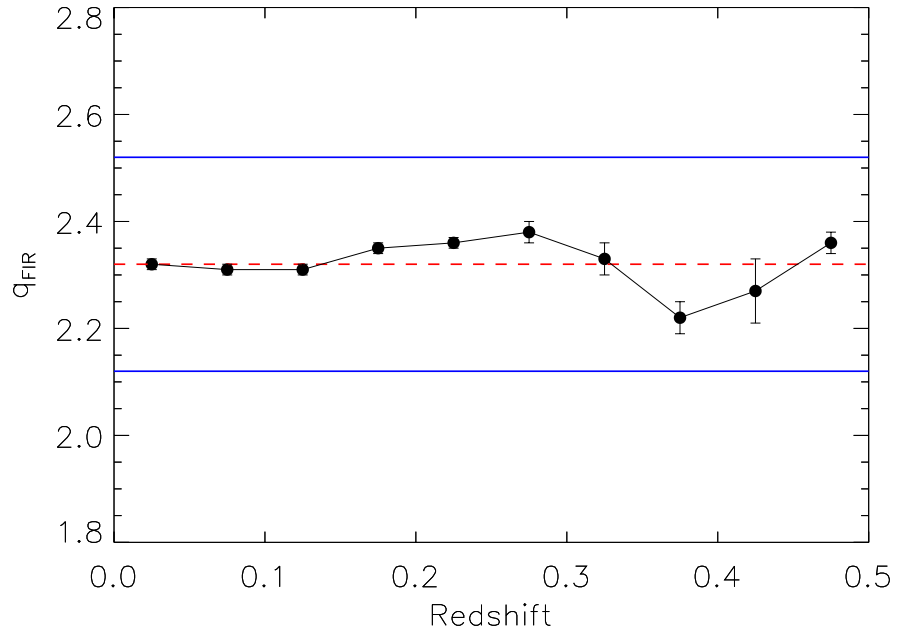


Figure 2.9: q_{FIR} (Equation 2.4 with rest-frame fluxes) versus redshift for a sample of 5351 objects plus 1276 with radio upper limits only. The dashed red line indicates the mean (KM) $q_{\text{FIR}} = 2.32 \pm 0.03$, the solid blue lines define $\pm 2\sigma_{q_{\text{FIR}}}$ ($\sigma_{q_{\text{FIR}}} = 0.20$).

Table 2.3: q_{FIR} luminosity slices (non KM), see Figure 2.10

N_{Total}	$N_{\text{UpperLimits}}$	Luminosity range	q_{FIR}	σ
229	100	$8.25, < L_{60} < 8.75$	2.42 ± 0.02	0.22
407	122	$8.75 < L_{60} < 9.25$	2.38 ± 0.02	0.23
1398	403	$9.25 < L_{60} < 9.75$	2.32 ± 0.01	0.18
1682	286	$9.75 < L_{60} < 10.25$	2.30 ± 0.01	0.19
1559	281	$10.25 < L_{60} < 10.75$	2.31 ± 0.01	0.20
969	208	$10.75 < L_{60} < 11.25$	2.30 ± 0.01	0.22
412	125	$11.25 < L_{60} < 11.75$	2.35 ± 0.01	0.22
159	74	$11.75 < L_{60} < 12.25$	2.32 ± 0.02	0.24
11	7	$12.25 < L_{60} < 12.75$	2.35 ± 0.10	0.20

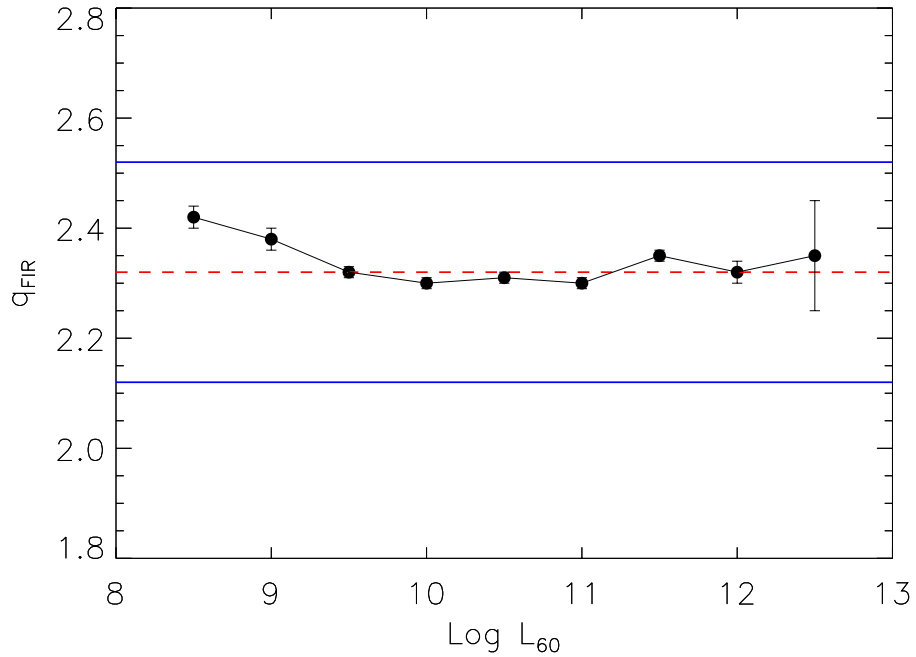


Figure 2.10: q_{FIR} (Equation 2.4 with rest-frame fluxes) versus $\log L_{60}$ luminosity for a sample of 5351 objects plus 1276 with radio upper limits only. The dashed red line indicates the mean (KM) $q_{\text{FIR}} = 2.32 \pm 0.03$, the solid blue lines define $\pm 2\sigma_{q_{\text{FIR}}}$ ($\sigma_{q_{\text{FIR}}} = 0.20$).

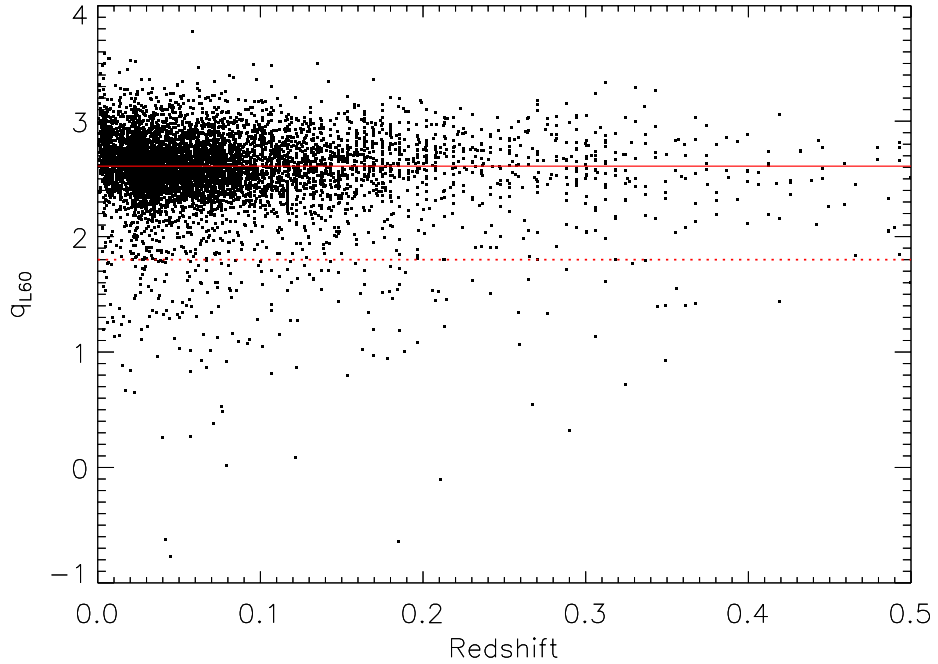


Figure 2.11: q_{L60} plotted against redshift. Radio loud sources are eliminated by cutting below $q_{L60}=1.8$. The mean q by Kaplan-Meier is 2.61 ± 0.01 , $\sigma = 0.24$.

2.4.2 q_{L60}

I test the linearity of the restframe q as a function of monochromatic $60 \mu\text{m}$ luminosity. Found less frequently in the literature than the Helou et al. (1985) formula, q in terms of luminosity is defined as

$$q_{L60} = \log_{10} \left(\frac{L_{60\mu\text{m}}}{L_{1.4\text{GHz}}} \right) \quad (2.14)$$

Infrared and radio luminosities are determined with IDL programme LofSZ (supplied by S. Oliver). This code incorporating k -correction, calculates log luminosity in solar units from a user supplied observed monochromatic flux density, redshift and appropriate rest-frame SED template. Here I have chosen to calculate the luminosities with an M82 template. This nearby (3.5×10^6 pc) starburst galaxy is commonly regarded as the prototype of this class of galaxy. As in the previous calculation a $60 \mu\text{m}$ flux cut of 0.25 Jy is applied to maximise completeness in the sample. Following the calculation of q_{L60} radio loud objects are similarly removed with a $q < 1.8$ cut. The mean value of q_{L60} is found to be 2.64 ± 0.01 with a dispersion of 0.24 . The plot of q_{L60} Figure 2.11 depicts the

distribution of galaxies classified as Spiral, Starburst and Elliptical identified from optical galaxy template types in the *IIFSCz* catalog (Wang & Rowan-Robinson, 2009). Objects of all three types are seen to follow the correlation although there is a population of radio loud spiral and elliptical galaxies that fall below $q = 1.8$ delimited by the broken line in the plot.

The histogram Figure 2.12 illustrates the distribution of q_{L60} across the whole sample. After applying a cut below $q_{L60} = 1.8$ to remove possible contamination from radio loud AGN and eliminating those with only radio upper limits the gaussian fitted to the remaining 6888 objects shows a good fit with a mean $q_{L60} = 2.63 \pm 0.01$ and dispersion of 0.21. There is an excess of objects found below $q_{L60} \approx 2.10$. This possibly indicates that the cut to remove radio loud objects is set too low.

As discussed in section 2.3.4 the Kaplan-Meier (KM) estimator can be used to provide an unbiased estimate of the mean of a sample by taking into account those members with only upper limits, in this application specifically radio upper limits. Applying the KM method to the calculation of the mean for the complete sample returns $q_{L60} = 2.60 \pm 0.003$ and dispersion of 0.33. The KM mean for the sample above the $q=1.8$ cut returns $q_{L60} = 2.61 \pm 0.004$ and dispersion of 0.24. A table of q_{L60} against redshift Tables 2.5 and the respective plot Figure 2.14 shows the k -corrected KM calculated means obtained for each redshift slice. Included in the table are numbers for both complete samples and those with only upper limits. In a similar but less pronounced deviation to that found in the q_{FIR} sample at $z \approx 0.4$ the q_{L60} also deviates from the mean but to a lesser extent, with the error bars indicating that the trend is to follow the mean. Similarly Table 2.6 and Figure 2.15 give the results for luminosity slices which are seen to follow the mean in a similar manor to that recorded for q_{FIR} , that is, no evolution is detected.

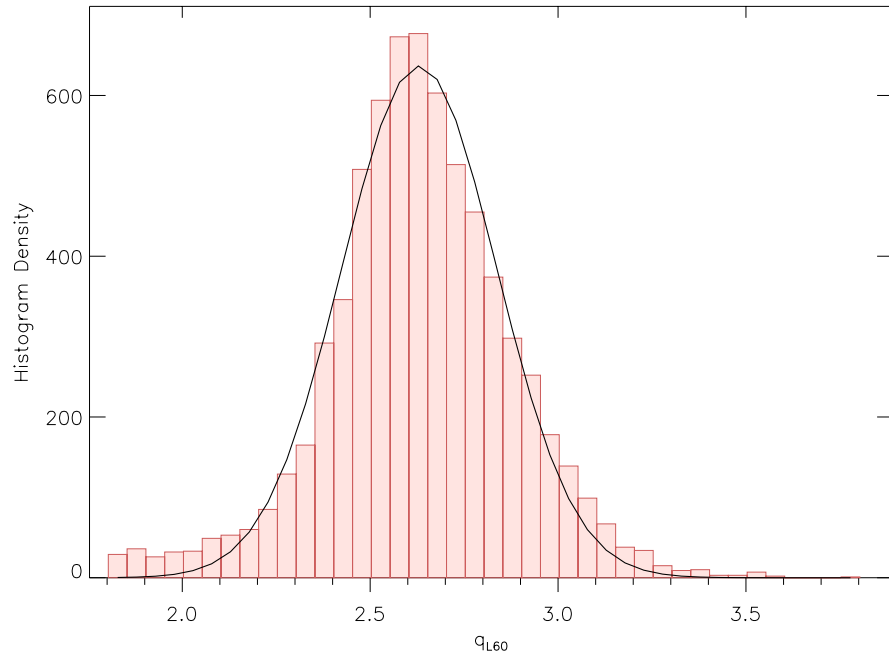


Figure 2.12: Histogram of q_{L60} of 6888 objects from an original sample of 11330 cut below $q_{L60} = 1.8$ to eliminate possible radio loud AGN (no radio upper limits). This plot illustrates the distribution of q for this sample over the redshift range $0 < z < 0.5$. The curve is a gaussian fit with a mean of $q_{L60} = 2.63 \pm 0.01$ and scatter 0.21.

Table 2.5: q_{L60} slices, see Figure 2.14

N_{Total}	$N_{\text{UpperLimits}}$	z range	q_{FIR}	σ
3952	927	$0.00 < z < 0.05$	2.64 ± 0.01	0.23
1820	346	$0.05 < z < 0.10$	2.66 ± 0.01	0.23
712	179	$0.10 < z < 0.15$	2.65 ± 0.01	0.25
332	89	$0.15 < z < 0.20$	2.69 ± 0.02	0.26
147	54	$0.20 < z < 0.25$	2.69 ± 0.03	0.27
82	29	$0.25 < z < 0.30$	2.69 ± 0.04	0.31
87	44	$0.30 < z < 0.35$	2.65 ± 0.05	0.34
37	23	$0.35 < z < 0.40$	2.58 ± 0.07	0.26
21	11	$0.40 < z < 0.45$	2.61 ± 0.09	0.29
23	16	$0.45 < z < 0.50$	2.66 ± 0.04	0.10

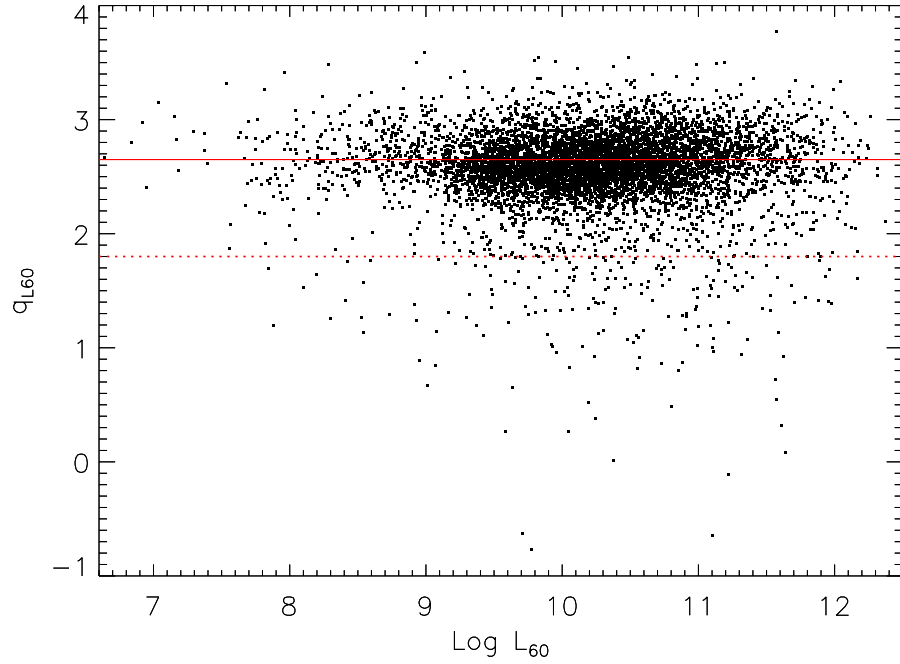


Figure 2.13: q_{L60} plotted against L_{60} . The mean q_{L60} value obtained for the whole sample is 2.60 ± 0.01 where Kaplan Meier Statistics are employed to include upper limits. When possible AGN and radio loud sources are eliminated by cutting below $q_{L60} = 1.8$ (lower dashed line) the mean q_{L60} is 2.65 ± 0.01 (solid line) and dispersion of 0.24.

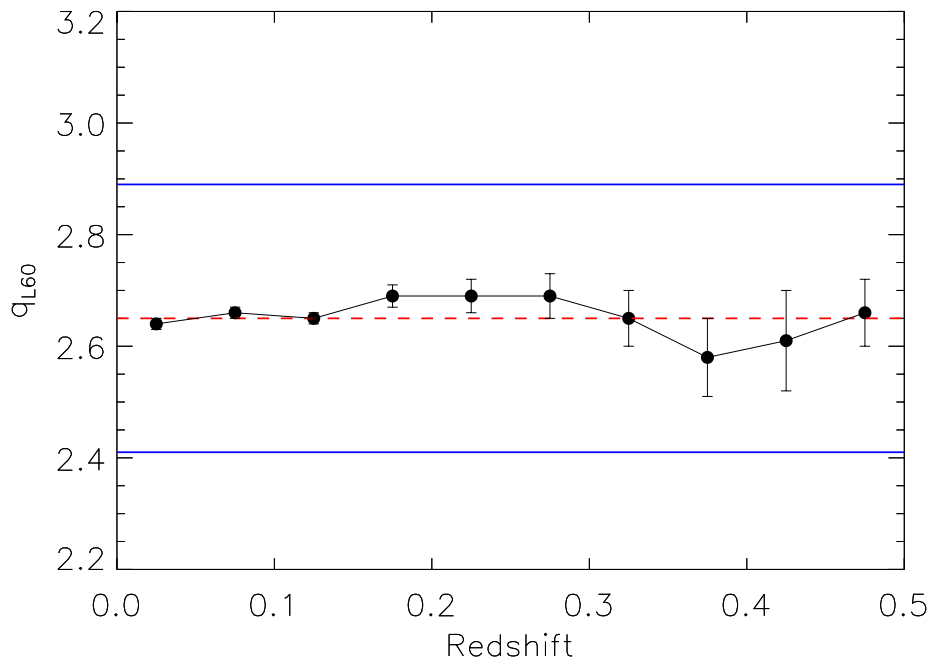


Figure 2.14: q_{L60} (calculated and k-corrected with LofSZ) versus redshift for a sample of 5506 objects plus 1726 with radio upper limits only. The dashed red line indicates the mean (KM) $q_{L60} = 2.65 \pm 0.01$, the solid blue lines define $\pm 2\sigma_{q_{L60}}$ ($\sigma_{q_{L60}} = 0.24$).

Table 2.6: q_{L60} luminosity slices, see figure 2.15

N_{Total}	$N_{\text{UpperLimits}}$	Luminosity range	q_{FIR}	σ
86	53	$8.25 < L_{60} < 8.75$	2.70 ± 0.05	0.31
191	104	$8.75 < L_{60} < 9.25$	2.68 ± 0.03	0.25
292	92	$9.25 < L_{60} < 9.75$	2.71 ± 0.02	0.25
870	302	$9.75 < L_{60} < 10.25$	2.63 ± 0.01	0.22
1647	325	$10.25 < L_{60} < 10.75$	2.61 ± 0.01	0.23
1787	286	$10.75 < L_{60} < 11.25$	2.63 ± 0.01	0.22
1298	244	$11.25 < L_{60} < 11.75$	2.66 ± 0.01	0.24
679	162	$11.75 < L_{60} < 12.25$	2.68 ± 0.01	0.26
287	106	$12.25 < L_{60} < 12.75$	2.68 ± 0.02	0.31
64	33	$12.75 < L_{60} < 13.25$	2.65 ± 0.05	0.28

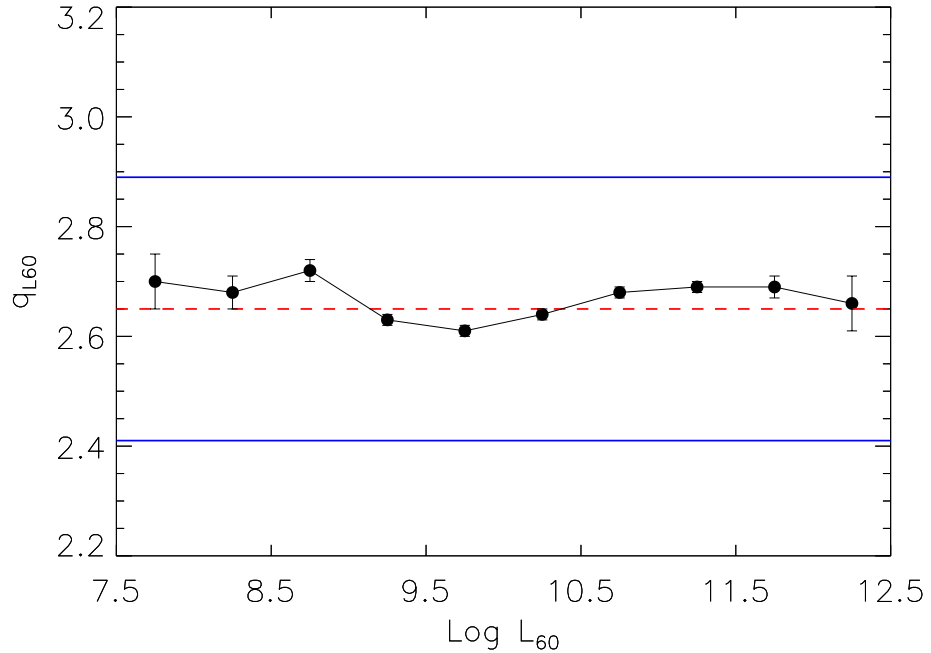


Figure 2.15: q_{L60} (calculated and k-corrected with LofSZ) versus $\log L_{60}$ luminosity for a sample of 5506 objects plus 1726 with radio upper limits only. The dashed red line indicates the mean (KM) $q_{L60} = 2.65 \pm 0.01$, the solid blue lines define $\pm 2\sigma_{q_{L60}}$ ($\sigma_{q_{L60}} = 0.24$).

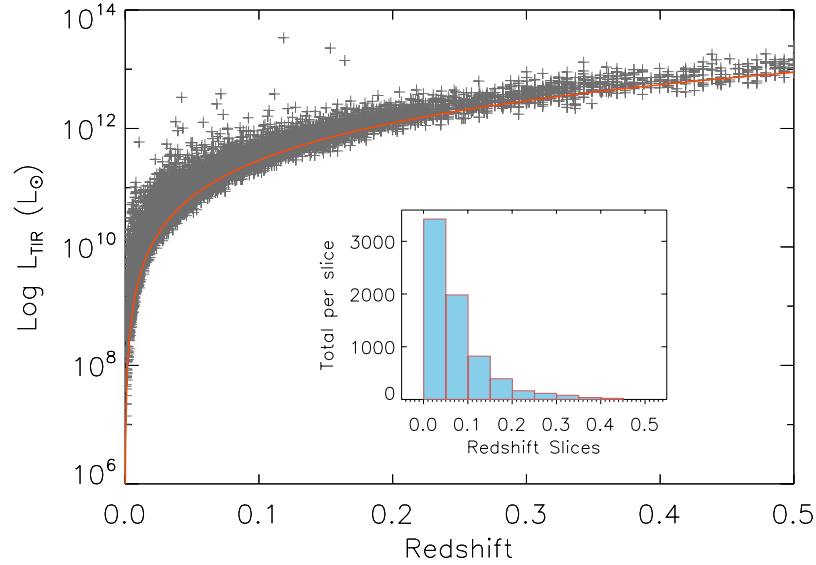


Figure 2.16: L_{TIR} vs redshift. The red line is the completeness cut applied at the $60 \mu\text{m}$, 0.25 Jy flux limit. The inset shows the number of objects in each redshift slice

2.4.3 q_{TIR}

A more commonly expressed version of the q -parameter is

$$q_{\text{TIR}} = \log_{10} \left(\frac{\text{TIR}}{3.75 \times 10^{12} \text{ W m}^{-2}} \right) - \log_{10} \left(\frac{S_{1.4 \text{ GHz}}}{\text{W m}^{-2} \text{ Hz}^{-1}} \right) \quad (2.15)$$

this is a modified version of the [Helou, Soifer & Rowan-Robinson](#) formula where the FIR luminosity is replaced with the L_{TIR} the total IR luminosity derived from the integrated flux between 8 and $1000 \mu\text{m}$. To derive the total luminosity I use the IDL fitting procedure by [Casey \(2012\)](#). *IRAS* 12 , 25 , 60 and $100 \mu\text{m}$ fluxes are fitted to a modified single dust temperature grey-body which represents starburst emission, hot starburst regions with AGN activity are represented by a mid-infrared power law. The radio luminosity data is k -corrected to the rest-frame with

$$L_{1.4 \text{ GHz}} = \frac{4\pi D_L^2}{(1+z)^{1+\alpha}} S_{1.4 \text{ GHz}} \quad (2.16)$$

and the q in terms of total infrared and radio luminosity is then given by

$$q_{\text{TIR}} = \log_{10} \left(\frac{L_{\text{TIR}}[L_{\odot}]}{L_{\text{radio}}[L_{\odot}]} \right) \quad (2.17)$$

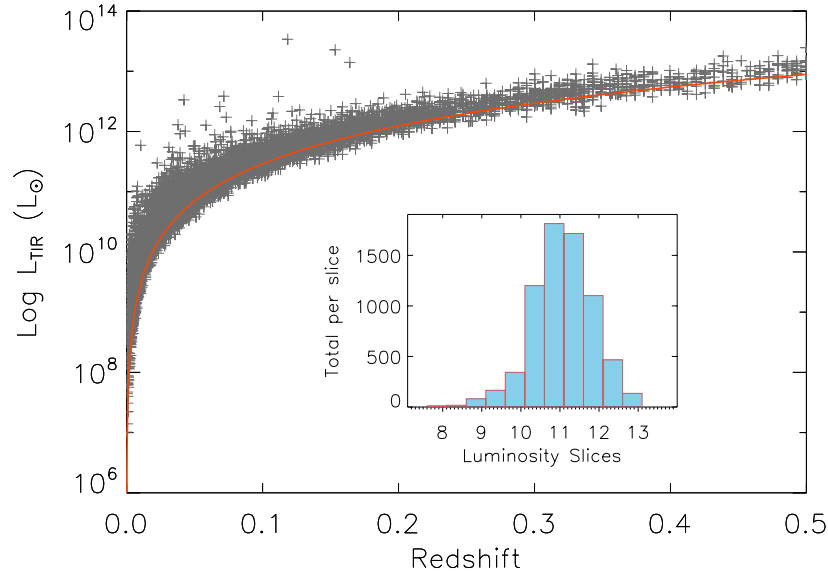


Figure 2.17: L_{TIR} vs redshift. The red line is the completeness cut applied at the $60 \mu\text{m}$, 0.25 Jy flux limit. The inset shows the number of objects in each luminosity slice.

I have applied a completeness cut to the full sample corresponding to the $60 \mu\text{m}$ 0.25 Jy flux limit and employed Kaplan-Meier survival analysis to take into account upper limits in the remaining objects in the radio sample previously eliminated from the analysis and find the mean q_{TIR} to be 2.72 ± 0.01 ($\sigma = 0.24$) after applying a cut at $q = 1.8$ to discard radio loud objects. Proportionally raising this cut from the value introduced by [Condon et al. \(2002\)](#) to $q = 2.2$ increases the mean q_{TIR} by 1% to 2.75.

In the same manner as the q_{FIR} and q_{L60} were treated I split the q_{TIR} into redshift and luminosity slices. Table 2.7 and Figure 2.18 for redshift slices indicate a deviation from the mean at redshifts > 0.3 , error bars at this redshift are large and do not support a true deviation from the mean. Table 2.8 and Figure 2.19 for luminosity slices show that the mean q s for these slices are very close to the mean of the whole sample.

When I plot the FIRC with galaxies selected according to the classification in the *IIFSCz* catalogue, which uses optical galaxy templates to divide the sample into a number of categories ([Rowan-Robinson et al., 2008](#)), I find that a number of objects classified as ellipticals fall on or near the mean q for spiral galaxies. These are not mainstream ellipticals but a small fraction of ellipticals exhibiting signs of active star formation as defined by their far-infrared and radio fluxes. A small sample of actively star forming field ellipticals has been identified by [Fukugita et al. \(2004\)](#), these have ongoing star formation rates comparable to those found in spiral galaxies.

Similarly for QSOs I find that there is a population that falls on the mean q of spiral

galaxies. It has been shown that these QSOs may have FIR emission as a result of direct heating by AGN or by ongoing star-formation ([Schweitzer et al., 2006](#)).

In table 2.9 are the (KM) mean q values for the whole sample classified from optical galaxy templates into seven groups: ellipticals, spirals (subdivided into Hubble types) and QSOs. No cuts are applied hence the qs are lower than mean previously reported. There is little variation found in the mean values, only QSOs have a distinctly low q .

Table 2.7: q_{LTIR} redshift slices (KM Stats), see figure 2.18

N_{Total}	$N_{\text{UpperLimits}}$	z range	q_{FIR}	σ
3976	927	$0.00 < z < 0.05$	2.71 ± 0.01	0.24
1835	349	$0.05 < z < 0.10$	2.72 ± 0.01	0.23
716	180	$0.10 < z < 0.15$	2.70 ± 0.01	0.26
338	90	$0.15 < z < 0.20$	2.73 ± 0.02	0.27
151	56	$0.20 < z < 0.25$	2.68 ± 0.03	0.26
81	29	$0.25 < z < 0.30$	2.73 ± 0.03	0.25
88	44	$0.30 < z < 0.35$	2.64 ± 0.04	0.29
38	24	$0.35 < z < 0.40$	2.62 ± 0.06	0.21
21	11	$0.40 < z < 0.45$	2.64 ± 0.08	0.24
24	17	$0.45 < z < 0.50$	2.80 ± 0.05	0.12

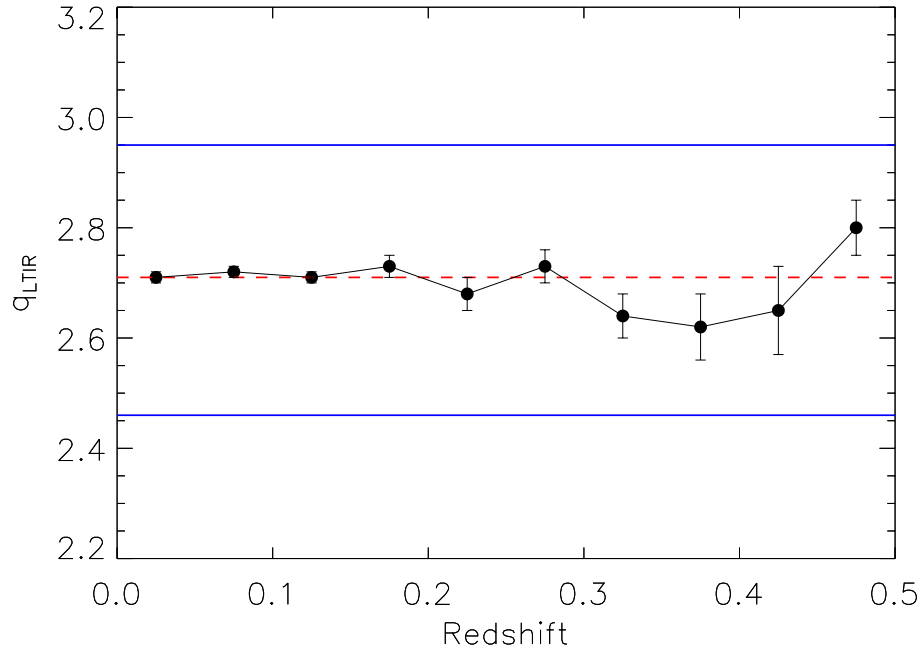


Figure 2.18: q_{TIR} (total IR luminosity and k-corrected radio) versus redshift for a sample of 5552 objects plus 1705 with radio upper limits only. The dashed red line indicates the mean (KM) $q_{\text{TIR}} = 2.72 \pm 0.03$, the solid blue lines define $\pm 2\sigma_{q_{\text{TIR}}}$ ($\sigma_{q_{\text{TIR}}} = 0.24$).

Table 2.8: q_{LTIR} luminosity slices (KM Stats), see figure 2.19

N_{Total}	$N_{\text{UpperLimits}}$	z range	q_{FIR}	σ
192	104	$8.0 < L_{60} < 8.5$	2.73 ± 0.03	0.32
291	92	$8.5 < L_{60} < 9.0$	2.76 ± 0.02	0.29
871	301	$9.0 < L_{60} < 9.5$	2.73 ± 0.01	0.26
1651	324	$9.5 < L_{60} < 10.0$	2.71 ± 0.01	0.24
1791	286	$10.0 < L_{60} < 10.5$	2.70 ± 0.01	0.25
1299	244	$10.5 < L_{60} < 11.0$	2.73 ± 0.01	0.25
687	162	$11.0 < L_{60} < 11.5$	2.70 ± 0.01	0.30
287	106	$11.5 < L_{60} < 12.0$	2.67 ± 0.02	0.30
64	33	$12.0 < L_{60} < 12.5$	2.66 ± 0.05	0.28

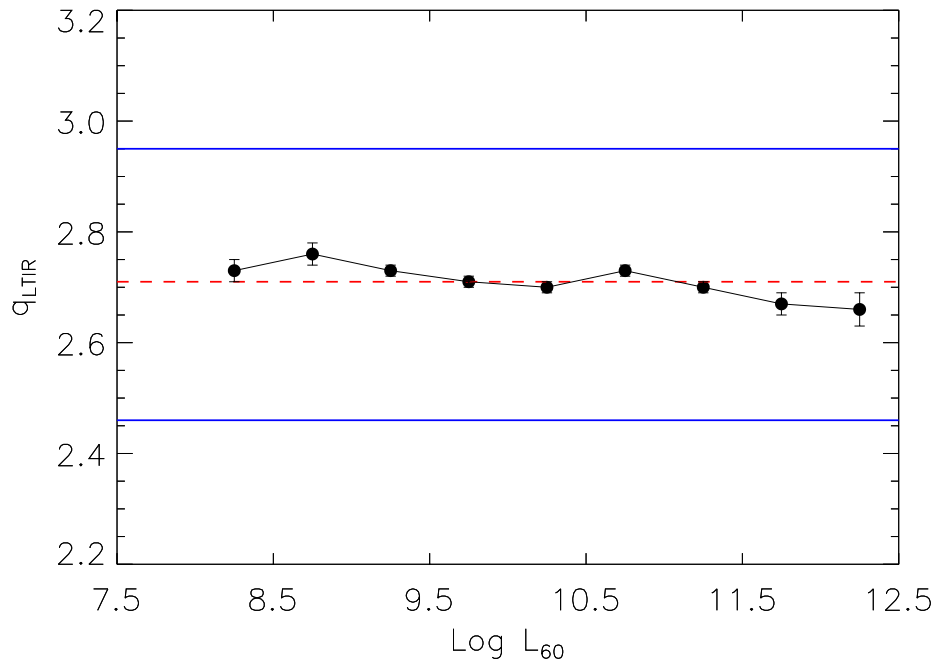


Figure 2.19: q_{TIR} (total IR luminosity and k-corrected radio) versus $\log L_{60}$ luminosity for a sample of 5552 objects plus 1705 with radio upper limits only. The dashed red line indicates the mean (KM) $q_{\text{TIR}} = 2.72 \pm 0.03$, the solid blue lines define $\pm 2\sigma_{q_{\text{TIR}}}$ ($\sigma_{q_{\text{TIR}}} = 0.24$).

Table 2.9: Variation in q_{L60} with galaxy types from optical templates

Galaxy Type	N_{Total}	$N_{\text{UpperLimits}}$	q_{L60}	σ
Elliptical	1700	704	2.60 ± 0.01	0.25
Sab	1762	491	2.61 ± 0.01	0.24
Sbc	2300	787	2.61 ± 0.01	0.24
Scd	1821	772	2.61 ± 0.01	0.25
Sdm	1195	549	2.60 ± 0.01	0.24
sb	1954	715	2.59 ± 0.01	0.24
QSO	14	2	2.49 ± 0.06	0.19

2.5 Discussion

The FIRC is examined for a sample of 11,330 galaxies selected from the *IIFSCz* catalogue, all complete with *IRAS* 12, 25, 60 and 100 μm fluxes. Of this sample 7,071 are also complete with 1.4 GHz radio flux densities, primarily composed of *NVSS* sources listed in the *IIFSCz* catalogue, additionally supplemented at redshifts $z > 0.2$ with sources from the VLA *FIRST* radio catalogue. The FIRC determined using the original method of Helou et al. was found to have a mean $q_{\text{FIR}} = 2.34 \pm 0.01$ with a scatter of 0.21 which is higher than $q_{\text{FIR}} = 2.14$ found by Helou et al., however the q of my sample matches $q = 2.34 \pm 0.01$ found by Yun et al. (2001) with a sample of 1809 *IRAS* detected galaxies. This new q_{FIR} value holds over a significantly larger sample than that of 38 galaxies in the original paper by Helou et al. (1985). Plots of redshift (Figure 2.9) and luminosity (Figure 2.9) cuts for this sample do not show any evidence for evolution in either regime.

The monochromatic q_{L60} was evaluated in terms of luminosity via Formula 2.14. Observed fluxes were corrected to the rest-frame using M82 templates in both the infrared and radio wavelengths and was found to have a mean value of 2.65 ± 0.01 ($\sigma = 0.24$) Redshift (Figure 2.14) and luminosity (Figure 2.15) cuts for this sample again do not show any evidence for evolution in either regime and are similar in form to the results seen in q_{FIR} .

The q_{TIR} of this sample was calculated with the aid of the IDL SED fitting program by Casey (2012). This is a more robust method than the alternative Formula 2.5. Again no evidence is presented for evolution in either the redshift or luminosity selected samples shown in Figures 2.18 and 2.19. The mean q_{TIR} is found to be 2.72 ± 0.01 ($\sigma=0.24$) following a cut below $q_{\text{TIR}} = 1.8$. This mean value taking upper radio limits into account by the application of Kaplan Meier statistics is higher than found by Bell (2003) with a median q_{TIR} of 2.64 and a scatter of 0.26 dex, and that reported by Sargent et al. (2010b), with $2.52 < q_{\text{TIR}} < 2.63$ for sources at $z \leq 0.5$ with a dispersion $\sigma_{q_{\text{TIR}}} \approx 0.35$.

In this chapter I have confirmed that the Far-Infrared - Radio Correlation of a large sample sample of galaxies remains reasonably constant to $z \sim 0.5$ which agrees with findings of Sargent et al. (2010a), Jarvis et al. (2010), Ivison et al. (2010), Bourne et al. (2011) and Mao et al. (2011), the only exception being Seymour et al. (2009) who reports a gradual decline in the q ratio with increasing redshift.

Chapter 3

The FIRC as a function of temperature

In the previous chapter I examined the FIRC for a large number of star forming galaxies and demonstrated that in terms of the mean ‘ q ’ value there was no definitive sign of evolution in terms of redshift or luminosity. In this chapter an alternative approach is taken in the investigation of the FIRC, by looking for changes that correlate with temperature in the star forming population.

3.1 The q of warm and cold galaxies

The far-infrared radiation can be modelled as a combination of three components. The first is a ‘cool’ component radiating from the disc where the diffuse dust is heated by the interstellar radiation. This component is well matched to the optical luminosity. Secondly, a warm ‘starburst’ component where dust is locally heated in HII regions by star formation. Finally, a ‘Seyfert’ component which is attributed to a compact continuum source hidden within a central dust cloud (Rowan-Robinson & Crawford, 1989).

In a study of the cool ‘cirrus’ component Xu et al. (1994) use $H\alpha$ data to separate out the warm component. The cool component was determined from the difference of this warm component and the total FIR. Their results show a tight linear correlation of the cool-FIR to radio continuum at 20 cm, and a less tight correlation of the warm-FIR to radio ratio. From these results Xu et al. propose that the tight cool correlation with the non-thermal radio component is due to stars of intermediate mass (5 - 20 M_{\odot}), whereas a correlation of the warm-FIR to thermal-radio continuum is attributed to massive stars $\geq 20 M_{\odot}$.

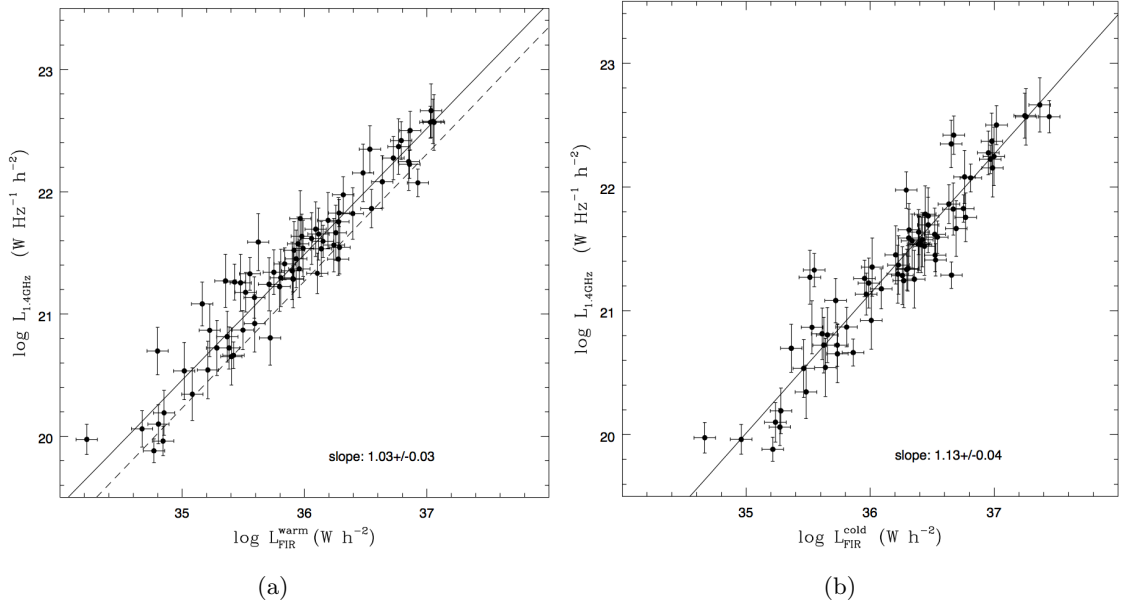


Figure 3.1: (a) The radio luminosity at 1.4 GHz vs. the total FIR luminosity of the warm component for a sample of 72 object. (b) The radio luminosity at 1.4 GHz vs. the total FIR luminosity of the cold component for a sample of 72 objects. Reproduced from [Pierini et al. \(2003\)](#).

The warm and cold FIRC has also been investigated by [Pierini et al. \(2003\)](#) with a limited sample of 72 galaxies complete with *IRAS* 60 and 100 μm fluxes supplemented with ISO-ISOPHOT 170 μm fluxes, extending the spectral coverage into the cooler dust beyond the spectral coverage of *IRAS*. [Pierini et al.](#) calculated separate luminosities for the warm and cool components and plotted these against the radio luminosity at 1.4 GHz finding that the slope of the warm FIRC was linear (Figure 3.1a) and that the slope of the cold FIRC (Figure 3.1b) was slightly non linear. A larger sample of 725 objects is now used to further investigate the properties of temperature selected samples and examine any differences in q .

3.1.1 Dust Temperatures

I now extend my investigation into the possible variation of q with galaxy dust temperatures. [Garn \(2008\)](#) gives an approximation for maximum dust temperature from the maximum infrared flux using Wien's displacement law for a black body spectrum.

$$\left(\frac{\lambda_{max}}{\mu\text{m}}\right) \simeq 2906 \left(\frac{T}{\text{K}}\right)^{-1} \quad (3.1)$$

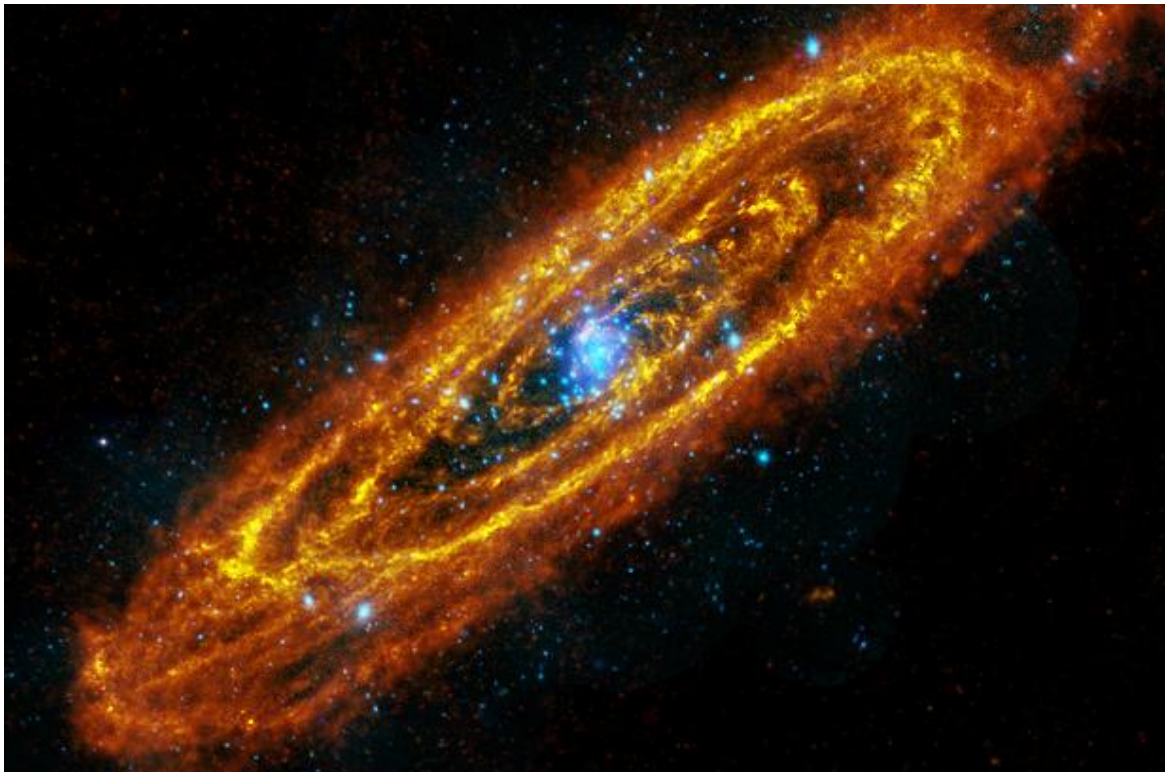


Figure 3.2: Herschel's far-infrared view of the Andromeda galaxy, M31 imaged at $250\ \mu\text{m}$ illustrating the emission from the dusty spiral arms. The blue regions are X-ray sources - mainly supernova remnants. Image credits: ESA/Herschel/PACS/SPIRE/J Fritz, U Gent; X-ray: ESA/XMM-Newton/EPIC/W Pietsch, MPE.

By this approximation it is seen that if the far-infrared spectrum peaks around $100 \mu\text{m}$ then the peak dust temperature will be $\approx 30\text{K}$. There are other methods of approximating the peak temperature, one commonly used is the *IRAS* $60 \mu\text{m}/100 \mu\text{m}$ colour ratio, which has been used as a proxy for dust temperature (Langer et al. (1989), Helou et al. (1991), Schnee, Ridge, Goodman & Li (2005)), where ‘cold’ galaxies are indicated by a low $60 \mu\text{m}/100 \mu\text{m}$ colour ratio and ‘warm’ galaxies are indicated by a high colour ratio. Parker (1991) gives a more formal formulation where the dust temperature is given by

$$T_d = \frac{\frac{hc}{k} \left(\frac{1}{\lambda_2} - \frac{1}{\lambda_1} \right)}{(3 + \beta) \log_e \left(\frac{\lambda_1}{\lambda_2} \right) \log_e \left(\frac{S\lambda_1}{S\lambda_2} \right)} \quad (3.2)$$

where λ_1 and λ_2 are flux densities at two *IRAS* wavelengths and the dust grain emissivity represented by β , typically taken to be in the range $0 \leq \beta \leq 2$ although generally accepted as uncertain. Bianchi, Davies & Alton (1999) report a more realistic value for this variable to be closer to $1 \leq \beta \leq 2$.

IRAS was only able to sample the Wien (short wavelength) side of galaxy spectral energy distributions (SED). In pursuit of an accurate dust peak temperature it would be ideal to have comparable samples on the Rayleigh-Jeans (long wavelength) side of the SED. Since the launch of *IRAS* in 1983 there have been several notable space telescopes dedicated to infrared wavelengths. The first of these launched in 1995 was *ISO*, the *European Space Agency (ESA) Infrared Space Observatory* carrying ISOPHOT an imaging photo-polarimeter that observed over the range of 110 to $240 \mu\text{m}$. One survey in particular with this instrument at $170 \mu\text{m}$ would have been useful for this research if it had comprised of more than the recorded 1927 galaxies with optical counterparts (Stickel et al., 2004). 2003 saw the launch of the *SPITZER* Space Telescope with the capability to do $160 \mu\text{m}$ photometry but scans were limited to small fields, for example see the SWIRE ELAIS N1 Source Catalog (Surace et al., 2004). The *Akari Infrared Astronomy Satellite*, launched in 2006 completed an all-sky survey in 18 months (see Yamamura et al. (2010) for the All-Sky Bright Source Catalogue). Of particular interest for this thesis is the *Akari* $140 \mu\text{m}$ data, see next section for details. The most recent mission of interest was the *Herschel space Observatory*, launched in 2009. This was an *ESA* mission covering the longer wavelengths of 250 , 350 and $500 \mu\text{m}$ with the SPIRE the Spectral and Photometric Imaging Receiver. Figure 3.2 illustrates the heating of cool dust in the spiral arms of M31 as seen by *Herschel* at $250 \mu\text{m}$. The primary survey, *HerMES*, the *Herschel* Multi-tiered Extragalactic Survey

(Oliver et al., 2012) was a set of targeted observations directed at a number of specific deep fields. Herschel did not undertake a full sky survey.

An investigation into the possible variation in q for subsamples of warm and cold *IRAS* galaxies reveals no clear cut boundary between cool and warm galaxies. For instance Saunders et al. (1990) divide their sample into cold ($T_{emitted} < 36$ K) disc dominated and warm ($T_{emitted} \geq 36$ K) starburst/Seyfert. When dividing this sample the models of Rowan-Robinson & Crawford (1989) were used. A second example of temperature division is by using *IRAS* colours. This method was selected by Hawkins et al. (2001) who divide their catalogue into three subsamples using the 60 and 100 μm fluxes. Colour ratios define the boundary selection, where hot galaxies are defined with $f_{100}/f_{60} < 1.7$, warm galaxies with $1.7 < f_{100}/f_{60} < 2.3$ and cold galaxies with $f_{100}/f_{60} > 2.3$. These boundaries correspond to temperatures of 31 and 28 K (Equation 3.2).

The longest wavelength observed by *IRAS* was 100 μm , thus *IRAS* data does not necessarily resolve the peak of the spectral energy distributions (SEDs) of all the individual galaxies in our sample. Typical star-forming galaxies in the *IRAS* survey are expected to have SEDs peaking at wavelengths between 60 and 100 μm , whereas galaxies closer in type to our own Milky Way will typically peak closer to 200 μm (Blain et al., 2002). To calculate realistic peak dust temperatures we require access to longer infrared wavelengths. I now look to data from the *AKARI* infrared astronomy satellite operated by the *Japan Aerospace Exploration Agency*. The *AKARI* All-Sky Survey Point Source Catalogue provides data at wavelengths of 65, 90, 140 and 160 μm (Yamamura et al., 2010). I am particularly interested in extending the wavelength coverage around the peak of the Spectral Energy Distribution (SED). The 140 μm data fits this role and is used to supplement the *IRAS* 60 and 100 μm fluxes. Note that Yamamura et al. (2010) indicate in their catalogue that only data flagged as $FQUAL=3$ is to be used for scientific purposes.

I adopt a single temperature modified grey-body fit to the infra-red data, choosing the dust emissivity index β to be the same for each object. For a discussion on β selection see Dunne & Eales (2001). To find the dust temperatures for each galaxy I now fit *IRAS* (60 and 100 μm) and *AKARI* (140 μm) flux densities using the IDL code of Casey (2012). By utilising a minimum input of three data points (and up to 10) with associated errors plus redshifts this program fits the supplied flux densities to a single dust temperature grey-body of the form

$$S(\lambda) = N_{\text{bb}} \frac{(1 - e^{-(\lambda_0/\lambda)^\beta}) (\frac{c}{\lambda})^3}{e^{hc/\lambda kT} - 1} + N_{\text{pl}} \lambda^\alpha e^{-(\lambda/\lambda_c)^2} \quad (3.3)$$

with free parameters: N_{bb} the greybody normalisation, T the greybody temperature, β the emissivity index and α the MIR power-law slope. N_{pl} is the normalisation of the power-law term and λ_c is the power-law turnover wavelength. N_{pl} determines the flux scaling of the power-law term relative to the grey-body. N_{pl} and λ_c are tied to the best fitting values of N_{bb} , T and α . In the fitting procedure a single dust temperature grey-body is added to a mid-infrared power-law which is approximated in the IDL program of Casey. The value of β is dependent on the dust grain properties such as size, compactness and composition, while the dust in galaxies is taken to be $1 < \beta < 2$ (Schnee, 2006), noting that for a pure blackbody $\beta=0$. The dust emissivity index β , is fixed at 1.5 as tested in Casey (2012), where it was found that using $\beta=2$ only gave a small difference of < 2 K in the dust temperature obtained from the fit.

Here I am not concerned with the absolute temperature as I am using temperature to divide the sample into nominal ‘cold’ and ‘warm’ temperature bins so that a comparison of q_{cold} and q_{warm} can be made. The program of Casey also calculates the total infra-red luminosity from 8 to 1000 μm (L_{TIR}) of each source which enables the calculation of q_{TIR} . The IDL programme takes inputs of redshift, wavelength, flux densities and uncertainty on flux densities for a minimum of three photometric data points per galaxy. I select the output to be restricted to two free parameters L_{TIR} and T_{dust} , where L_{TIR} is output in log solar luminosities and T_{dust} in K.

Some objects are found to have large temperature errors that are probably due to under recording the true flux by *IRAS* or over recording by *AKARI*, leading to a diverging data set which no longer represents the true flux across the measured (60 μm , 100 μm , 140 μm) wavebands, and is impossible to fit to an SED. These sources are therefore eliminated from the sample. Now I am able to calculate q_{TIR} for the whole sample using the rest-frame total infrared luminosity and the rest-frame 1.4 GHz radio luminosity where

$$q_{\text{TIR}} = \log_{10} \left(\frac{L_{\text{TIR}}}{L_{1.4\text{GHz}}} \right) \quad (3.4)$$

A small population of the sample with low q are possibly AGN, in Chapter two I show that these were identified as sources having $q < 1.8$ as defined by Condon et al. (2002). This was for q_{FIR} where FIR refers to the wavelengths between 42.5 and 122.5 μm . I am calculating q_{TIR} where TIR is defined as the wavelengths between 8 and 1000 μm .

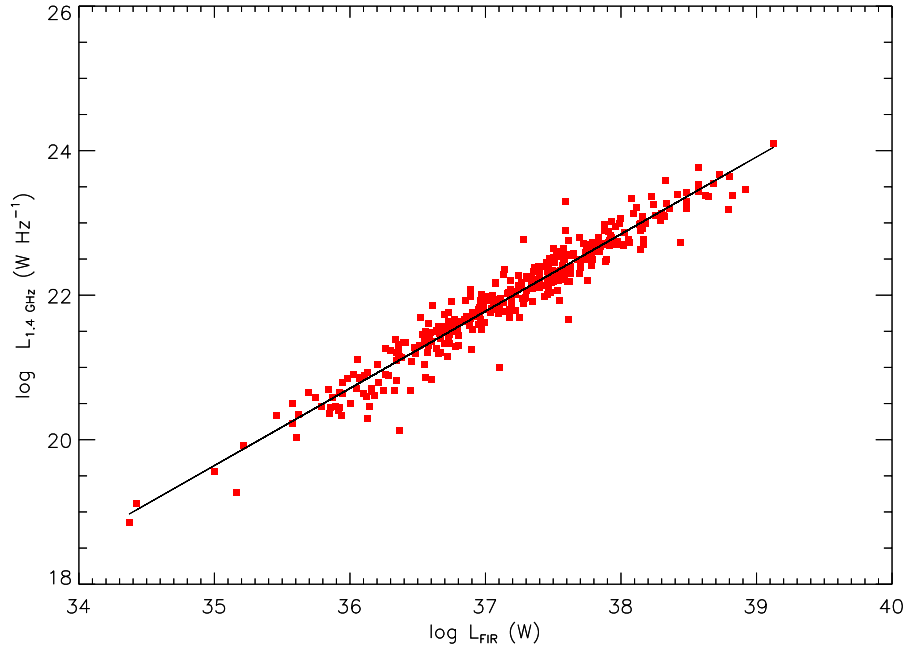


Figure 3.3: The radio luminosity at 1.4 GHz vs. the total FIR luminosity for a sample of 369 warm objects selected with a temperature above 24 K. The slope of the correlation is 1.06 ± 0.03 .

3.2 Results

Following an earlier investigations of the warm and cold far-infrared - radio correlation by [Xu et al. \(1994\)](#) and [Pierini et al. \(2003\)](#) I present results for a sample of 725 objects. This number is an order of magnitude larger than the sample studied by [Pierini et al. \(2003\)](#). To establish the peak temperature of the dust emission [Pierini et al.](#) used 60, 100 and 170 μm data from the Infrared Space Observatory (ISO), here 140 μm data is used in addition to *IRAS* 12, 25, 60 and 100 μm data to extend the spectral coverage longwards of the expected peak at $\approx 100\mu\text{m}$. I do not follow the method of fitting two modified blackbody functions to isolate the warm and cold dust components. Instead I follow a simpler method of extracting dust temperatures by SED fitting of *IRAS* 60 and 100 μm fluxes plus *AKARI* flux at 140 μm , using the IDL program of [Casey \(2012\)](#), setting the parameters α to 2.0 and β to 1.5, here α is the Mid-IR Power-law Slope and β is the dust emissivity index, these values are those adopted by [Casey](#) following the measurement of these parameters on a sample of 48 galaxies. The warm and cold samples are then obtained by applying a cut at the median of the sample at 24 K then labelling the two samples either side of this cut as ‘warm’ above 24 K and ‘cold’ below 24 K.

Figure 3.1a reproduced from [Pierini et al. \(2003\)](#), illustrates the radio luminosity at 1.4

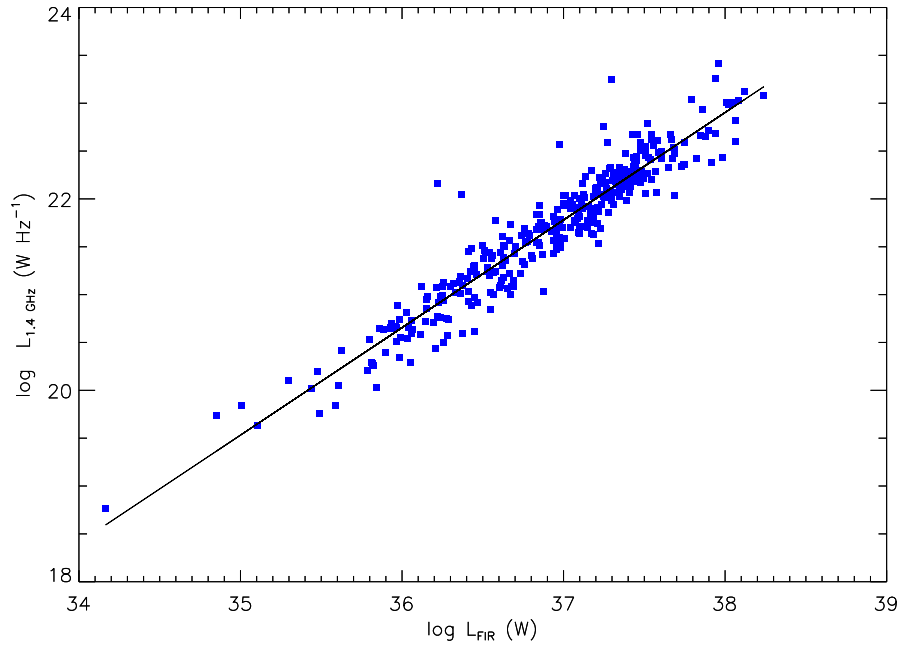


Figure 3.4: The radio luminosity at 1.4 GHz vs. the total FIR luminosity for a sample of 356 cool objects selected with a temperature below 24 K. The slope of the correlation is 1.13 ± 0.03 .

GHz vs. the total FIR luminosity of the warm component for their sample of 72 objects where the slope of the correlation was found to be 1.03 ± 0.03 . My sample of 369 ‘warm’ galaxies illustrated in Figure 3.3, is found to have a linear slope of 1.06 ± 0.03 . Similarly Figure 3.1b reproduced from Pierini et al. (2003), illustrates the radio luminosity at 1.4 GHz vs. the total FIR luminosity of the cold component of their sample of 72 objects, this can be compared to the ‘cold’ sample of 356 independent objects plotted in Figure 3.4. The slope of the cold sample at 1.13 ± 0.03 is a good match to that found by Pierini et al.. Figure 3.5 is a plot of the full sample of 725 objects spanning the temperature range $9 \text{ K} < T < 44 \text{ K}$ having a mean of 24.2 K. The slope of the correlation across this temperature range is found to be 1.09 ± 0.04 . Figure 3.6 is a composite plot of ‘warm’ and ‘cold’ labeled galaxies displaying similar distributions for each sample the mean q_{TIR} of the total sample is 2.65 ± 0.01 ($\sigma=0.24$).

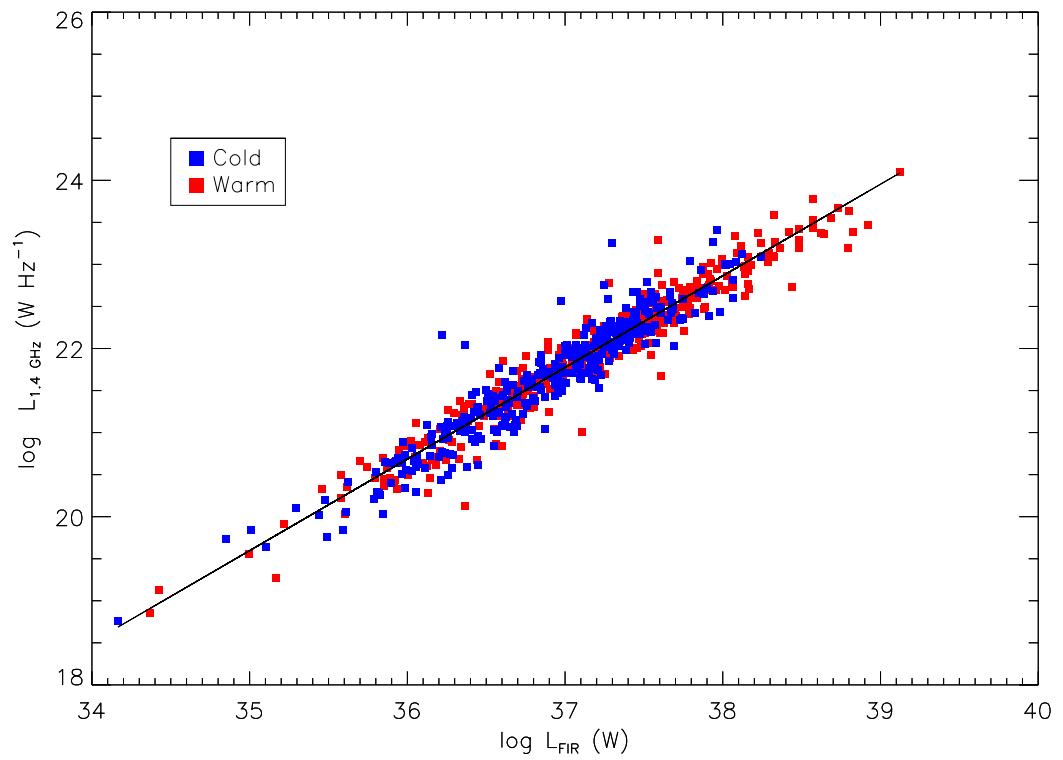


Figure 3.5: The radio luminosity at 1,4 GHz vs. the total FIR luminosity for a sample of 725 objects. Warm objects are selected to have a temperature above 24 K and cool objects are selected to have a temperature below 24 K. The slope of the correlation is 1.09 ± 0.04

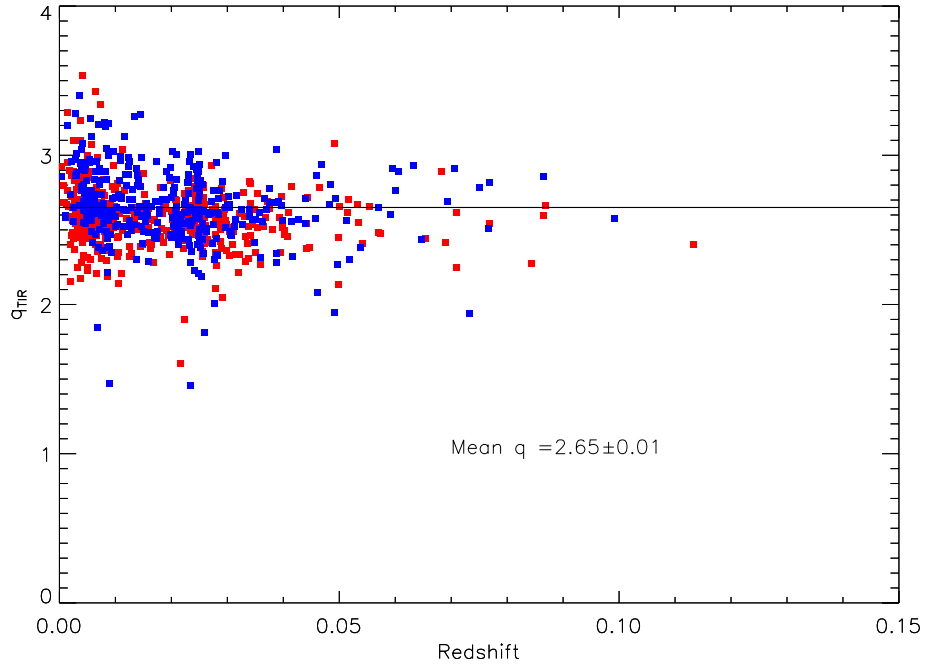


Figure 3.6: q_{TIR} of the sample plotted against redshift for the complete sample of both cool (blue) and warm (red) objects. The mean q_{TIR} of this sample is 2.65 ± 0.01 ($\sigma=0.24$).

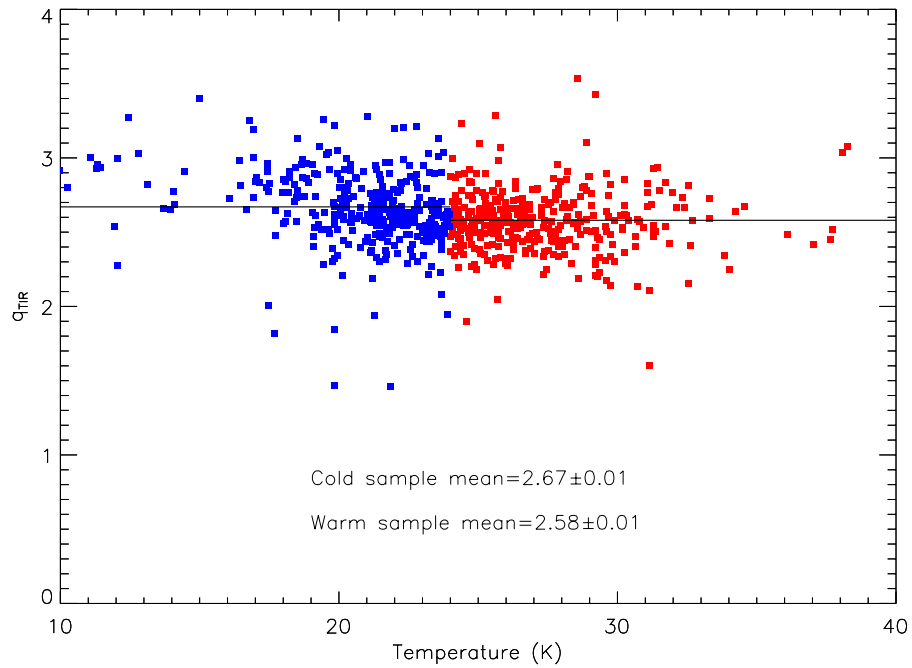


Figure 3.7: q_{TIR} of sample plotted against temperature. The sample is split at 24 K, with the mean q for each group indicated by the horizontal line. The cool (blue) sample has a mean q_{TIR} of 2.67 ± 0.01 (σ 0.20) and the warm (red) sample has a mean q_{TIR} of 2.58 ± 0.01 ($\sigma=0.20$).

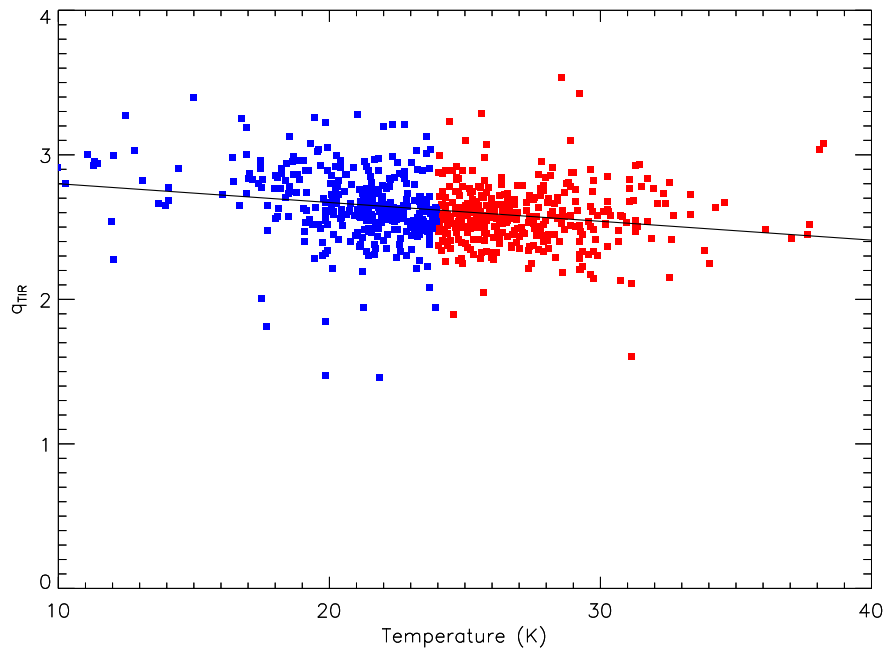


Figure 3.8: A linear fit in q_{TIR} to the warm and cold sample indicates a slope (-0.013 ± 0.002) towards higher temperatures.

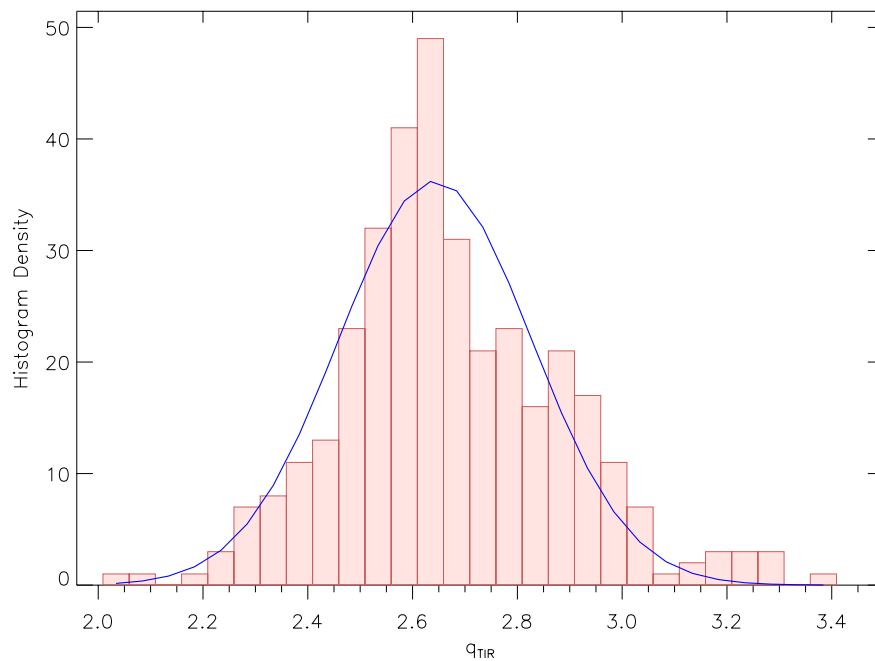


Figure 3.9: Histogram of the cold sample. This plot illustrates the distribution of q for this sample for temperatures below 24 K. The curve is a gaussian fit to the cold sample with a peak at $q_{\text{TIR}}=2.64 \pm 0.01$ ($\sigma=0.16$)

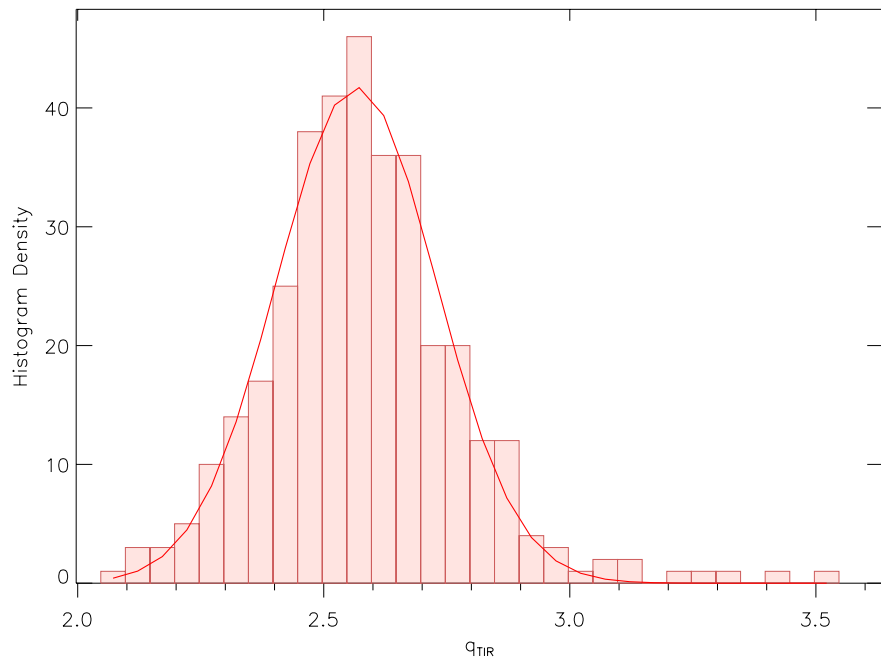


Figure 3.10: Histogram of the warm sample. This plot illustrates the distribution of q for this sample for temperatures above 24 K. The curve is a gaussian fit to the warm sample with a peak at $q_{\text{TIR}} = 2.57 \pm 0.01$ ($\sigma = 0.16$)

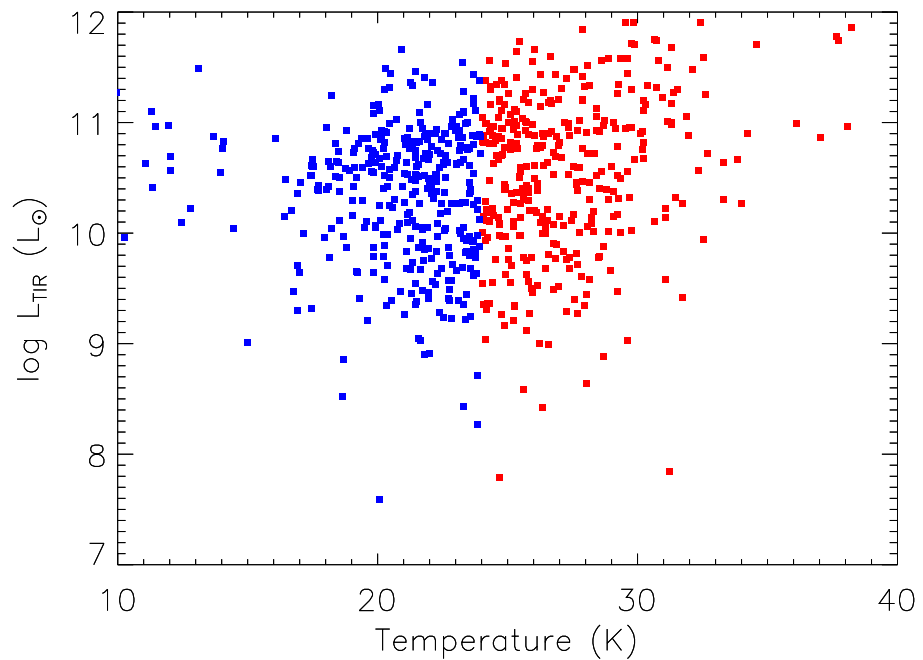


Figure 3.11: Luminosity of the complete sample plotted against temperature. The warm (red) sample has a greater dispersion in luminosity than the cool (blue) sample.

In order to compare results with the general exploration of the FIRC in Chapter 2. I now calculate q for both warm and cold samples (assigning a radio synchrotron spectral slope of $\alpha = 0.8$ when calculating q). I find a small difference in q_{cold} (Temp < 24 deg) and q_{warm} (Temp > 24 deg) for the sample area as shown in Figure 3.7.

I compute statistics for warm and cold samples using the the IDL function IMSL-NORM2SAMP which computes statistics using samples from two independently normal populations. The means returned for the two samples are:

$$q_{\text{cold}} = 2.67 \pm 0.01 \ (\sigma=0.21)$$

$$q_{\text{warm}} = 2.58 \pm 0.01 \ (\sigma=0.20)$$

The difference in the means is small at 0.085. Assuming a null hypothesis that the temperature and q are not related I calculate the Pearson p-value to test the significance of this result. I first extract the t-statistic as 5.42, then calculating the p-value with the t-statistic returns < 0.00001. From this result I conclude that the null hypothesis is rejected.

A linear fit in q_{TIR} to the warm and cold sample shown in Figure 3.8 reveals a slope of -0.013 ± 0.002 from cold towards warmer temperatures. The correlation coefficient (Pearson r-value) for this slope is -0.2, indicating a weak linear relationship. This slope can be compared to the split in q for the warm and cold samples shown in Figure 3.7. Although this is a small trend I find this to be an interesting result.

A gaussian is fitted to the histogram of the ‘cold’ sample shown in Figure 3.9 which gives a similar q of 2.64 compared to q_{cold} of 2.67 not withstanding the rather peaky distribution. A fit to the ‘warm’ sample shown in Figure 3.10 returns a q of 2.57, also close to previously noted q_{warm} of 2.58. In the case of the warm sample the data is a better match to a gaussian. Figure 3.11 plots the Log L_{TIR} of the complete sample of warm and cold objects against temperature. Inspection of this plot reveals a tendency to a higher dispersion at higher temperature, also more high luminosity objects appear to be present at higher temperatures.

Table 3.1 divides the whole sample into various luminosity blocks and slices. Inspection of the mean q_{cold} and mean q_{warm} for each sample shows that in the majority of cases the ratio q_{warm} is lower than the ratio q_{cold} . Only in the highest redshift slice and highest luminosity is the mean q_{warm} seen to be higher than the mean q_{cold} .

Table 3.1: q_{LTIR} of cold and warm samples in luminosity and redshift blocks and slices

z range	Luminosity range	q_{cold}	q_{warm}
$z < 0.01$	$L > 9.5$	2.68	2.60
$z < 0.02$	$L > 10$	2.65	2.56
$z < 0.04$	$L > 10.7$	2.52	2.53
$z < 0.06$	$L > 11.0$	2.56	2.54
$z < 0.01$	$9.5 < L < 10.0$	2.71	2.63
$z < 0.02$	$10.0 < L < 10.5$	2.67	2.56
$z < 0.04$	$10.7 < L < 11.0$	2.64	2.53
$z < 0.06$	$11.0 < L < 11.5$	2.56	2.54
$0.02 < z < 0.04$	$L > 10.7$	2.52	2.52
$0.04 < z < 0.06$	$L > 11.0$	2.51	2.56

3.3 Discussion

Of the two mechanisms behind the FIRC, the intensity of the FIR radiation is directly related to the temperature of the dust particles heated by the radiation emitted by massive young stars. This component is the *warm dust* with $T \sim 40$ K. A second FIR radiation source is that from *cool dust* with $T \sim 20$ K. The source here is the general interstellar UV ($912 < \lambda < 3000$ Å) radiation field found within galactic discs and is attributed to the emission from late type A and B stars (Xu, 1990).

This chapter presents an analysis of the Far-infrared - radio correlation in terms of galaxy peak temperatures using *IRAS* 60 and 100 μm flux densities plus *AKARI* 140 μm to extend the spectral coverage long-wards of the peak SED. From an original sample of 725 I have then split these into 369 ‘warm’ and 356 ‘cold’ objects by dividing the sample at a temperature of 24 K.

In terms of various groupings in luminosity and redshift I find that except at the highest redshift and luminosity the mean q_{warm} is generally lower than q_{cold} . In Figure 3.7 I plot two distinctly different mean q s for the cold and warm samples. Also when plotting q_{LTIR} against temperature in Figure 3.8 a line fit through the sample has a negative slope illustrating a general trend towards a lower mean q_{LTIR} ratio with increasing temperature. This is the most interesting result to emerge from this research and does, I believe, warrant a future investigation to confirm or refute the finding.

I have identified a variation in q that correlates with peak dust temperature of galaxies. The mean q of the cold sample is higher than that found for the warm sample with q ratios of 2.67 ± 0.01 and 2.58 ± 0.01 respectively as illustrated in Figure 3.7. The linear fit to the warm and cold sample illustrated in Figure 3.8 has a slope of -0.013 ± 0.002 towards higher temperatures. The measured correlation coefficient for this slope is -0.2, indicating a weak linear relationship which could be re-tested with a larger sample in the future.

Initial postulated reasons for higher q in the cold sample are a higher FIR flux than found in the mean sample or conversely a lower radio flux. For the warm sample the inverse situation could apply with a lower FIR flux or higher radio flux attributed to a higher likelihood of finding AGN at higher temperatures.

Later type spirals (Sc and SBc) and irregulars are expected to have a temperature distribution favouring colder dust temperatures which corresponds to my cold sample. Whereas early type spirals (Sa and SBa) are expected to have a temperature distribution favouring warm dust temperatures which corresponds to my warm sample. The later type spirals have discs dominated by young blue stars and therefore will have a higher UV

output, and consequently higher FIR flux than early type spirals which have old red stars, little gas and large amounts of dust (Popescu et al., 2002).

I have compared the mean qs of ‘warm’ and ‘cool’ galaxies. A plot of the complete sample of warm and cold galaxies plotted against temperature, Figure 3.11, shows the greatest dispersion in the warm sample. The mean $q=2.67$ of the cold sample is close to that of the whole sample where $q=2.65$, this indicates that the cold sample is closely following the FIRC, whereas the warm sample has more outliers some with strong FIR and some with strong radio, with a general trend towards a lower q ratio towards higher temperatures. This is possibly indicative of a lower rate of star formation from an ageing population of stars whilst a synchrotron radio flux is still being emitted as a result of SN at the end of vigorous star formation.

Popescu et al. (2002) fit two modified blackbody functions to a sample of galaxies, and then predict a tight FIRC for the cold dust component attributed to a young stellar population heating the dust by UV radiation. This same population also gives rise to synchrotron radiation via SN at the end of their lifetime. Although this prediction is based on a small sample of 14 galaxies they confirm the correlation for the cold sample. A fit to the warm component is seen to be nonlinear, this the authors find difficult to explain if the calorimeter theory holds.

Chapter 4

The Far-Infrared Radio Correlation at low radio frequencies

4.1 Introduction

The far-infrared radio correlation has been well explored at 1.4 GHz, and to a much lesser extent at lower radio frequencies. At the present time there is a construction boom of new low frequency distributed array radio telescopes, see Figure 4.1 for frequency coverage and baselines. The most ambitious of these being the Low Frequency Radio telescope (LOFAR) ([van Haarlem et al., 2013](#)). The LOFAR interferometric array of radio telescopes is to comprise of many stations across Europe with a core centred on the Netherlands, and will be dedicated to observations at radio-frequencies below 240 MHz, in two bands down to 10 MHz with a break from 88 to 110 MHz dominated by terrestrial broadcasts ([Falcke, 2006](#)). Two more radio array telescopes to note are the Murchison Widefield Array (MWA) ([Tingay et al., 2013](#)) and the Long Wavelength array (LWA). Between them these radio telescopes will open up a new window to one of the most poorly explored regions of the electromagnetic spectrum ([Kassim et al., 2005](#)). In the near future LOFAR will be extending the observable spectrum to metre wavelengths at high resolution. There is also a proposal for a Giant Metrewave Radio Telescope (GMRT) ([Sirothia et al., 2014](#)) 150 MHz survey that is expected to return a four times improvement in sensitivity and angular resolution over existing low frequency radio surveys: the WENSS (325 MHz) ([de Bruyn et al., 2000](#)) and VLSS (74 MHz) ([Cohen et al., 2006](#)). These new low frequency radio observatories will extend our knowledge of radio SEDs, identifying sources deviating from

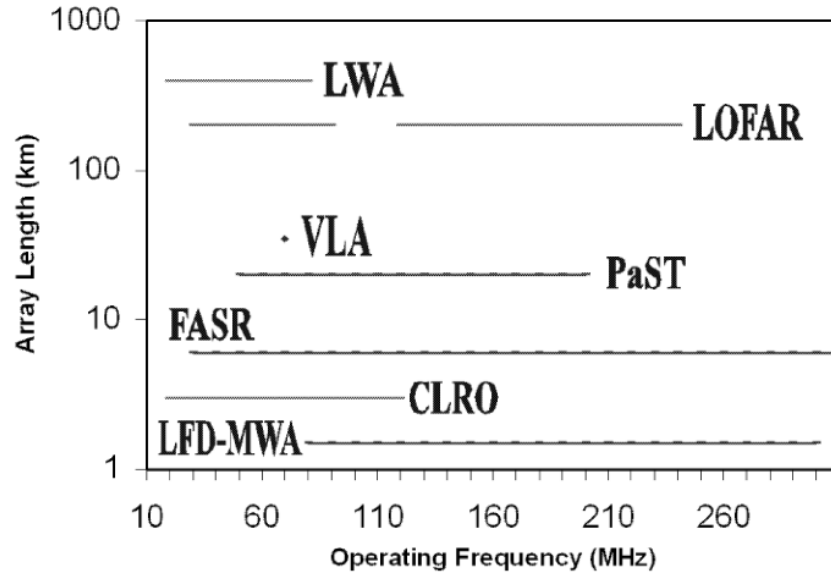


Figure 4.1: Wavelength coverage and baselines of past, present and future Low frequency arrays compared. The arrays are the Long Wavelength Array (LWA), Low Frequency Array (LOFAR), Very Large Array (VLA), PaST (Primeval Structure Telescope), FASR (The Frequency Agile Radio Telescope), Clark lake Radio Observatory, and the Low Frequency Demonstrator - Mileura Wide-field Array (LFD-MWA). Plot taken from *Low Frequency Radio Astronomy* (Clark et al., 2005).

the continuum spectrum such as Gigahertz Peaked Spectrum (GPS) sources which peak around 1GHz and Compact Steep Spectrum sources (CSS) which deviate from the linear having convex radio spectra (Tschager et al., 2003) also spectral turnover such as observed in M33 where the spectrum turns and flattens below 900 MHz (Israel et al., 1992).

The far-infrared radio correlation is conventionally studied at a radio frequency of 1.4 GHz. One notable exception in this respect was the investigation of the correlation between the far-infrared and the non-thermal radio emission at 151 MHz by Cox et al. (1988). This particular investigation was completed with a small 145 object sample and compared objects from the *IRAS Point Source Catalogue* and radio data from the 6C radio survey (Waldram, 1998). While investigating the FIRC Cox et al. identified two populations; Sample I, comprised of nearby spiral galaxies which were FIR-loud and Sample II which were brighter in the radio than Sample I but relatively faint in the FIR. The main focus of that work was Sample I, comprised of 74 sources, which confirmed the far-infrared radio correlation, whilst Sample II exhibited a scattered distribution as shown in plot 4.2. Modelling the FIR to radio luminosity and comparing the star formation and supernovae rates was found to lead to predicted FIRC ratios higher than observed in the sample. This

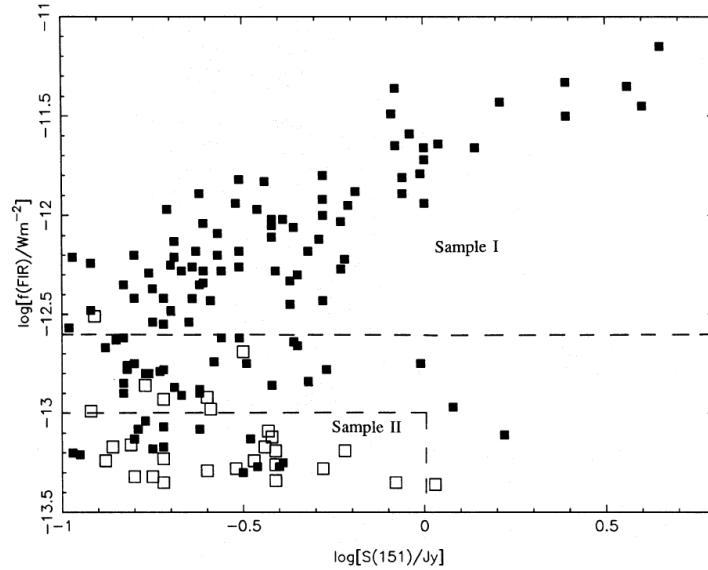


Figure 4.2: FIRCOR at 151 MHz. Plot of FIR flux against radio flux density at 151 MHz. The limits of the two samples are indicated. Figure from [Cox et al. \(1988\)](#) Figure 3.

leads the authors to conclude that the observed radio emission cannot be attributed solely to individual supernova remnants but must result from accelerated cosmic ray electrons within the ISM interacting with the host galaxy magnetic field, resulting in the higher levels of observed Synchrotron emission compared to that predicted ([Cox et al., 1988](#)).

4.2 The FIRC at 74 MHz

The FIRC has been shown to hold down to 151 MHz, the investigation now looks to see if the far-infrared radio correlation holds to lower radio frequencies, where the emission is expected to be predominantly non-thermal. To extend the pioneering work at 151 MHz I now make use 74 MHz (4m) data from the VLA VLSS 4m survey ([Condon et al., 1998](#)) cross matched to the IRAS PSCz catalogue ([Helou & Walker, 1988](#)).

The original Very Large Array (VLA) Low Frequency Sky Survey (VLSS) 74 MHz. Survey ([Cohen et al., 2006](#)) has undergone a re-reduction of its data and is now re-released as the VLSS redux (VLSSr. [Lane et al., 2012](#)). The end result is an improved catalogue with number of sources increased by 35% to 93,000 and includes six previously unpublished fields. At meter wavelengths the ionosphere distorts the incoming wavefront and consequently a good ionospheric model is required to correct positional error. The original VLSS did not have an available sky model at 74 MHz but used the NVSS 1.4 GHz data and an assumed spectral index $\alpha = 0.7$. By reusing the original VLSS catalogue as a same

Table 4.1: Radio surveys at Low frequency

Field	Instrument	Frequency	Area (deg ²)	Reference
ϵ Eridani	GMRT	150MHz	2	George et al. 2008
xFLS	GMRT	610MHz	4	Garn et al. 2007
ELAIS-N1	GMRT	610MHz	9	Garn et al. 2008a
Lockman Hole	GMRT	610MHz	5	Garn et al. 2008b
ELAIS-N2	GMRT	610MHz	6	Garn et al. 2009

Note: GMRT 610 MHz data reproduced from [Garn & Alexander \(2009\)](#)

frequency sky model catalogue [Lane et al.](#) found that it was possible to achieve better positional fits. Other improvements are listed in the following redux overview:

The VLSSr represents a major improvement to the original VLSS over most of the sky. It includes six previously unpublished fields, and improved dynamic range in 95% of all fields. The clean bias has been halved and is now 0.66 times the local RMS. The largest angular size imaged has been roughly doubled to 36 arcmin, and the number of cataloged sources is increased by 35% to 93,000 ([NRAO, 2013](#)).

4.2.1 Low frequency turnover

At the time of writing the low frequency regime < 1.4 GHz is poorly explored and awaits the first all sky survey with LOFAR which will explore the low frequency radio emission of galaxies at frequencies down to tens of MHz at sensitivities of a few mJy. Of particular interest will be the Multifrequency Snapshot Sky Survey (MSSS) covering a frequency range of 30 to 74 MHz with its low frequency array antennae, and 120 to 160 MHz with its high band antennae ([Astron, 2013](#)). The latest news on the MSSS suggests a public release of the high band catalogue by mid-2014.

Little work has been done on the determination of low frequency radio spectra for larger samples of galaxies. Investigations into the FIRC at low frequency have been limited to small fields (Table 4.1) for example, observations 610 MHz in the Spitzer extragalactic First Look Survey field ([Garn & Alexander, 2008](#)). Synchrotron sources are expected to have a turnover or flattening in their spectra at low frequency due to absorption, either synchrotron self absorption or thermal absorption ([Israel & Mahoney, 1990](#); [Hummel, 1991](#)). The self absorption cut-off frequency constrains the magnetic field strengths of

sources, and the thermal absorption constrains the temperature and density of the interstellar medium (ISM) (de Bruyn et al., 2002). There is an existing class of Step Spectrum sources that gives an indication of these processes. These are Gigahertz Peaked Spectrum (GPS) radio sources characterised by their radio spectrum peaking at around 1 GHz before declining towards lower frequencies and Compact Steep Spectrum sources (CSS) peaking around 100 MHz. These are not standard star forming galaxies but Active Galactic Nuclei (AGN) or young radio sources yet to evolve into large radio galaxies. (Snellen et al., 1998) Details of GPS and CSS sources are given in O’Dea (1998).

Lacki (2013) describes the ways in which low frequency radio emission can be absorbed. From free free absorption to the Razin effect, the latter of these processes is where the refractive index in the emitting region is reduced to less than unity due to the presence of thermal plasma decreasing the synchrotron radiation intensity. Although considered to be the most important process is ‘free-free absorption’ where free electrons gain energy during collisions with ions by absorbing photons. It is this free-free absorption that is expected to flatten or lead to low frequency spectral curvature in the radio spectra of starburst galaxies.

4.2.2 Data

The primary data source for this investigation into the FIRC with radio flux at a frequency of 74 MHz is the VLSSr catalogue (Lane et al., 2012). This catalogue has complete coverage between the declination limits of +90.0 and -10.0 deg with further coverage in parts to -30 deg. Complimentary far-infrared data is taken from the *IIFSCz* catalogue of Wang & Rowan-Robinson (2009).

To build a catalogue of 74 MHz sources complete with *AKARI* flux densities plus 1.4 GHz flux densities the following procedure was used: Initially the *IIFSCz* catalogue was matched to the *AKARI* catalogue using TOPCAT, a Tool for Operations on Catalogues and Tables (Taylor, 2005), with the search radius set at 20 arcsec. Finally I match the resulting *IIFSCz-AKARI* catalogue to the 74 MHz VLSSr catalogue using TOPCAT. The VLSSr has a resolution of 75 arcsecs³ plus *AKARI* 140 μm , which is the most complete

³The original VLSSR survey is quoted to have a beam = 80" x 80" (Cohen et al., 2006). I initially limited the search radius set in TOPCAT to 60 arcsec to limit the probability of making false associations between these galaxies. To test the number of spurious matches I estimated the false matching rate (FMR). Applying a shift of 5 arcmin to the DEC co-ordinates revealed an FMR of $\approx 33\%$. Reducing the search radius to 20 arcsec reduced the FMR to $\approx 1\%$. The resulting catalogue complete with *AKARI* data at 65, 90, 140 and 160 μm matched to the 74 MHz radio flux from the VLSSr is limited to 48 galaxies.

wavelength sample in that catalogue. Both catalogues have complementary 1.4 GHz radio fluxes and redshifts from the *IIFSCz* catalogue. Search radii were set to match the previous sample. Galaxies in this final match are classified as follows: 55 spirals, 14 starbursts, 7 ellipticals and 19 unclassified according to the optical galaxy template types quoted in the *IIFCz* catalogue

The number of matches obtained is low at 95, this represents a small fraction of the sources listed in the cited catalogues. Inspection of the matched sources reveals that the minimum 1.4 GHz flux where I find a match to a 74 MHz source is > 3.0 mJy . Whereas 74 MHz sources in the VLSSr catalogue are typically > 300 mJy. Counting 1.4 GHz sources in the *IIFSCz* catalogue which are > 3.0 mJy reveals $> 10,000$ which match this criteria. I also find that the $100\mu\text{m}$ *IRAS* flux is not a reliable indicator of detecting a VLSSr 74 MHz radio flux.

4.2.3 Spectral Index

At frequencies around 1 GHz and higher the spectral index is typically ~ -0.8 . As discussed in Section 4.2.1, the power law radio spectra, which is predominantly due to synchrotron radiation, is expected to flatten at MHz frequencies due to absorption. When calculating q_{74} I need to know the appropriate spectral index for the synchrotron radio spectra when applying a k -correction to the data.

I calculate the spectral index for the main sample of 134 galaxies between the radio flux densities at 74 MHz and 1.4 GHz using Equation 2.8 and find a mean of $\alpha = -0.6 \pm 0.07$. The error quoted here was obtained using the error propagation equation

$$\sigma_{\alpha} = \frac{\sqrt{\left(\frac{\delta S_1}{S_1}\right)^2 + \left(\frac{\delta S_2}{S_2}\right)^2}}{\ln(\nu_1/\nu_2)} \quad (4.1)$$

See Figure 4.3 for a histogram displaying the dispersion in the spectral index. When k -correcting radio flux densities at 74 MHz I adopt a universal $\alpha = -0.6$. I list in table 4.2 the characteristics of galaxies found to have lower spectral indices than the mean. Only one of these sources is classed as a starburst galaxy, the remainder are highly luminous in the infrared including those classified as LIRGs and ULIRGs or strong in the radio. Some of the sources are characterised as having a flat radio spectrum. This selection of low spectral indices (SI) illustrates that at 74 MHz the synchrotron is flattening out for some galaxies and therefore a single SI may not be appropriate in all cases.

I build a larger catalogue of 95 galaxies comprised of *IRAS* 12, 25, 60 and $100\mu\text{m}$

Table 4.2: Sources with a low spectral index at 74 MHz

IRAS	Name	Classification	Spectral Index
F00460+3141	NGC0262	Sy II radio source	-0.29
F013448+3254	3C048	Extremely radio loud quasar	-0.05
F01403+1323	NGC0660	Sy II	-0.32
F02368-0828	NGC1052	Elliptical Sy II, inverted radio spectrum	0.02
F04305+0514	3C120	Sy I	-0.31
F06098+7103	UGC3426	SyII, one of pair (Radio jet)	-0.24
F08519+2017	OJ+287	BL Lac (AGN)	0.3
F09293+2143	NGC2903	Starburst	-0.07
F09517+6954	M82	FR I	-0.37
F12176+2933	NGC4278	Strong LINER and radio loud	-0.04
F12535-0530	3C279	QSO superluminal (AGN)	-0.39
F12265+0219	3C273	Radio loud quasar	-0.34
F12540+5708	MRK231	ULIRG, Flat spectrum radio source	-0.39
F13170-2708	NGC5078	Flat spectrum radio source	-0.31
F13277+4727	M51a	Sy II, one of pair	-0.29
F14106-0258	NGC5506	Most luminous local Seyfert	-0.17
F16577+5900	NGC 6286	LIRG	-0.4
F17537+1820	NGC 6500	Flat spectrum radio source	-0.37
F23389-0300	4C+03.60	ULIRG	-0.23
F23532+2956	CGCG498-038	Sy II	-0.34

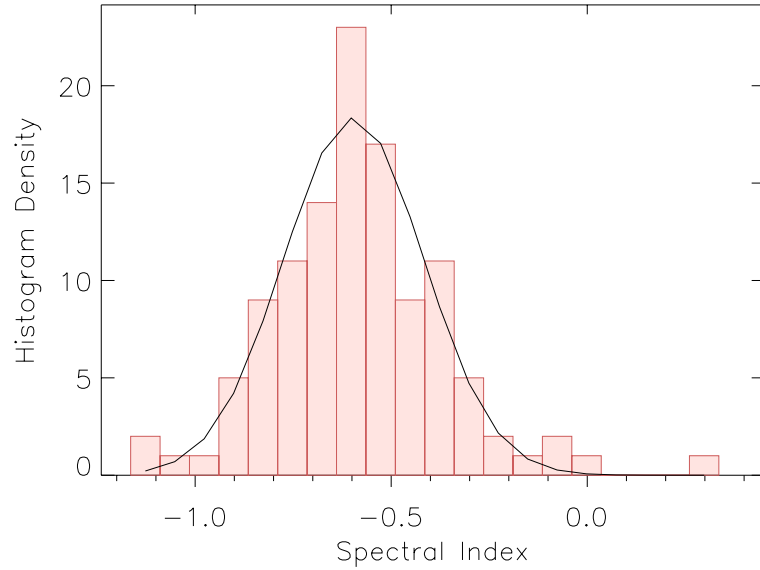


Figure 4.3: Histogram displaying the dispersion in Spectral index between 1 GHz and 74 MHz, with a mean of $\alpha = -0.6 \pm 0.07$

4.3 Results

The FIRC of a subsample of (48) 74 MHz selected galaxies with matches to *AKARI* FIR data at 65, 90, 140 and 160 μm is compared to the correlation of the same sample with radio flux densities at 1.4 GHz data. Rest-frame total IR luminosities (8 - 1000 μm) were calculated as in Chapter 3, using the IDL program of Casey (2012), setting the parameters α to 2.0 and β to 1.5, noting that here α is the Mid-IR Power-law Slope and β is the dust emissivity index. The rest-frame radio luminosity was calculated with Equation 2.16, with the spectral index set at -0.8 for the 1.4 GHz sample and -0.6 for the 74 MHz sample. Using Equation 3.4 the q_{TIR} was calculated with the radio sample at 1.4 GHz, then with the radio sample at 74 MHz. Referring to Figure 4.4 the q_{TIR} is plotted for the two samples. The q_{TIR} at 1.4 GHz (black symbols) has a mean of 2.4 ± 0.04 and the q_{TIR} at 74 MHz (red symbols) has a mean of 1.77 ± 0.05 . Cuts were not applied to the data sets when calculating mean q values as none of the 1.4 GHz sample had q values below 1.8, the level below which I have previously designated as radio loud. By comparing the mean q_{TIR} at 74 MHz with the q_{TIR} at 1.4 GHz I determine that a reasonable cut-off level for radio loud galaxies in the 74 MHz sample should be below $q = 1.1$. No cut is therefore required for the 74 MHz sample.

Figure 4.5 is a comparison of q_{TIR} at 1.4 GHz and q_{TIR} at 74 MHz. Galaxies are colour coded according to their type as indicated in the IIFCz catalogue optical templates listing

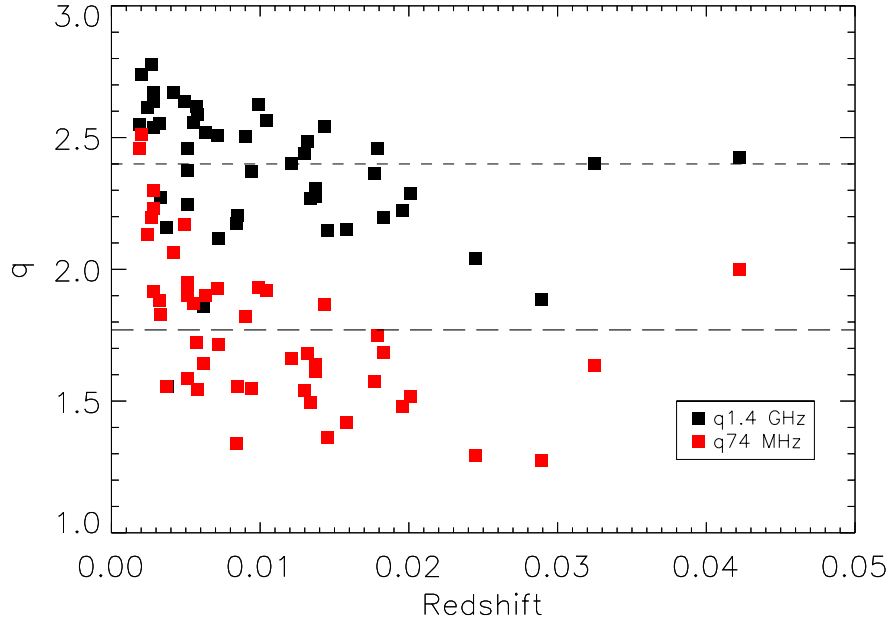


Figure 4.4: The q of the comparison sample at 74 MHz and 1.4 GHz was calculated using *AKARI* data at 65, 90, 140 and 160 μm . Where the q of the 74 MHz and 1.4 GHz samples (denoted by red and black symbols respectively) are plotted against redshift. The spectral index α is set at a mean value of -0.6 when k -correcting the radio flux at 74 MHz and -0.8 at 1.4 GHz.

(Rowan-Robinson et al., 2008). No preference for a tighter correlation by galaxy type is identified in this sample. In particular elliptical galaxies are seen to be amongst the most tight and loosest bound. In this small sample no particular deviation from the mean q at 1.4 GHz is identified.

Having established an offset in the $q_{74\text{MHz}}$ and $q_{1.4\text{GHz}}$ ratios I now look at the FIRC with the larger 95 galaxy sample built from *IRAS* 25, 60 and 100 μm plus 140 μm *AKARI* flux densities. Plotting the $q_{74\text{MHz}}$ and $q_{1.4\text{GHz}}$ results for this sample (Figure 4.6) it is seen that there are many radio loud galaxies. I therefore apply cuts to both samples to eliminate the radio loud galaxies below $q = 1.8$ for the 1.4 GHz sample and $q = 1.1$ for the 74 MHz sample. Following application of the cuts I calculate the mean q of the 1.4 GHz selected radio sample = 2.35 ± 0.02 and the mean q of the 74 MHz selected radio sample = 1.72 ± 0.02 , these are seen to be in agreement with the previous *AKARI* selected sample. I have colour coded Spirals as orange, Ellipticals red and Starburst as violet in Figure 4.6. Examination of this plot reveals no bias for any particular class of object to fall on or near the mean q for the 74 MHz selected sample.

Over the frequency range 1 - 10 GHz the non-thermal radio emission has a power law

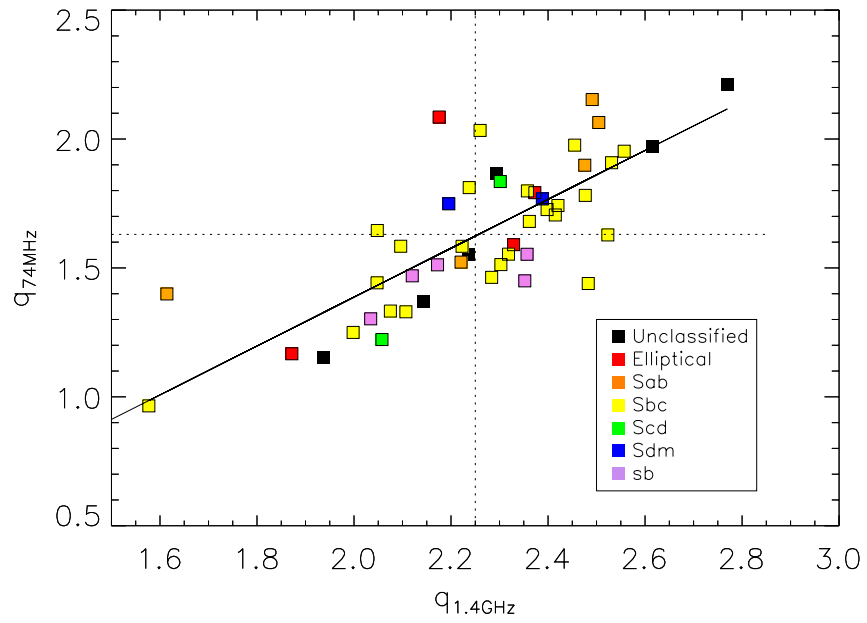


Figure 4.5: *AKARI* 65, 90, 140 and 160 μm fluxes were employed to calculate rest frame q_{LTIR} (8 - 1000 μm) for 48 galaxies where 74 MHz observations are matched to objects in the *IIFCz* catalogue. The mean $q_{74\text{MHz}}$ was found to be 1.77 ± 0.05 compared to the q at 1.4 GHz with a mean of 2.40 ± 0.04 . The dispersions for these two samples are 0.34 and 0.27 respectively.

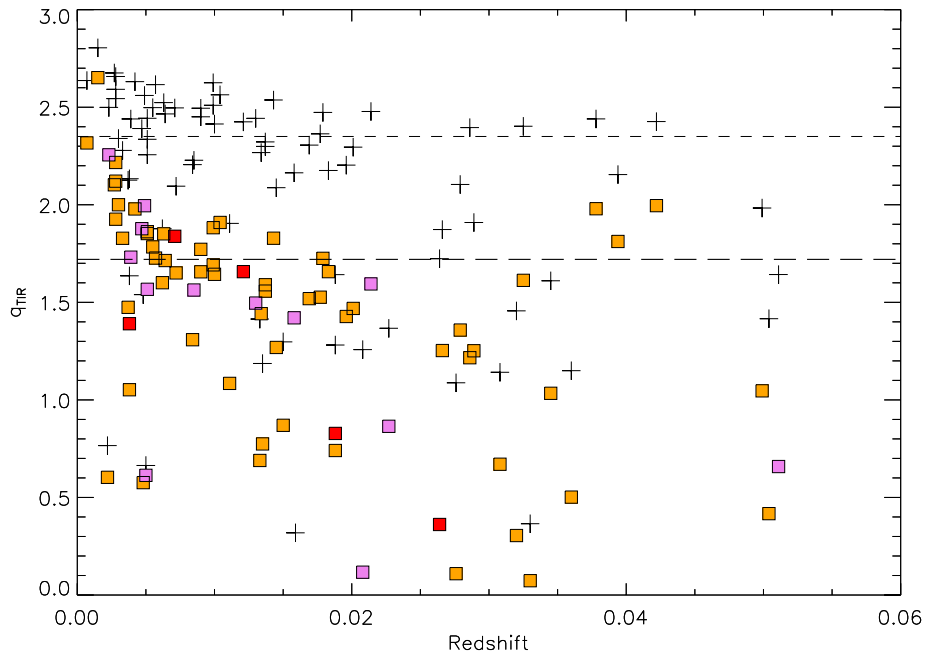


Figure 4.6: $q_{1.4\text{GHz}}$ vs. $q_{74\text{MHz}}$ using TIR luminosities calculated from IRAS 12, 25, 60 and 100 μm plus AKARI 140 μm flux densities. Crosses show $q = \log(\text{TIR}/21\text{cm})$ and squares show $q = \log(\text{TIR}/4\text{m})$. Galaxies are colour coded where Spirals are orange, Ellipticals red and Starburst violet. The mean q of the 1.4 GHz selected radio sample = 2.35 ± 0.02 ($\sigma = 0.22$) The mean q of the 74 MHz selected radio sample = 1.72 ± 0.02 ($\sigma = 0.22$).

spectrum with a mean spectral index of $\alpha = -0.8$. I have shown that at 74 MHz there is lowering of the spectral index to a mean of -0.6 with some sources having α approaching zero. The lowering of the spectral index in spiral galaxies is observed by [Hummel \(1991\)](#) who reports that many galaxies in this class exhibit a break in their radio spectrum at ≈ 700 MHz, below this frequency the spectral index is reported to be reduced by 0.25 ± 0.05 which is inline with my findings.

It has been predicted that the non-thermal radio spectrum will undergo a turnover at these long wavelengths due to absorption of the synchrotron radiation. [Israel et al. \(1992\)](#) show that the radio spectrum of M33 has a turnover between 500 and 900 MHz, which is attributed to free-free absorption by cool ($T_e < 1000$ K) ionised gas. Investigation of the far-infrared radio correlation at low frequencies may lead to better understanding of these processes.

4.4 Discussion

In this chapter I have made a preliminary exploration of the FIRC at low radio frequencies beyond the previous study at 150 MHz by [Cox et al. \(1988\)](#). The main findings are that at 74 MHz the correlation still holds although the q ratio is lower than at 1.4 GHz, with a new mean $q \approx 0.7$ lower. Around 10% of galaxies have a spectral index that deviates significantly from the mean of -0.6 . [Hummel \(1991\)](#) suggested that the synchrotron spectra would deviate from being linear at frequencies below ≈ 1 GHz, with an associated change in the spectral index.

Over the frequency range $10^1 - 10^{10}$ MHz the non-thermal radio emission has a power law spectrum with a mean spectral index of $\alpha = -0.8$. I have shown that at 74 MHz there is a lowering of the spectral index to a mean of -0.6 with some sources having α approaching zero. The lowering of the spectral index in spiral galaxies is observed by [Hummel \(1991\)](#) who reports that many galaxies in this class exhibit a break in their radio spectrum at ≈ 700 MHz, below this frequency the spectral index is reported to be reduced by 0.25 ± 0.05 a result confirmed by my own research findings.

It has been predicted that the non-thermal radio spectrum will undergo a turnover at these long wavelengths due to absorption of the synchrotron radiation. [Israel et al. \(1992\)](#) show that the radio spectrum of M33 has a turnover between 500 and 900 MHz, which is attributed to free-free absorption by cool ($T_e < 1000$ K) ionised gas. Investigation of the far-infrared radio correlation at low frequencies may lead to better understanding of these processes.

Chapter 5

FIRC with HerMES and GMRT

5.1 Introduction

This chapter studies the Far-Infrared - Radio Correlation in a relatively small area survey with excellent multi-frequency coverage. The field chosen for this chapter is one of the European Large Area *ISO* Survey (ELAIS) fields, originally defined for observation by ESA's Infrared Space Observatory (ISO, [Kessler et al. \(1996\)](#)). ELAIS N1 is located in the northern hemisphere (Figure 1.4). In common with other small fields ELAIS N1 was chosen to be in an area with a low infrared foreground, known to be clear of the dust emission (Cirrus contamination) from our own galaxy, a prerequisite for the detection of faint and distant objects ([Oliver et al., 2000](#)).

5.2 Hermes fields

Chapter one introduced the *Herschel*¹ Space Telescope. The results from *Herschel* are a quantum leap from previous ground based observations made with the 15-metre James Clerk Maxwell Telescope (JCMT) on Mauna Kea in Hawaii, observing through the atmospheric window open to wavelengths long-ward of 400 μm using a large area bolometric camera, SCUBA ([Dempsey et al., 2012](#)). Figure 5.1 compares the resolution of SCUBA to that of the *Herschel*-SPIRE instrument. The inset is a SCUBA image of the Hubble Deep Field at the same scale as the GOODS-North field observed by SPIRE. The HerMES survey described in section 1.4.2 observed fields with pre-existing ancillary data over a wide range of wavelengths from radio through to x-ray, see Fig 5.2.

¹Herschel is an ESA space observatory with science instruments provided by European-led Principal Investigator consortia and with important participation from NASA.

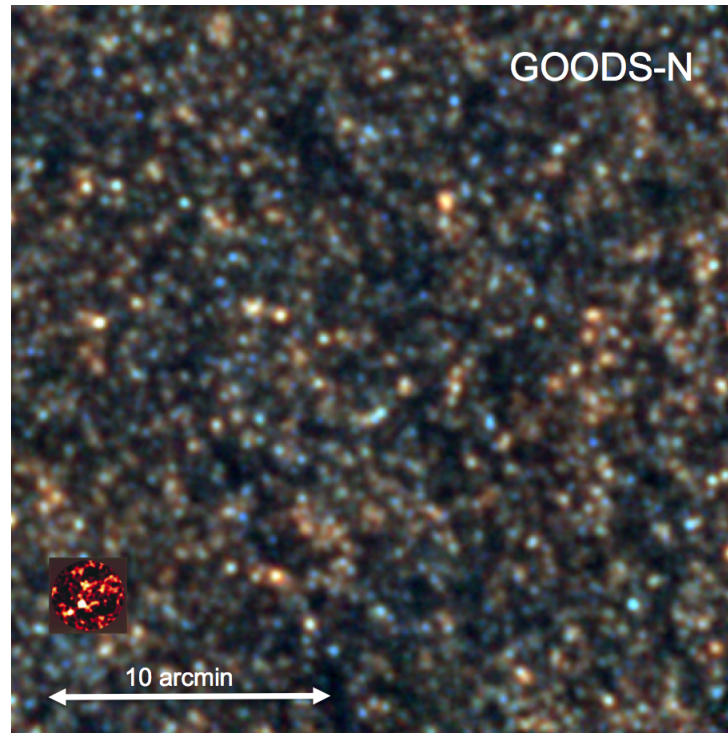


Figure 5.1: 900 arcmin² of the ‘Great Observatory Origins Deep Survey (GOODS) Field North observed by the Herschel Spectral and Photometric Imaging Receiver (SPIRE) at the wavelengths of 250, 350 and 500 μm over 14 hours. The inset imaged by the ground based SCUBA instrument at 850 μm shows an area of 9 arcmin² of the Hubble Deep Field (HDF) over a period of 50 hours. Image credit: ESA / SPIRE / HerMES

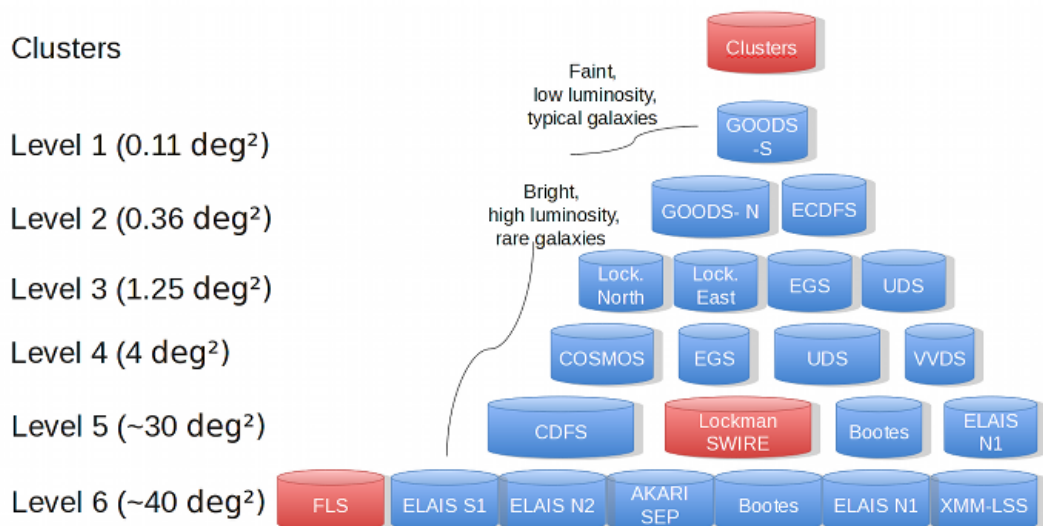


Figure 5.2: The ‘Wedding cake survey’ covering different depths and areas from level 1 (deep and narrow) to level 6 (wide and shallow).



Figure 5.3: GMRT at Pune. Picture credit: The National Centre for Radio Astrophysics (NCRA)

5.3 GMRT-the telescope

The source of low frequency radio data in this chapter is the Giant Metrewave Radio Telescope (GMRT) [Ananthakrishnan \(2005\)](#), illustrated in Figure 5.3. Located at a site adjacent to Khodad village 80 km north of Pune India (see Figure 5.2), and is comprised of 30 steerable parabolic antenna, each of 45 m diameter with a lightweight reflecting mesh surface supported by steel rope trusses. Fourteen of these dishes form a ‘randomly’ placed 1 km central cluster, the remaining sixteen are deployed in a three arm Y configuration, giving a maximum interferometric base line of 25 km. At this site the maximum observable declination range is between -55° and $+90^\circ$. The GMRT is dedicated to low radio frequency observations over the wavelength range of 6 m to 20 cm with a corresponding angular resolution of 60 to 2 arcsec. Feeds are available to cover 151, 325, 610 and the 1000-1430 MHz bands. The site was chosen to be as free as possible from manmade interference. Although the interference is low at this site at meter wavelengths the ionosphere becomes a major concern with its ability to cause wavefront distortion ([Swarup et al., 1991](#)).

5.4 Radio data

In this chapter I study the Far-Infrared - Radio Correlation in The European Large-Area *ISO* Survey-North 1 field (ELAIS-N1). Although there have been numerous observations

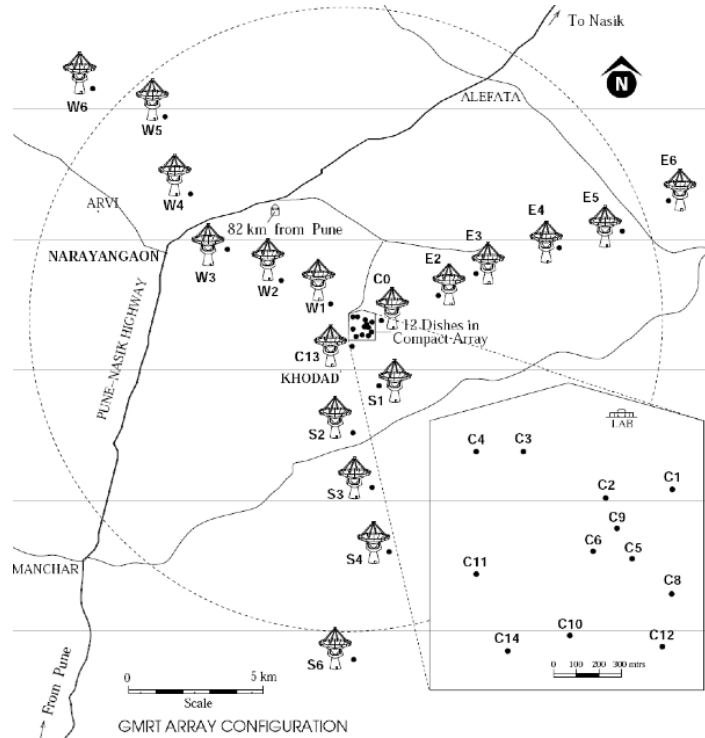


Figure 5.4: GMRT location 80 km north of Pune and 10 km east of Narayangaon, illustrating the configuration of the 30 antennae. The total collecting area of the 45 m dishes is ≈ 3 times the collecting area of the VLA. Fourteen of the dishes are randomly placed ‘randomly’ in the central 1 km core, the remaining dishes are placed in a Y configuration resulting in an interferometric baseline of 25 km. Image credit: Tata Institute of Fundamental Research.

of this field at infrared wavelengths including the European Large Area *ISO* Survey (Oliver et al., 2000), *Spitzer* (Lonsdale et al., 2003; Surace et al., 2004) and the UK Infrared Deep Sky (UKIDSS) (Lawrence et al., 2007) there have been relatively few at wavelengths longer than 20 cm. That gap is now being addressed by the GMRT.

ELAIS-N1 is a $\sim 9 \text{ deg}^2$ area centred on $\text{RA} = 16^{\text{d}}11^{\text{m}}20^{\text{s}}$, $\text{Dec} = +55^{\circ}00'00''$. The ELAIS-N1 field has also been included in major radio surveys at 1.4 GHz namely the VLA *NVSS* and *FIRST* surveys. In this chapter data I use data from the radio surveys in Table 5.1.

A 20 cm survey of the ELAIS-N1 field has been undertaken with the VLA in the C configuration where antennae are closely configured to 3.5 km. Previous shallower surveys the *NVSS* and *FIRST* had FWHM resolutions of 45 arcsec and 5 arcsec respectively. This deep 20 cm survey has a resolution of 15 arcsec. With an integration time of ≈ 60 min for

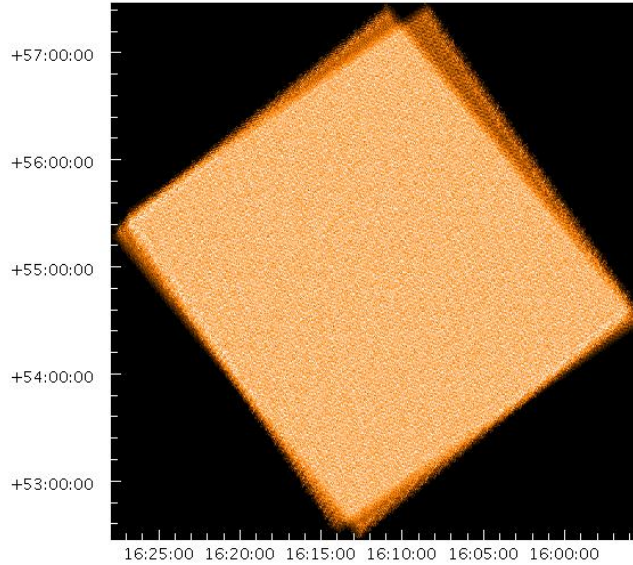


Figure 5.5: Coverage map of the ELAIS-N1 field illustrating the orientation of the scan relative to the co-ordinates

each pointing this survey reaches below the flux limit of both previous surveys and has a confusion limit between the two (Ciliegi et al., 1999). This survey overcomes the problem encountered in chapter 2 where a choice was made to supplement the *NVSS* data at $z > 0.2$ with *FIRST* data with the associated possibility of under sampling with the *FIRST* beam.

Table 5.1: Radio frequency coverage of the ELAIS-N1 field

Frequency	Area (deg ²)	Sources	Author / Reference
325 MHz	3.8	1286	Sirothia et al. (2009) MNRAS.395.269
610 MHz	9	2500	Garn et al. (2008) MNRAS.383.75G
1400 MHz	1.54	964	Ciliegi et al. (1999) MNRAS.302.222

GMRT data

In this chapter I use two dedicated low radio frequency observations of the ELAIS-N1 field undertaken with the GMRT. The first by Sirothia et al. (2009) was conducted at 325 MHz in June 2005, using 25 available antennas and observing over a time period of 20.6 hours a total of 1286 sources were extracted and catalogued.

The second series of observations from the GMRT was undertaken by Garn et al. (2008) at a frequency of 610 MHz and covering an area of 9 deg² with an observation time

totalling 25 hours during August 2003, resulting in a catalogue of 2500 sources.

Data from the VLA survey at 20 cm of the ELAIS N1 field (Ciliegi et al., 1999) was matched to the SWIRE Photometric catalogue (Lonsdale et al., 2003) and both the GMRT 325 MHz observations by Sirothia et al. (2009) and the 610 MHz observations by Garn (2008). All matches are made within a search radius of 20 arcsec. The resulting catalogues have respectively 46 sources at 325 MHz and 38 at 610 MHz and have $70 \mu\text{m}$ flux densities and redshifts in addition to the radio data. Final matches in each catalogue have separations < 7 arcsec.

I have estimated the false matching rate (FMR) for both the 325 and 610 MHz samples by applying a shift of 5 arcmin to the DEC co-ordinates and re-matching at the same radius. The FMR of the 325 MHz sample was found to be $\approx 15\%$ and the FMR of the 610 MHz sample was found to be zero.

5.5 Far-infrared data

The ELAIS-N1 field is well observed in the far-infrared with observations from the following space observatories:

- The European Large Area ISO Survey (ELAIS) with observations at 90 and $175 \mu\text{m}$ (Oliver et al., 2000).
- The SIRTf Wide-Area Infrared Extragalactic Survey (SWIRE) observed ELAIS-N1 with the Multiband Imaging Photometer (MIPS) at 24, 70, and $160 \mu\text{m}$ (Lonsdale et al., 2003).
- *Herschel* observed ELAIS-N1 with the SPIRE photometer at 250, 350 and $500 \mu\text{m}$ (Oliver et al., 2012; Griffin et al., 2010)

In this chapter I use *Herschel* HerMES data from the ELAIS-N1 field with a coverage of 3.25 deg^2 . The instrument of interest is the submillimeter camera and spectrometer, (SPIRE) Spectral and Photometric Imaging REceiver, working in three spectral bands of 250, 350 and $500 \mu\text{m}$.

Redshifts are taken from the revised SWIRE photometric redshift catalogue which covers an 8.72 deg^2 area of ELAIS-N1 together with seven other fields (Rowan-Robinson et al., 2008). The ELAISN1 section of this catalogue is comprised of 204421 sources of which $\approx 5\%$ are also complete with spectroscopic redshifts.

Data sets were matched as follows: 1284 observations at 325 MHz [Sirothia et al. \(2009\)](#), matched to the SWIRE photometric redshift catalogue within a radius of 20 arcsec with 1284 matches, then matching this sample to the L5-ELAIS-N1-HerMES-xID250-DR2 ([Oliver et al., 2012](#)) sample within a radius of 20 arcsec. Similarly 2500 observations at 610 MHz ([Garn, 2008](#)) matched to the SWIRE photometric redshift catalogue within a radius of 20 arcsec, then matched to the L5-ELAIS-N1-HerMES-xID250-DR2 sample within a radius of 20 arcsec. Selecting only galaxies with complete coverage in the 250, 350 and 500 μm SPIRE wavebands gives a total of 203 galaxies in the 325 MHz set and 94 galaxies in the 610 MHz set.

5.6 Method and results

In this section I compare the FIRC of two samples of galaxies from the ELAIS-N1 field observed at both 325 MHz and 610 MHz. Initially I calculate q_{L70} with 70 μm SWIRE flux densities using Equation 2.1 with radio flux densities as divisors at the GMRT frequencies of 325 and 610 MHz. I obtain corresponding q_{70} values (at 325 MHz) of 1.73 ± 0.07 and 1.95 ± 0.09 (at 610 MHz). For comparison I show that q_{70} (at 1.4 GHz) is 2.28 ± 0.08 and 2.17 ± 0.1 respectively. These q values are quoted without any cuts or k -correction and serve to illustrate the differential between the q ratios of the 1.4 GHz sample against the lower frequency GMRT samples. See plots in Figures 5.6 and 5.7.

I next calculate q_{LTIR} for both samples. The IDL program CMCIREN.PRO by [Casey \(2012\)](#) is used to calculate $LTIR$ and the rest-frame radio luminosities for each wavelength are calculated with Equation 2.10 and spectral index α set at -0.6. Finally using Equation 3.4 the q_{LTIR} was calculated at 325 MHz and 610 MHz.

The mean q_{LTIR} for the 325 MHz selected sample is

$$q_{LTIR} = 2.02 \pm 0.04 (\sigma = 0.45)$$

the mean q_{LTIR} for the 610 MHz selected sample is

$$q_{LTIR} = 2.34 \pm 0.05 (\sigma = 0.38)$$

Both mean qs are reported after applying a cut below $q=1.4$. Figures 5.8 and 5.9 are plots of the FIRC for the 325 MHz and 610 MHz selected samples respectively. Tables 5.2 and 5.3 have tabulated qs for a set of redshift slices covering the most resolved areas.

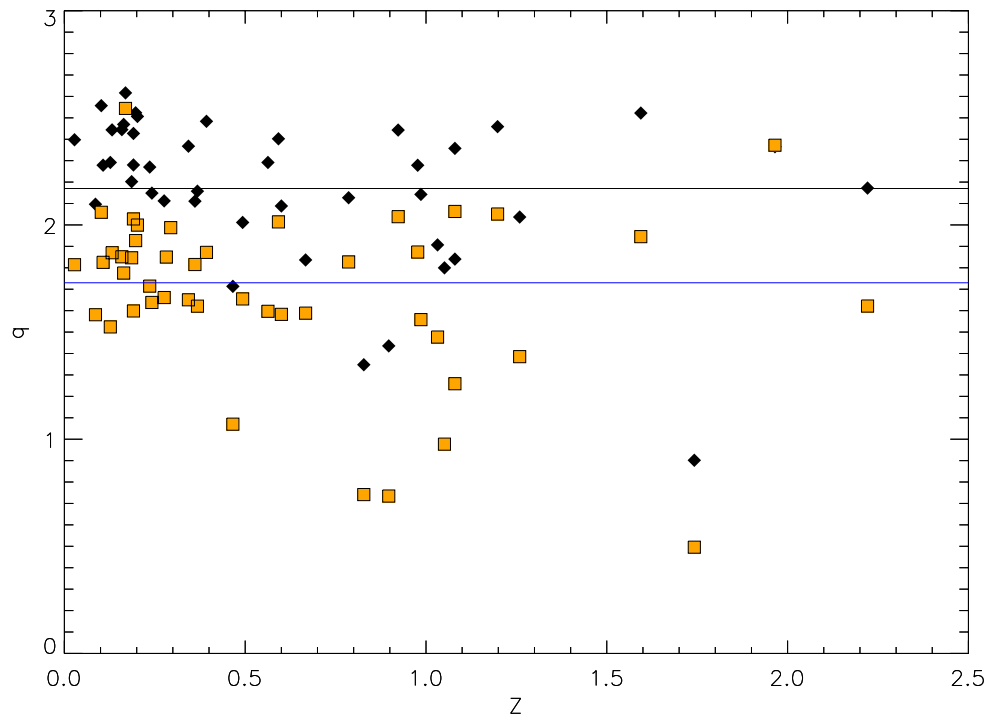


Figure 5.6: q_{L70} of the 325 MHz selected sample (orange squares) with a mean q_{70} of 1.73 ± 0.07 indicated by the continuous blue line is compared to q_{70} at a frequency of 1.4 GHz (black diamonds) where $q_{70}=2.28 \pm 0.08$ with the mean indicated by the continuous black line

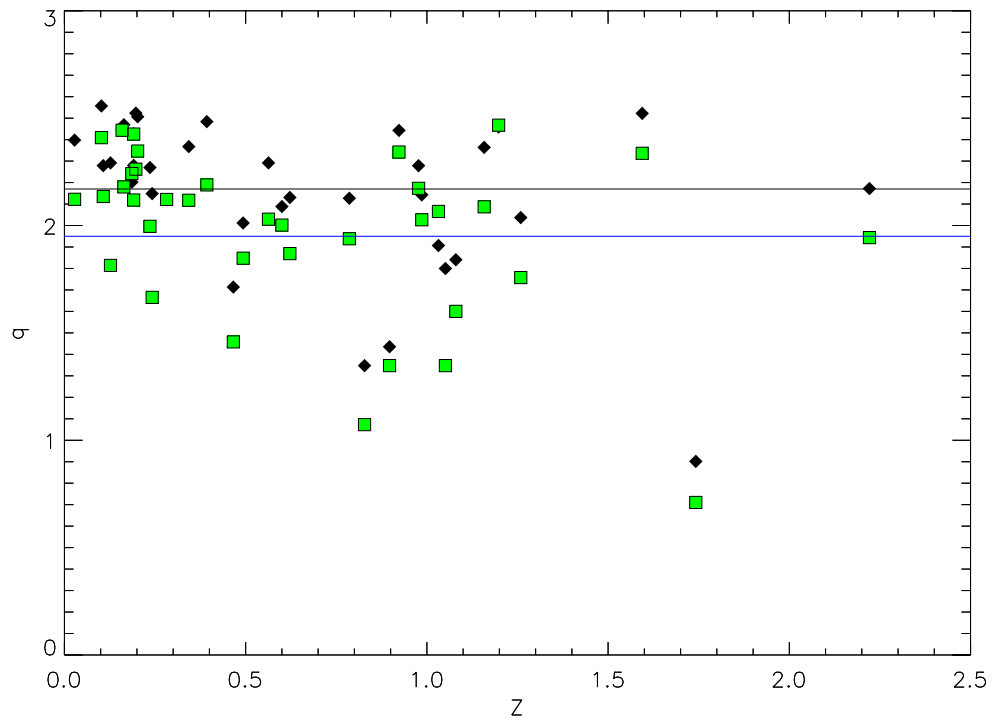


Figure 5.7: q_{L70} of the 610 MHz selected sample (green squares) with a mean q_{70} of 1.95 ± 0.09 indicated by the continuous blue line is compared to q_{70} at a frequency of 1.4 GHz (black diamonds) where $q_{70}=2.17 \pm 0.10$ with the mean indicated by the continuous black line

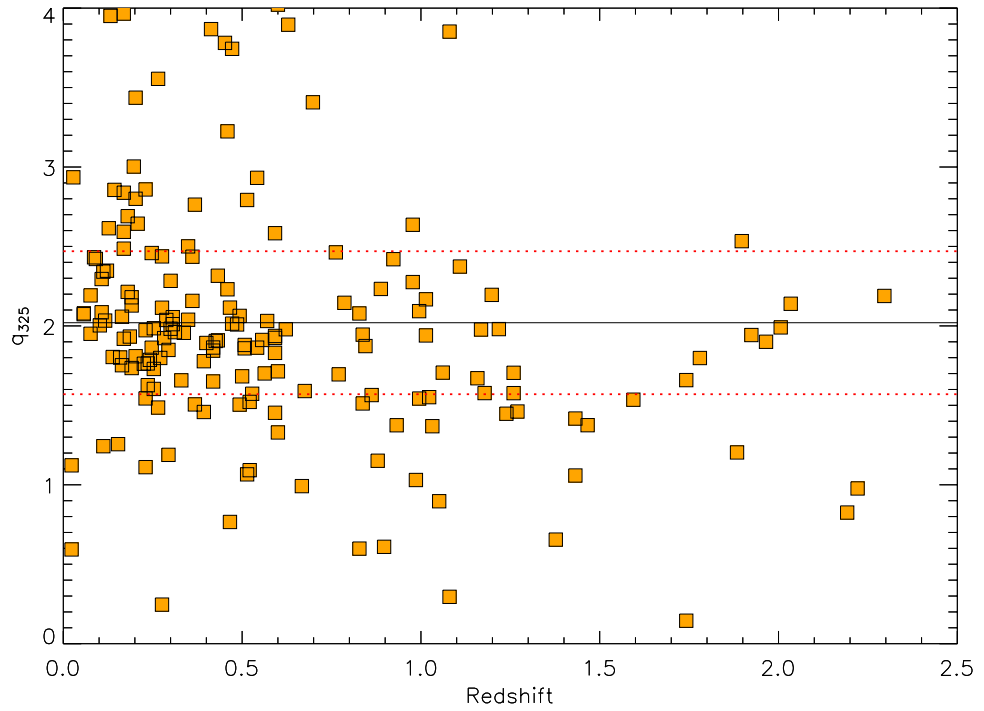


Figure 5.8: q_{LTIR} of the 325 MHz selected sample. The mean q_{LTIR} of 2.02 ± 0.04 with a dispersion of 0.45 is indicated by the continuous black line. The two dashed (red) lines represent the $\pm 1\sigma$ q_{LTIR} . The mean q_{LTIR} for redshift slices are listed in table 5.2

Table 5.2: q_{LTIR} (325 MHz) Redshift slices, see figure 5.8

N_{Total}	z range	q_{Ltir}	σ
45	$0 < z < 0.25$	2.19 ± 0.07	0.47
40	$0.25 < z < 0.5$	2.04 ± 0.06	0.42
20	$0.5 < z < 0.75$	1.99 ± 0.12	0.53
15	$0.75 < z < 1.0$	1.99 ± 0.10	0.38
12	$1.0 < z < 1.25$	1.83 ± 0.10	0.32
5	$1.25 < z < 1.5$	1.51 ± 0.06	0.13
2	$1.5 < z < 1.75$	1.59 ± 0.06	0.09
5	$1.75 < z < 2.0$	1.87 ± 0.21	0.47

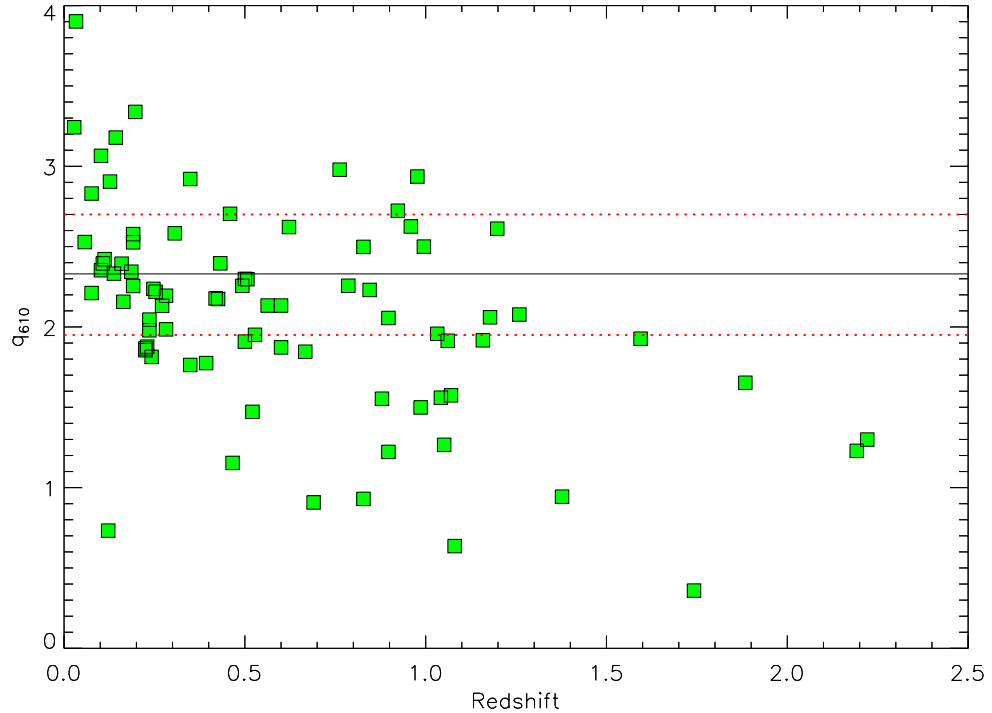


Figure 5.9: q_{LTIR} of the 610 MHz selected sample. The mean q_{LTIR} of 2.34 ± 0.05 with a dispersion of 0.38 is indicated by the continuous black line. The two dashed (red) lines are the $\pm 1\sigma$ q_{LTIR} . The mean q_{LTIR} for redshift slices are listed in table 5.3

As discussed in Section 4.2.3 it is important to k -correct the radio flux density for each galaxy. For the 610 MHz selected sample I have compiled a subset of galaxies complete with additional 1.4 GHz data. This affords the opportunity to derive an individual spectral index for each galaxy, and is accomplished using Equation 2.8. Figure 5.10 plots q_{LTIR} for the sample initially with a fixed spectral index (Si) of $\alpha = -0.6$ as used in the original larger sample, here plotted as blue squares. For this small sample the mean q_{LTIR} is raised to 2.39 ± 0.08 compared to a mean of 2.34 ± 0.05 in the original sample. Applying an individual spectral index in the calculation of the radio luminosity and then subsequently calculating q_{LTIR} , we find that the majority of qs are revised to a higher ratio with only a few going lower. The new values are plotted as red diamonds, with a new mean q_{LTIR} plotted as a continuous black line at 2.46 ± 0.08 .

Table 5.3: q_{LTIR} (610 MHz) Redshift slices, see figure 5.9

N_{Total}	z range	q_{Ltir}	σ
25	$0 < z < 0.25$	2.43 ± 0.08	0.44
11	$0.25 < z < 0.5$	2.34 ± 0.08	0.28
7	$0.5 < z < 0.75$	2.12 ± 0.10	0.27
9	$0.75 < z < 1.0$	2.53 ± 0.10	0.31
5	$1.0 < z < 1.25$	2.09 ± 0.13	0.29

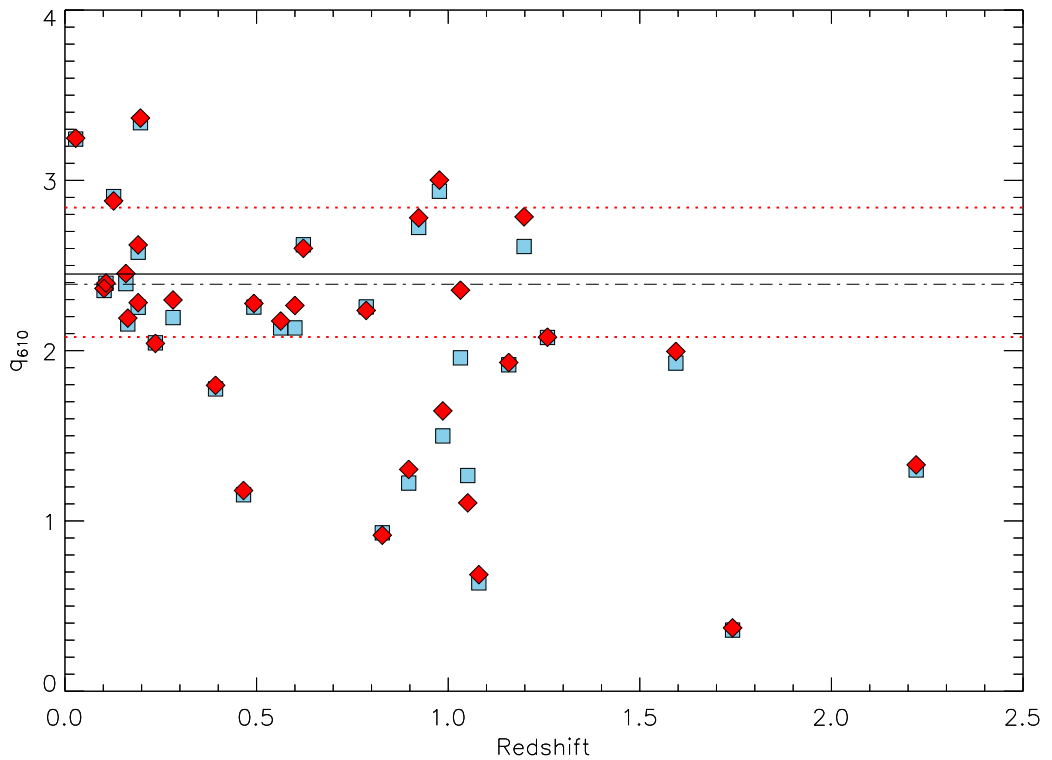


Figure 5.10: Subset of the 610 MHz selected sample shown in Figure 5.9. Individual spectral indices have been calculated for each galaxy. q_{LTIR} for the original sample is calculated with a fixed spectral index (S_i) $\alpha = -0.6$, represented by the blue squares and has a mean $q_{\text{LTIR}} = 2.39 \pm 0.08$ with a dispersion of 0.39. The mean q_{LTIR} of the sample with fixed S_i is indicated by the dot-dash black line. q_{LTIR} calculated with individual spectral indices is depicted by red diamonds, The mean q_{LTIR} of this sample is raised to 2.46 ± 0.08 with a dispersion of 0.38 and is indicated by the black line. The two dashed red lines are the $\pm 1\sigma$ q_{LTIR} of the sample calculated with individual spectral indices.

5.7 Discussion

In this chapter I have built two samples of star-forming galaxies in the northern SWIRE field of ELAIS-N1, using observations from the *Spitzer* SWIRE survey at $70\ \mu\text{m}$ and the *Herschel* HerMES survey at 250, 350 and $500\ \mu\text{m}$. The radio data at 1.4 GHz is from the ISO ELAIS 20cm VLA survey by Ciliegi et al. (1999) and the radio data at 325 MHz by Sirothia et al. (2009) and at 610 MHz by Garn (2008). The redshifts of the radio samples at 325 and 610 MHz observed with the GMRT both cover a greater range ($z > 2.0$) than discussed in previous chapters.

I have calculated the ratio q_{LTIR} for both the 325 and 610 MHz samples. The mean q values are found to be lower than recorded previously at 1.4 GHz. In both samples we see a high proportion of radio loud objects. Above a redshift $z \sim 1$ there is seen to be an apparent scarcity of galaxies nearer to the mean q . This is attributed to selection effects whereby the galaxies strongest in the radio, AGN and QSOs are dominating.

I demonstrated in chapter 2 that the FIRC does not evolve to a redshift of $z \sim 0.5$. From the plots in this chapter (Figures 5.8 and 5.9) I show that within the $\pm 1\sigma$ lines that there is no detectable indication of evolution to a redshift of $z \sim 1$.

The ability to k -correct the radio by using a spectral index derived from two frequencies will give a more accurate result than that derived from a single generic index. At low radio frequencies an individual spectral index is important since it is in this region the synchrotron spectra is starting to deviate from the predictable power law at frequencies $> 1.4\ \text{GHz}$. At some low radio frequency synchrotron absorption is predicted to manifest as a decrease in the received flux. Observation of the radio flux at low frequency is expected to reveal the spectrum flattening (Emerson, 1996).

Chapter 6

Conclusions

At the present time the enigma of the FIRC continues to present us with a conundrum: why does this phenomena, which relies on disparate processes, appear to be so constant across a range of star-forming galaxies that have a wide distribution in their individual luminosities of over five (log) decades. Natural variation in the interstellar medium (ISM) would lead us to predict a deviation, evolution or breakdown at some as yet undetermined redshift or luminosity.

Looking more closely at the ISM we can examine some of the processes at the heart of this problem. The far-infrared radiation is the product of starlight ¹ from massive stars being reprocessed by dust. This immediately leads to a question, are all dust grains the same size, material and density? A diversion in any of these properties would lead to a dispersion in the strength of the far-infrared radiation which is again determined by the population and distribution of the stars themselves. The radio emission is attributed to a by-product of the endpoint in the lives of massive stars: stars of mass $8M_{\odot}$ undergo an inevitable core-collapse when the fuel is exhausted. These events are linked to the production of synchrotron radiation via the process of accelerating cosmic ray particles in the resultant shocks. The supernovae rate (SNR) is another variable that can be added to our list, whereby the SNR is expected to follow the same evolutionary path as the star formation rate (SFR) (Horiuchi et al., 2011). It would be very surprising if the conditions in the ISM, including the magnetic field implied in the production of synchrotron radiation, were so balanced that the FIRC could stay so constant.

In this thesis I have shown that the FIRC does not appear to evolve with luminosity or redshift to $z \sim 1$. As can be seen from these results, whichever way I analyse the

¹More than fifty percent of the UV-optical output of stars is removed by the presence of dust (Calzetti, 2001)

FIRC using GHz or MHz radio frequencies or probing different parts of the SED the findings confirm the universal relationship of the Far-Infrared/Radio Correlation. There is a strong indication therefore that star formation obeys the same pattern no matter what the conditions are.

Galaxies that exhibit different dust temperatures, on the average, are probing differences in the interstellar medium. I have tested the FIRC by building a sample of 725 objects with peak dust temperatures allocated by fitting to a modified black body SED and mid-infrared power law (Casey, 2012). An unexpected result is the apparent reduction in the mean q_{LTIR} towards higher peak dust temperatures. This result warrants a closer look with a larger sample.

Table 6.1 shows the relation between q_{LTIR} for the four data sets examined in the previous chapters. The q_{LTIR} ratio is seen to reduce as the observed radio frequency is lowered and correspondingly the synchrotron spectrum rises. Thus I conclude that radio emissions at frequencies down to 74 MHz are all viable to calculate q ratios. At MHz frequencies there is an increasing chance of encountering galaxies with a particularly low spectral index, i.e. deviating significantly from the expected synchrotron spectra. The dispersion seen in the q ratio at 1.4 GHz and 74 MHz in my samples is comparable. The dispersion seen in the GMRT samples is greater than either the 1.4 GHz or 74 MHz, however these two small samples have a high number of radio loud galaxies and are deficient in starburst galaxies at redshifts $> z = 1.0$. Hence from these samples it is not entirely clear that the dispersions in the FIRC across the radio frequency range are comparable, although this is thought to be likely with larger samples.

Given the luminosity temperature relation for infrared galaxies (Frenk et al., 1990), how is it possible that the the q ratios shown in Figures 3.7 and 3.8 show a dependance on temperature and not luminosity? One possible explanation is that as the temperature rises the proportion of AGN goes up. This has a bigger impact on the radio power than on the infrared power. This indicates that at higher temperatures the infrared may be a better measure of star formation than the radio power.

Is it possible to exploit the spectral classification of galaxies in the *IIFSCz* catalogue in the determination of their q ratio? In Chapter 2, Table 2.9 I list spectral types from Elliptical through to QSO. Apart from a small number galaxies classified as QSOs which are seen to exhibit a lower q_{L60} , the remainder show very little deviation from the overall mean $q_{L60} = 2.63 \pm 0.01$. Figure 2.7 shows populations of QSOs that follow the FIRC and QSOs that lie away from the mean. So within QSOs for example spectral type

Freq. (MHz)	λ (m)	Sensitivity			
		Superterp (mJy)	NL Core (mJy)	Full NL (mJy)	Full EU (mJy)
15	20.0
30	10.0	36	9.0	5.7	3.8
45	6.67	29	7.4	4.7	3.1
60	5.00	25	6.2	3.9	2.6
75	4.00	44	10.8	6.8	4.5
120	2.50	1.5	0.38	0.30	0.20
150	2.00	1.3	0.31	0.24	0.16
180	1.67	1.5	0.38	0.30	0.20
200	1.50	(2.5)	(0.62)	(0.48)	(0.32)
210	1.43	(2.5)	(0.62)	(0.48)	(0.32)
240	1.25	(5.6)	(1.4)	(1.1)	(0.73)

Figure 6.1: LOFAR sensitivities. The different columns refer to the case of a 6-station Superterp, a 24-station core array, a 40-station Dutch array, and a 48-station full array. Credit: Astron

does not appear to predict their q ratio. Figure 2.8 is a colour coded plot of q_{FIR} for galaxies classified from Elliptical through spirals to QSOs, I find no discernible pattern and conclude overall that spectral type is not a strong factor in the q ratio of galaxies.

I have shown that the use of individual spectral indices leads to an improvement in the k -correction of the radio power of galaxies. By using radio observations at two (or more) frequencies it becomes possible to correct the raw radio power measurement leading to a more robust calculation of the q ratios.

Table 6.1: q_{TIR} at frequencies of 1.4 GHz to 74 MHz

N_{Total}	q_{TIR}	σ	FIR (μm)	Radio (MHz)
7071	2.72 ± 0.01	0.24	- 60 100 -	1400
725	2.65 ± 0.01	0.24	- 60 100 140	1400
94	2.34 ± 0.05	0.38	- 250 350 500	610
203	2.02 ± 0.04	0.45	- 250 350 500	325
95	1.75 ± 0.02	0.20	25 60 100 140	74

6.1 Future work

With LOFAR data just arriving a new opportunity for valuable work on this topic is opened up for testing the Far-infrared/ radio correlation to higher redshifts. The first all-sky survey undertaken with LOFAR is the Multifrequency Snapshot Sky Survey (MSSS). This is a shallow commissioning first survey covering the frequency bands of 30-74 and 120-160 MHz and is due for public release mid - 2014. Data from this survey can be employed to further explore the behaviour of the correlation in a region of the radio spectrum where synchrotron may be declining in strength.

Examination of the LOFAR sensitivities in Fig. 6.1 indicates a minimum x10 increase in sensitivity at 75 MHz compared to the VLSS at 74 MHz. LOFAR will detect steep spectra sources at high redshift, an object at redshift 3 detected at 150 MHz would have a rest frame frequency of 600 MHz where synchrotron losses are not having a significant effect. Lower radio frequencies lead to increased sensitivity to high redshift objects, building a larger sample than possible with 1.4 GHz observations (Kassim et al., 2002). When these sources are matched to *Herschel* SPIRE sources this will enable the study of the FIRC to high redshift with surveys dominated by star-forming galaxies at at greater depths than detected by the VLA NVSS (Snellen et al., 2009).

Bibliography

Abazajian K. N., et al., 2009, ApJS, 182, 543 [22](#)

Ananthakrishnan S., 2005, International Cosmic Ray Conference, 10, 125 [81](#)

Appleton P. N., et al., 2004, ApJS, 154, 147 [23](#)

Astron, 2013, Introduction to LOFAR MSSS. <http://www.astron.nl/radio-observatory/lofar-msss/lofar-msss> [70](#)

Beal B., 2010, A Macro for Calculating Summary Statistics on Left Censored Environmental Data using the Kaplan-Meier Method. <http://analytics.ncsu.edu/sesug/2010/SDA09.Beal.pdf> [30](#)

Becker R. H., White R. L., Helfand D. J., 1995, ApJ, 450, 559 [9](#), [22](#)

Beelen A., 2004, PhD thesis, Institut d'Astrophysique Spatiale [4](#)

Beichman C. A., Neugebauer G., Habing H. J., Clegg P. E., Chester T. J., eds., 1988, Infrared astronomical satellite (IRAS) catalogs and atlases. Volume 1: Explanatory supplement, Vol. 1. NASA [6](#)

Bell E. F., 2003, ApJ, 586, 794 [2](#), [13](#), [15](#), [50](#)

Bertout C., 2010, A&A, 514, 1 [7](#)

Bianchi S., Davies J. I., Alton P. B., 1999, A&P, 344, L1 [54](#)

Blain A., Combes F., Draine B., 2002, The Cold Universe. Springer [14](#), [55](#)

Bourne N., Dunne L., Ivison R. J., Maddox S. J., Dickinson M., Frayer D. T., 2011, MNRAS, 410, 1155 [1](#), [10](#), [14](#), [16](#), [50](#)

Burke B. F., Graham-Smith F. G., 2002, An Introduction to Radio Astronomy. Cambridge [11](#)

-
- Butt Y., 2009, *Nature*, 460, 701 [4](#)
- Calzetti D., 2001, *PASP*, 113, 1449 [92](#)
- Cameron R. M., 1976, *Sky & Telescope*, 52, 327 [9](#)
- Carilli C. L., Yun M. S., 1999, *ApJ*, 513, L13 [17](#)
- Casey C. M., 2012, *MNRAS*, 425, 3094 [28](#), [44](#), [50](#), [55](#), [56](#), [57](#), [74](#), [85](#), [93](#)
- Cesarsky C. J., Salama A., 2006, *ISO Science Legacy*. Springer [6](#)
- Chandra P., Ray A., Bhatnagar S., 2004, *ApJ*, 604, L97 [12](#)
- Chary R., Elbaz D., 2001, *ApJ*, 556, 562 [28](#)
- Ciliegi P., et al., 1999, *MNRAS*, 302, 222 [83](#), [84](#), [91](#)
- Clark B. G., Kassim N. E., Perez M. R., 2005, in *Astronomical Society of the Pacific Conference Series*, Vol. 345, *From Clark Lake to the Long Wavelength Array: Bill Erickson's Radio Science*, Kassim N., Perez M., Junor W., Henning P., eds., p. 533 [68](#)
- Cohen A. S., Lane W. M., Cotton W. D., Kassim N. E., Lazio T. J. W., Perley R. A., Condon J. J., Erickson W. C., 2006, *VizieR Online Data Catalog*, 8079, [9](#), [26](#), [67](#), [69](#), [71](#)
- Condon J. J., 1992, *ARA&A*, 30, 575 [9](#), [10](#), [11](#), [12](#), [27](#), [33](#)
- , 1998, *Radio Sources and Cosmology*. Springer [29](#)
- Condon J. J., Anderson M. L., Helou G., 1991, *ApJ*, 376, 95 [20](#)
- Condon J. J., Cotton W. D., Broderick J. J., 2002, *AJ*, 124, 675 [29](#), [31](#), [45](#), [56](#)
- Condon J. J., Cotton W. D., Greisen E. W., Yin Q. F., Perley R. A., Taylor G. B., Broderick J. J., 1998, *AJ*, 115, 1693 [9](#), [22](#), [23](#), [69](#)
- Cox M. J., Eales S. A. E., Alexander P., Fitt A. J., 1988, *MNRAS*, 235, 1227 [24](#), [68](#), [69](#), [78](#)
- Cox P., Kruegel E., Mezger P. G., 1986, *A&A*, 155, 380 [11](#)
- Dale D. A., Helou G., 2002, *ApJ*, 576, 159 [28](#)
- Davies R. D., Wilkinson A., 1998, *ArXiv Astrophysics e-prints* [12](#)

-
- de Bruyn A. G., et al., 2002, Exploring the Universe with the Low Frequency Array: A Scientific Case. <http://www.nova-astronomy.nl/lofarsciencecase.pdf> 71
- de Bruyn G., et al., 2000, VizieR Online Data Catalog, 8062, 0 67
- de Graauw T., et al., 2010, A&A, 518, L6 7
- de Jong T., Clegg P. E., Rowan-Robinson M., Soifer B. T., Habing H. J., Houck J. R., Aumann H. H., Raimond E., 1984, ApJ, 278, L67 1
- de Jong T., Klein U., Wielebinski R., Wunderlich E., 1985, A&A, 147, L5 10
- Dempsey J. T., et al., 2012, Society of Photo-Optical Instrumentation Engineers (SPIE) Conference Series, 8452 79
- Desert F. X., Boulanger F., Puget J. L., 1990, A&A, 237, 215 2
- Devereux N. A., Eales S. A., 1989, ApJ, 340, 708 20
- Dole H., et al., 2006, A&A, 451, 417 2, 3
- Donley J. L., Rieke G. H., Rigby J. R., Pérez-González P. G., 2005, ApJ, 634, 169 16
- Douglas J. N., Bash F. N., Bozayan F. A., Torrence G. W., Wolfe C., 1996, AJ, 111, 1945 26
- Dunne L., Eales S. A., 2001, MNRAS, 327, 697 55
- Duric N., Bourneuf E., Gregory P. C., 1988, AJ, 96, 81 5
- Emerson D., 1996, Interpreting Astronomical Spectra. John Wiley and Sons Ltd 91
- Emerson J. P., Habing H. J., Clegg P. E., Lundy S., 1985, The IRAS mission. NASA 22
- Falcke H., 2006, Highlights of Astronomy. Volume 13. IAU 9, 67
- Feigelson E. D., Nelson P. I., 1985, ApJ, 293, 192 30
- Fitt A. J., Alexander P., Cox M. J., 1988, MNRAS, 233, 907 24
- Frenk C. S., White S. D. M., Efstathiou G., Davis M., 1990, ApJ, 351, 10 93
- Fukugita M., Nakamura O., Turner E. L., Helmboldt J., Nichol R. C., 2004, APJ, 601, L127 45
- Fullmer L., Lonsdale C. J., 1989, JPL D-1932, Version 2, 0 24

-
- Funk S., Ackermann M., Ajello M., 2013, *Science*, 339, 807 [4](#)
- Garn T., Alexander P., 2008, *MNRAS*, 391, 1000 [70](#)
- , 2009, *MNRAS*, 394, 105 [70](#)
- Garn T., Green D. A., Riley J. M., Alexander P., 2008, *MNRAS*, 383, 75 [83](#)
- Garn T. S., 2008, PhD thesis, Cambridge University [52](#), [84](#), [85](#), [91](#)
- Garrett M. A., 2002, *A&A*, 384, L19 [14](#)
- Ghisellini G., Celotti A., Tavecchio F., Haardt F., Sbarbato T., 2013, ArXiv e-prints [20](#)
- Gillespie Jr. C. M., 1981, in *Society of Photo-Optical Instrumentation Engineers (SPIE) Conference Series*, Jerkovsky W., ed., Vol. 265, pp. 1–7 [5](#)
- Goudfrooij P., 1997, in *Astronomical Society of the Pacific Conference Series*, Vol. 116, *The Nature of Elliptical Galaxies; 2nd Stromlo Symposium*, Arnaboldi M., Da Costa G. S., Saha P., eds., p. 338 [29](#)
- Griffin M. J., et al., 2010, *A&A*, 518, L3 [7](#), [84](#)
- Haarsma D. B., Partridge R. B., Windhorst R. A., Richards E. A., 2000, *ApJ*, 544, 641 [17](#)
- Hales S. E. G., Mayer C. J., Warner P. J., Baldwin J. E., 1991, *MNRAS*, 251, 46 [26](#)
- Hales S. E. G., Waldram E. M., Rees N., Warner P. J., 1994, *VizieR Online Data Catalog*, 8031, 0 [26](#)
- Hawkins E., Maddox S., Branchini E., Saunders W., 2001, *MNRAS*, 325, 589 [55](#)
- Heckman T., 2006, *Starburst Galaxies*, *Encyclopedia of Astronomy and Astrophysics*. IOP [6](#)
- Helou G., Bica M. D., 1993, *ApJ*, 415, 93 [12](#), [15](#)
- Helou G., Ryter C., Soifer B. T., 1991, *ApJ*, 376, 505 [54](#)
- Helou G., Soifer B. T., Rowan-Robinson M., 1985, *ApJ*, 298, L7 [1](#), [10](#), [19](#), [20](#), [23](#), [24](#), [26](#), [33](#), [39](#), [44](#), [50](#)
- Helou G., Walker D. W., 1988, *Infrared astronomical satellite (IRAS) catalogs and atlases*. Volumes 2 to 6. NASA [69](#)

-
- Hoernes P., Berkhuijsen E. M., Xu C., 1998, *A&A*, 334, 57 [13](#), [15](#)
- Hogg D. W., Baldry I. K., Blanton M. R., Eisenstein D. J., 2002, *ArXiv:astro-ph/0210394* [27](#)
- Horiuchi S., Beacom J. F., Kochanek C. S., Prieto J. L., Stanek K. Z., Thompson T. A., 2011, *ApJ*, 738, 154 [92](#)
- Hubble E. P., 1925, *Popular Astronomy*, 33, 252 [2](#)
- Hummel E., 1991, *A&A*, 251, 442 [1](#), [70](#), [78](#)
- Ibar E., 2008a, PhD thesis, Institute for Astronomy School of Physics and Astronomy. University of Edinburgh [28](#)
- Ibar E., et al., 2008, *MNRAS*, 386, 953 [14](#)
- Israel F. P., Mahoney M. J., 1990, *ApJ*, 352, 30 [70](#)
- Israel F. P., Mahoney M. J., Howarth N., 1992, *A&A*, 261, 47 [68](#), [78](#)
- Iverson R. J., et al., 2010, *A&A*, 518, L31 [1](#), [10](#), [16](#), [50](#)
- Jarvis M. J., et al., 2010, *MNRAS*, 409, 92 [1](#), [10](#), [16](#), [22](#), [50](#)
- Kant I., 1755, *Universal Natural History and Theory of Heaven*. - [2](#)
- Kassim N. E., Lazio T. J. W., Erickson W. C., Crane P. C., Perley R. A., Hicks B., 2002, in *IAU Symposium, Vol. 199, The Universe at Low Radio Frequencies*, Pramesh Rao A., Swarup G., Gopal-Krishna, eds., p. 474 [96](#)
- Kassim N. E., et al., 2005, in *Astronomical Society of the Pacific Conference Series, Vol. 345, From Clark Lake to the Long Wavelength Array: Bill Erickson's Radio Science*, Kassim N., Perez M., Junor W., Henning P., eds., p. 392 [67](#)
- Kessler M. F., et al., 1996, *A&A*, 315, L27 [6](#), [79](#)
- Kimball A. E., Ivezić Ž., 2008, *ApJ*, 136, 684 [10](#)
- Lacki B. C., 2013, *MNRAS*, 431, 3003 [71](#)
- Lacki B. C., Thompson T. A., Quataert E., 2010, *ApJ*, 717, 1 [13](#), [14](#), [15](#)
- Lagache G., Dole H., Puget J.-L., 2003, *MNRAS*, 338, 555 [28](#)

-
- Lane W. M., Cotton W. D., Helmboldt J. F., Kassim N. E., 2012, *Radio Science*, 47 [v](#), [69](#), [70](#), [71](#)
- Langer W. D., Wilson R. W., Goldsmith P. F., Beichman C. A., 1989, *ApJ*, 337, 355 [54](#)
- Lawrence A., et al., 2007, *MNRAS*, 379, 1599 [82](#)
- Levenson L., et al., 2010, *MNRAS*, 409, 83 [20](#)
- Lisenfeld U., Völk H. J., 2000, *A&A*, 354, 423 [4](#)
- Longair M., 1994, *High Energy Astrophysics. Volume 2. Stars ,the Galaxy and the interstellar medium.* CUP [12](#)
- , 1998, *Galaxy Formation.* Springer [6](#)
- , 2006, *The Cosmic Century.* CUP [5](#)
- Lonsdale C. J., et al., 2003, *PASP*, 115, 897 [82](#), [84](#)
- Magdis G. E., et al., 2012, *ApJ*, 760, 6 [28](#)
- Mao M. Y., Huynh M. T., Norris R. P., Dickinson M., Frayer D., Helou G., Monkiewicz J. A., 2011, *ApJ*, 731, 79 [16](#), [17](#), [50](#)
- Martin P., 1978, *Cosmic Dust.* Clarendon Press Oxford [11](#)
- Matsuhara H., Wada T., Matsuura S., Nakagawa T., Pearson C. P., Kawada M., Shibai H., 2008, in *Astronomical Society of the Pacific Conference Series, Vol. 381, Infrared Diagnostics of Galaxy Evolution*, Chary R.-R., Teplitz H. I., Sheth K., eds., p. 507 [7](#)
- Miller N. A., Owen F. N., 2001, *AJ*, 121, 1903 [1](#)
- Morić I., Smolčić V., Kimball A., Riechers D. A., Ivezić Ž., Scoville N., 2010, *ApJ*, 724, 779 [10](#), [16](#)
- Moshir M., Kopman G., Conrow T. A. O., 1992, *IRAS Faint Source Survey, Explanatory supplement version 2.* CIT [6](#), [31](#)
- Murphy E. J., Kenney J. D. P., Helou G., Chung A., Howell J. H., 2009, in *The Evolving ISM in the Milky Way and Nearby Galaxies* [14](#)
- Mushotzky R., 2004, in *Astrophysics and Space Science Library, Vol. 308, Supermassive Black Holes in the Distant Universe*, Barger A. J., ed., p. 53 [31](#)

- Nagata H., Shibai H., Takeuchi T. T., Onaka T., 2002, PASJ, 54, 695 24
- Neugebauer G., et al., 1984, AJL, 278, L1 iv
- Neugebauer G., Leighton R. B., 1968, Scientific American, 219, 50 5
- Niklas S., Beck R., 1997, A&A, 320, 54 13, 15
- NRAO, 2013, The VLA Low-Frequency Sky Survey Redux. <http://www.cv.nrao.edu/vlss/VLSSpostage.shtml> 70
- Ochsenbeim F., Bauer P., Marcout J., 2000, A&AS, 143, 23 v
- O'Dea C. P., 1998, PASP, 110, 493 71
- Oliver S., et al., 2000, MNRAS, 316, 749 79, 82, 84
- Oliver S. J., et al., 2012, MNRAS, 424, 1614 7, 8, 55, 84, 85
- Oort J. H., van de Hulst H. C., 1946, BAIN, 10, 187 11
- Oyabu S., et al., 2005, AJ, 130, 2019 16
- Parker N. D., 1991, MNRAS, 251, 63 54
- Pierini D., Popescu C. C., Tuffs R. J., Völk H. J., 2003, A&A, 409, 907 52, 57, 58
- Pilbratt G. L., et al., 2010, A&A, 518, L1 7, 8
- Poglitsch A., et al., 2010, A&A, 518, L2 7
- Popescu C. C., Tuffs R. J., Völk H. J., Pierini D., Madore B. F., 2002, ApJ, 567, 221 66
- Rees N., 1990, MNRAS, 244, 233 9
- Rickard L. J., Harvey P. M., 1984, AJ, 89, 1520 9
- Rowan-Robinson M., et al., 2008, VizieR Online Data Catalog, 738, 60697 34, 45, 75, 84
- Rowan-Robinson M., Crawford J., 1989, MNRAS, 238, 523 51, 55
- Sanders D. B., Mirabel I. F., 1996, ARA&A, 34, 749 19, 24
- Sanders D. B., Soifer B. T., Elias J. H., Madore B. F., Matthews K., Neugebauer G., Scoville N. Z., 1988, ApJ, 325, 74 6
- Sargent M. T., et al., 2010a, ApJS, 186, 341 16, 50

-
- , 2010b, *ApJ*, 714, L190 1, 10, 16, 29, 50
- Saunders W., Rowan-Robinson M., Lawrence A., Efstathiou G., Kaiser N., Ellis R. S., Frenk C. S., 1990, *MNRAS*, 242, 318 55
- Schleicher D. R. G., Beck R., 2013, *A&A*, 556, A142 20
- Schnee S. L., 2006, PhD thesis, Harvard University 56
- Schnee S. L., Ridge N. A., Goodman A. A., Li J. G., 2005, *ApJ*, 634, 442 54
- Schweitzer M., et al., 2006, *ApJ*, 649, 79 46
- Seymour N., Huynh M., Dwelly T., Symeonidis M., Hopkins A., McHardy I. M., Page M. J., Rieke G., 2009, *MNRAS*, 398, 1573 1, 10, 14, 16, 50
- Siah M. J., Wiita P. J., 1990, *ApJ*, 363, 411 12
- Siebenmorgen R., Krügel E., 2007, *A&A*, 461, 445 25, 28
- Sirothia S. K., Dennefeld M., Saikia D. J., Dole H., Ricquebourg F., Roland J., 2009, *MNRAS*, 395, 269 83, 84, 85, 91
- Sirothia S. K., Kantharia N. G., Ishwara-Chandra C. H., Gopal-Krishna, 2014, TIFR GMRT Sky Survey. <http://www.tgss.tifr.res.in> 67
- Snellen I. A. G., et al., 2009, *Astronomische Nachrichten*, 330, 297 96
- Snellen I. A. G., Schilizzi R. T., de Bruyn A. G., Miley G. K., Rengelink R. B., Röttgering H. J., Bremer M. N., 1998, *A&AS*, 131, 435 71
- Soifer B. T., Boehmer L., Neugebauer G., Sanders D. B., 1989, *AJ*, 98, 766 10
- Soifer B. T., Sanders D. B., Neugebauer G., Danielson G. E., Lonsdale C. J., Madore B. F., Persson S. E., 1986, *ApJ*, 303, L41 6
- Sopp H. M., Alexander P., 1991, *MNRAS*, 251, 14 28
- Stickel M., Lemke D., Klaas U., Krause O., Egner S., 2004, *A&A*, 422, 39 54
- Strong A. W., Moskalenko I. V., 1997, in *American Institute of Physics Conference Series*, Vol. 410, *Proceedings of the Fourth Compton Symposium*, Dermer C. D., Strickman M. S., Kurfess J. D., eds., pp. 1162–1166 11
- Surace J. A., et al., 2004, *VizieR Online Data Catalog*, 2255, 0 54, 82

- Swarup G., Ananthakrishnan S., Kapahi V. K., Rao A. P., Subrahmanya C. R., Kulkarni V. K., 1991, *Current Science*, 60, no 2 iv, 81
- Taylor M. B., 2005, in *Astronomical Society of the Pacific Conference Series*, Vol. 347, *Astronomical Data Analysis Software and Systems XIV*, Shopbell P., Britton M., Ebert R., eds., p. 29 22, 71
- Thompson T. A., Quataert E., Waxman E., Murray N., Martin C. L., 2006, *ApJ*, 645, 186 14
- Tingay S. J., et al., 2013, *PASA*, 30, 7 67
- Tschager W., Schilizzi R. T., Röttgering H. J. A., Snellen I. A. G., Miley G. K., Perley R. A., 2003, *A&A*, 402, 171 68
- van de Kruit P. C., 1971, *A&A*, 15, 110 1, 9
- , 1973, *A&A*, 29, 231 1
- van Haarlem M. P., et al., 2013, *A&A*, 556, A2 67
- Völk H. J., 1989, *A&A*, 218, 67 12, 15
- Waldram E. M., 1998, in *Astrophysics and Space Science Library*, Vol. 226, *Observational Cosmology with the New Radio Surveys*, Bremer M. N., Jackson N., Perez-Fournon I., eds., p. 63 68
- Wang L., Rowan-Robinson M., 2009, *MNRAS*, 398, 109 iv, 21, 29, 31, 34, 40, 71
- Wang L., et al., 2008, *MNRAS*, 387, 601 31
- White R. L., 2014, TIFR GMRT Sky Survey. <http://sundog.stsci.edu/first/catalogs/> 23
- White R. L., Becker R. H., Helfand D. J., Gregg M. D., 1997, *ApJ*, 475, 479 22
- Williams P. K. G., Bower G. C., 2010, *ApJ*, 710, 1462 25, 26
- Xu C., 1990, *ApJ*, 365, L47 11, 65
- Xu C., Lisenfeld U., Völk H. J., 1994, *A&A*, 285, 19 51, 57
- Yamamura I., Makiuti S., Ikeda N., Fukuda Y., Oyabu S., Koga T., White G. J., 2010, *AKARI Online Data Catalog*, 2298, 0 54, 55

Yun M. S., Carilli C. L., 2002, ApJ, 568, 88 [4](#)

Yun M. S., Reddy N. A., Condon J. J., 2001, ApJ, 554, 803 [10](#), [20](#), [29](#), [50](#)

Appendix A

IDL code implementing Kaplan Meier statistics

```
PRO km_mean
;set_plot_ps, 'q_probility.ps'

;Readin  q data and flag (uncensored q=0, censored q=1)
;*****
readcol, 'q_data.txt', F='F,F,F,F,F,I', z, L60, L100, q, qu, uq

count = n_elements(q)
print, 'count', count
cq = fltarr (count)
tq = fltarr(count)

;separate uncensored q data
;*****
num = where(uq EQ 0, count)

print, 'num=', n_elements(num)
arrlen = (n_elements(num))-2

tq = q[where(uq EQ 0)]
tq = tq[sort(tq)]
tq = reverse(tq)
```

```
;separate censored q data
;*****
cq = q[where(uq EQ 0)]

;build array b holding number of repeats
;*****
a = cq
len = size(a, /n_elements)
b =fltarr(len)
x = 0.
y = 0.

WHILE (x LT len) DO begin
index=where(a eq a[x],count)
b[y] = count
x = x+count
y = y+1
endwhile

;calculate x(j)
;*****
len = size(tq, /n_elements)
xj=fltarr(len)
i = 0.
xj = tq[0]-tq

;calculate n(j)
;*****
len = size(tq, /n_elements)
nj =fltarr(len)
i = 0.
WHILE (i LT len) DO BEGIN
index = where(q LE tq[i], count)
```

```
nj[i] =count

i = i+1
ENDWHILE

;Calculate dj
;*****
len = size(nj, /n_elements)
dj = fltarr(len)
i = 0
j = 0.

WHILE (i LT (len-2)) DO BEGIN
  IF dj[j] LT 1 THEN dj[j] = 1
    IF nj[i]NE nj[i+1] THEN BEGIN
      i = i+1
      j = j+1
    ENDIF
  IF dj[j] lt 1 THEN dj[j] = 1
    IF nj[i] EQ nj[i+1] THEN BEGIN
      dj[j] = dj[j]+1
      i = i+1
    ENDIF
  ENDWHILE

;calculate nj
;*****
len = size(tq, /n_elements)
nj =fltarr(len)
i = 0.
n = 0

WHILE (i LT len) DO BEGIN
  index = where(q LE tq[i], count)
```

```
nj[n] =count
IF  dj[i] GT 1 THEN i = i+dj[i]ELSE i = i+1
n = n+1
ENDWHILE

;Calculate S(x) and F(x)
;*****
s = fltarr(len)
Sx = 1-(dj/nj)

len = size(Sx, /n_elements)

i = 0
Fx =fltarr(len)
Fx[i] = 1

WHILE (i LT (arrlen-1)) DO BEGIN
Fx[i+1]=Fx[i]*Sx[i]
i = i+1
ENDWHILE

;Estimate population mean
;*****
m = 0
i = 0
lenfx = size(Fx, /n_elements)

WHILE (i LE (lenfx)) DO BEGIN
z = (Fx(i)-Fx(i+1))*tq(i)
m = m+z
i = i+1
ENDWHILE

print, 'mean=', m
```

```
;Plot
;*****
plot, tq, Fx, xrange=[0.0, 3.0], xtitle='q!DFIR',ytitle='Probability Distribution'
trueq = interpol(tq, Fx, 0.5)
oplot,[0, 3], [0.5, 0.5], linestyle=2
oplot, [trueq, trueq], [0, 1], linestyle=2
xyouts, 0.5, 0.3,trueq

END
```